The Design and Fabrication of Miniature Microwave Bandpass Filters Using Multilayer Liquid Crystal Polymer Technology

Shilong Qian

A Dissertation Submitted for the degree of Doctor of Philosophy

School of Engineering and Physical Sciences

Heriot-Watt University

March 2014

Abstract

This thesis presents the design and fabrication techniques for miniature microwave bandpass filters using multilayer liquid crystal polymer (LCP) technology.

As a multilayer technology for microwave devices, LCP is of low cost and light weight. It also has excellent electrical properties across a wide frequency range. These characteristics make it promising for the development of next generation microwave devices for applications across commercial, defence and civil sectors. However, very limited work has been found in the open literature to apply this technology to the design of miniature bandpass filters, especially at low microwave frequencies. In addition, the reported work shows lack of fabrication techniques, which limits the size reduction of multilayer LCP devices.

To address these problems, this thesis develops advanced fabrication techniques for sophisticated LCP structures, such as multilayer capacitors, via connections and cavities. These techniques are then used to support the design of novel miniature bandpass filters for wideband and narrowband applications. For the design of miniature wideband bandpass filters, a cascaded approach, which combines highpass and lowpass filters, is presented first to provide a flexible design solution. This is followed by another novel ultra-wideband bandpass filter which produces extra transmission zeroes with minimum number of elements. It does not only have high performance but also a compact structure for high yield fabrication. For narrowband applications, two types of advanced coupled-resonator filters are developed. One type produces a very good selectivity at the upper passband edge, and its spurious-free stopband is extremely wide and of high interference attenuation. The other type, based on novel mixed-couplings approaches developed in this thesis, provides a solution to produce almost the same response as the coupling matrix prototype. This type is used to generate arbitrarily-located transmission zeroes.

All designs presented in this thesis are simulated using CAD design tools and then validated by measurements of fabricated samples. Good agreements between simulations and measurements are shown in the thesis.

Dedication

To all my family and friends

Acknowledgment

I would like to thank my supervisor Professor Jiasheng Hong for his patient mentoring and continuous support throughout my study at Heriot-Watt University. Without his guidance, encouragement and keeping me motivated, completing the work in this thesis would not be possible.

I also appreciate the help and support from my colleagues and friends: Dr. Zhangcheng Hao, Dr. Wenxing Tang, Dr. Alex Miller, Jia Ni, Francisco Cervera, Ross Aitken, Maria Lorente Crespo, David Waston, Martin Aitken, Paul Miller, Elizabeth Mckeever, Xiaobang Shang, Armando Fernandez Prieto and Miguel Angel Sanchez Soriano. My special thanks also go to my study advisors and friends, who supported my research visit, from Saint Petersburg ElectroTechnical University and University of Stellenbosch: Prof. Irina Vendik, Prof. Petrie Meyer, Prof. Riana Riana Geschke, Irina Munina, Dima Kozlov, Dr. Mike Odit, Alex Rusakov, Brandan Como, Gerdus Brand, Theunis Beukman, David Prinsloo, Shamim Nyiraneza Omar, Wiaan Beeton, Ryno Beyers, Dewald Botes, Elmine Botes, Ngoy Mutonkole and Mark Volkmann.

Last but certainly not least, I would like to thank my mum and the rest of the family, for their ever-lasting love, support and patience. Without these, I would never be able to finish my Ph.D. study.

Contents

List of Figures

List of Tables

List of Publications by the Candidate

Journal Publications:

1. S. Qian and J.-S. Hong, “Miniature Quasi-Lumped Element Wideband Bandpass Filter at 0.5-2 GHz Band Using Multilayer Liquid Crystal Polymer Technology,” *IEEE Trans. Microw. Theory Tech.*, vol.60, no. 9, pp.2799-2807, Sept. 2012.

2. S. Qian, G. Brand, J.-S. Hong and P. Meyer, “The Design of Miniature Multilayer Bandpass Filters With Mixed Couplings,” *IEEE Trans. Microw. Theory Tech.*, vol.61, no. 12, pp.4072-4078, Dec. 2013.

Conference Publications:

1. S. Qian, Z.-C. Hao, J.-S. Hong, J. P. Parry and D. P. Hand, “Design and Fabrication of a Miniature Highpass Filter Using Multilayer LCP Technology,” *41th European Microw. Conf.*, Oct. 2011, pp. 187-190. Manchester, UK.

2. S. Qian and J.-S. Hong, “Channel-reconfigurable filter with integrated switch in multilayer LCP package,” *42nd European Microw. Conf.*, Oct. 2012, pp. 265-268. Amsterdam, Netherland.

3. S. Qian, J.-S. Hong, A. Rusakov and I. B. Vendik, “A Novel Compact Ultra-Wideband Bandpass Filter,” *43rd European Microw. Conf.*, Oct. 2013, pp. 896-899. Nuremberg, Germany.

4. S. Qian and J.-S. Hong, “A compact multilayer liquid crystal polymer VHF bandpass filter,” *43rd European Microw. Conf.*, Oct. 2013, pp. 1207-1210. Nuremberg, Germany.

Chapter 1

Introduction

The RF/microwave spectrum (300 KHz-300 GHz) is a very limited resource which is shared by many applications, such as communications, radar, and navigation. However, since the RF/microwave spectrum is such a limited resource, the operation frequencies of these applications are sometimes very close to each other, especially at the low RF/Microwave frequency bands, where the bandwidth is in great demand.

To allow efficient spectrum sharing without interference among different systems, RF/microwave filters play an important role. They are designed to select or limit the signals within the assigned spectrum. To demonstrate this important function of RF/microwave filters, a simplified architecture of a RF/microwave receiver is shown in Fig. 1.1. In this receiver, the filter is used to select the signal at the operating frequency and reject the unwanted signal from other frequencies, so that the operation of this system is not susceptible to interference from other RF/microwave systems.

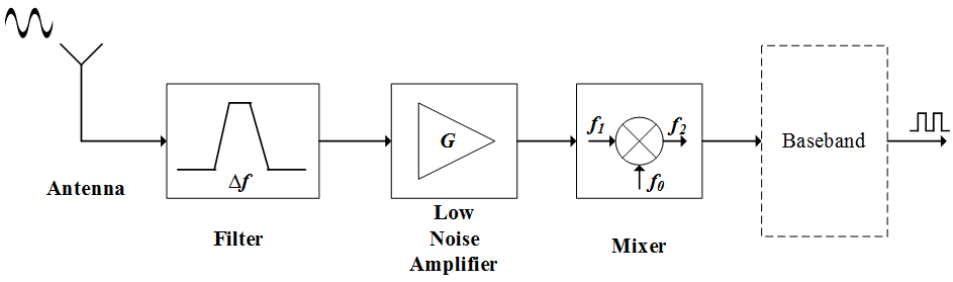

Fig. 1.1 A simplified communication system

1.1. Background

To provide the desired filtering function, the design and implementation of RF/microwave filters has been an active research area for many years. G. Matthaei, L. Young and E.M.T. Jones presented and summarised various types of RF/microwave filters in [1.1] in 1964.

In terms of transmission line technologies, conventional RF/microwave filters can be classified into many groups and some popular ones include: waveguide, coaxial line, stripline and microstrip filters. Stripline and microstrip filters are generally referred as to

planar filters. Waveguide filters have the advantages of high power-handling capability and low loss. They can also be tuned by using tuning screws to compensate for the fabrication deviations. However, they are bulky at low frequencies and expensive to manufacture. Coaxial line filters have the capability of providing a wideband match and do not need any transition for measurement purposes, but they can't integrate many novel microwave structures due to the fabrication complexity and cost [1.2]. Planar filters are currently very popular in many applications [1.3] due to the compact size and low cost. Apart from the conventional stripline and microstrip configurations, novel structures such as coplanar waveguide (CPW) filters [1.4] and substrate integrated waveguide (SIW) filters [1.5] have also been developed. However, due to the nature of small size, planar filters usually suffer from high insertion loss and have low power handling capability, compared with waveguide and coaxial line filters. Nevertheless, planar filters are very suitable for some low power applications in which small size and light weight are the key criteria. Driven by these applications, a large variety of design approaches and implementations for planar filters have been developed [1.3]. The most popular design approach for bandpass filters is the theory of coupled-resonator filter. Initially, only direct-coupled filters were designed and this gave the all pole Chebyshev response [1.6]. With the application of cross couplings, and especially the development of coupling matrix in [1.7]-[1.9], coupled-resonator filters can be designed to have arbitrarily located transmission zeroes, which can improve the selectivity of filters and provide high attenuations at desired frequencies.

1.1.1. Miniature Planar RF/microwave Filters

However, new RF/microwave applications bring new challenges to the design of planar filters. First of all, portable multi-function communication devices require all internal RF/microwave components, such as filters, to be as small as possible, so internal space can be saved for other bigger components such as batteries and application processors. Unfortunately, most conventional planar filters are relatively large at low frequencies. This is generally due to the distributed resonators which are usually used. For low frequency applications, surface acoustic wave (SAW) filters in [1.10]-[1.13] are designed to provide ultra-compact solutions for portable communication devices. However they require very high fabrication accuracy and it's not easy to generate transmission zeroes in SAW filter designs. CMOS technology can also be used to design active filters, such as those in [1.14]-

[1.16], and it provides a very good solution for designing reconfigurable filters. However, low Q, low linearity and high fabrication cost are the drawbacks of active filters.

During the past 15 years, with the development of novel multilayer packaging material, such as the low temperature co-fired ceramic (LTCC), the sizes of microwave devices have been reduced dramatically [1.17]-[1.25]. These publications cover narrowband filters [1.17]-[1.21], wideband filters [1.22, 1.23], and duplexers [1.24, 1.25]. Especially in [1.17], a 3-pole narrowband bandpass filter using high dielectric constant LTCC substrates ($\varepsilon_r = 54$) for 2.4 GHz wireless local area network (WLAN) application is reported and has a size of 1.6 mm × 0.8 mm × 0.52 mm, which is almost as small as the SAW filter in [1.13]. In order to achieve a compact implementation, most of these filters are designed using lumped-elements on LTCC, except the design in [1.23], where quarter-wavelength resonators were used.

In 2002, another multilayer solution liquid crystal polymer was reported for the application of packaging [1.26] and then characterized for microwave frequencies in 2004 [1.27]. It has excellent electrical characteristics such as a nearly constant dielectric constant across a very wide frequency range, low loss, extremely low water absorption, and low coefficient of thermal expansion [1.28]. Initially, due to its excellent characteristics, LCP was mainly used for millimetre wave application [1.29] and only one circuit layer was used. Then for X-band and ultra-wideband (UWB) applications [1.30], a few multilayer filters were reported in [1.31]-[1.33]. However, even these filters only utilize two circuit layers and one ground. It can be seen that although various types of filters for different applications have been developed using LTCC, much less work has been done using LCP, especially at frequencies lower than 3 GHz, where many applications exist such as WLAN, global positioning system (GPS) and Universal Mobile Telecommunications System (UMTS).

Table 1.1 summarises the sizes and design specifications of some miniature bandpass filters using different technologies. Since the same filter design can be easily miniaturised by using substrates with high dielectric constant, it would be fairer to remove the miniaturization effect obtained from substrates when comparing sizes. For this purpose, guided wavelength λ_g is used instead of wavelength throughout this thesis. It can be seen that, in general, the reported LTCC filters have smaller sizes than LCP filters with respect

to guided wavelengths. The main reason for this is the number of circuit layers that have been utilized on LCP is fewer than LTCC.

1.1.2. Liquid Crystal Polymer

The commercially available LCP material can be divided into two types: core films and bonding films. Both of them have a low dielectric constant of 3 and a loss tangent of 0.0025 at 10 GHz [1.28]. However, bonding films have a melting temperature of 280 ºC, while core films melt at 315 ºC. Bonding films are therefore usually used as preprag layers and core films are copper-clad for circuit pattern etching. Fig. 1.2 shows a multilayer structure consisting of LCP core films and bonding films.

Reported Miniature Bandpass Filters	Fabrication Technology	Passband Bandwidth (GHz) and FBW	Circuit Size (λ_g^3) at Center Frequency	Number of Metallization Layers	Insertion Loss
[1.17]	Multilayer LTCC	2.3-2.6 12.2%	0.07 × 0.035 × 0.023	7	< 2.3 dB
[1.18]	Multilayer LTCC	Dual-band 22.7% and 8.75%	0.07 × 0.062 × 0.011	6	1.7 dB (2.4 GHz) and 1.6 dB (2.5 GHz)
[1.22]	Multilayer LTCC	3.1-4.9 45%	0.20 × 0.08 × 0.03	11	< 1.1 dB
[1.23]	Multilayer LTCC	3.1-10.6 110%	0.57 × 0.57 × 0.02	5 (2 Grounds)	< 0.8 dB
[1.31]	Single layer LCP	9.5-10.5 10%	0.57 × 0.15 × 0.01	3	3.2 dB at 9.9 GHz
[1.32]	Multilayer LCP	3.1-10.6 110%	0.55 × 0.27 × 0.028	3	0.35 dB at 6.15 GHz
[1.33]	Multilayer LCP	3.1-10.6 110%	0.36× 0.207 × 0.014	3	0.35 dB at 5.85 GHz

Table 1.1 design specifications of some miniature bandpass filters

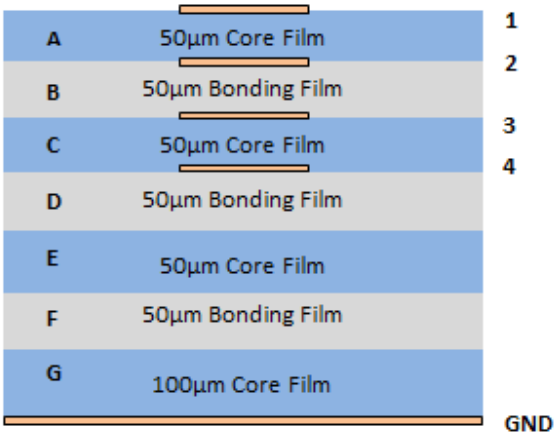

Fig. 1.2 A Multilayer LCP structure.

In terms of fabrication process, LCP is quite different from LTCC due to the bonding film. For LTCC, as shown in Fig. 1.3 (a), via holes can be punched and metalized on separate layers before lamination and co-firing. This makes it possible to fabricate any types of vias, such as blind vias and buried vias. For LCP substrates, the bonding film will be melt during the lamination process, thus if via holes are laser-drilled before lamination, they will be re-filled by the bonding film material. For the work discussed in this thesis, blind vias are used and a fabrication process as shown in Fig. 1.3 (b) is used. In the case of buried vias, an alternative via fabrication technique will be discussed in Chapter 2.

To illustrate the fabrication process of LCP further, 6 figures are included below as Fig. 1.4 (a) - (f). Fig. 1.4 (a) shows a layer of LCP core film after sheet cutting. Depending on the design, the copper cladding on this layer of LCP can be completely etched off as shown in Fig. 1.4 (b), or partially etched using the masks shown in Fig. 1.4 (c) to obtain circuit patterns shown in Fig. 1.4 (d). It can be noticed in Fig. 1.4 (b), (c) and (d) that, every layer of LCP and mask must contain a few holes in the corners for the purpose of alignment during fabrication or etching. Then these holes can be used together with the holes on the lamination plate in Fig. 1.4 (e) for multilayer LCP formation, so that all layers can be aligned precisely. Laser machining can be used to obtain such holes on LCP film for accuracy. After putting all the layers together with proper alignment, the whole LCP stack can be put into a thermal press in Fig. 1.4 (f) for the lamination process.

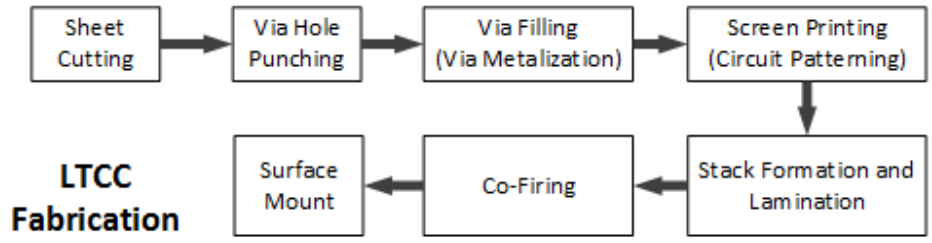

(a)

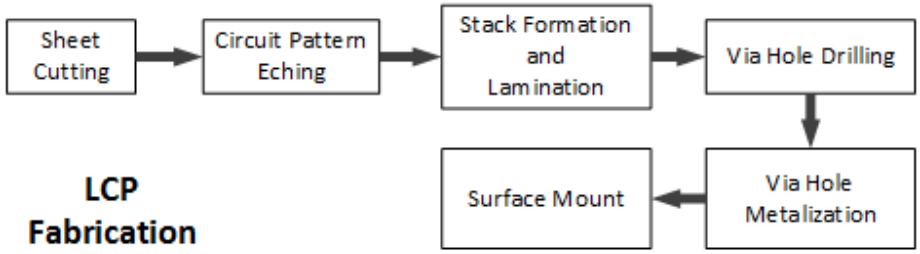

(b)

Fig. 1.3 Fabrication process for (a) LTCC and (b) LCP

Fig. 1.5 shows a recommended guideline [1.34] for the control of temperature and pressure during the lamination process. It can be seen that LCP only requires a processing temperature of 280 ºC, which is almost the same as FR4 process, in comparison with 800 ºC for LTCC. This can be a great benefit when passive elements such as thin film resistive layers have to be embedded into a multilayer LCP package [1.35, 1.36].

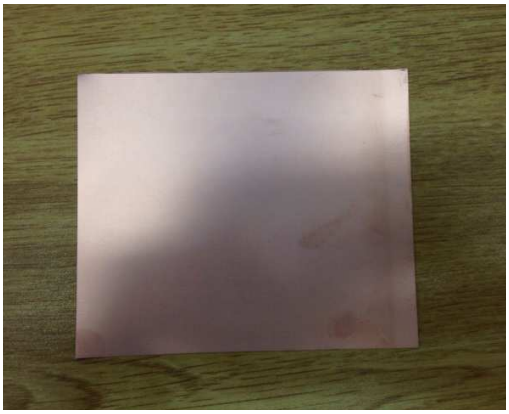

(a)

(b)

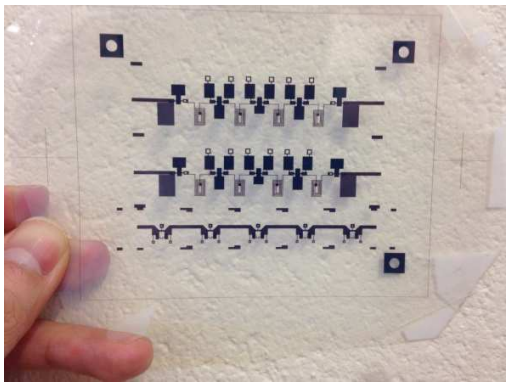

(c)

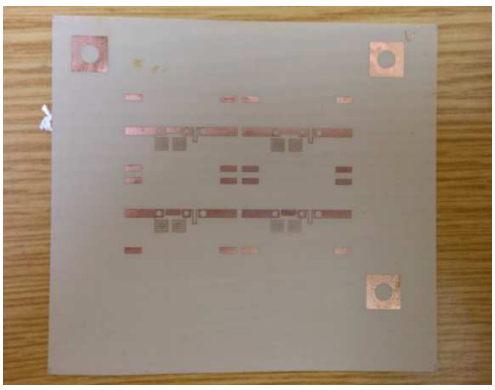

(d)

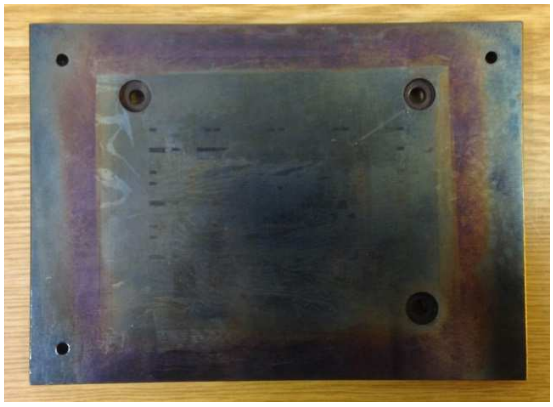

(e)

(f)

Fig. 1.4 (a) A LCP core film before etching (b) A LCP core film after etching (c) A mask for circuit patterning on LCP (d) A LCP core film after circuit patterning (e) A lamination plate with holes for alignment pins (f) A thermal press for LCP lamination

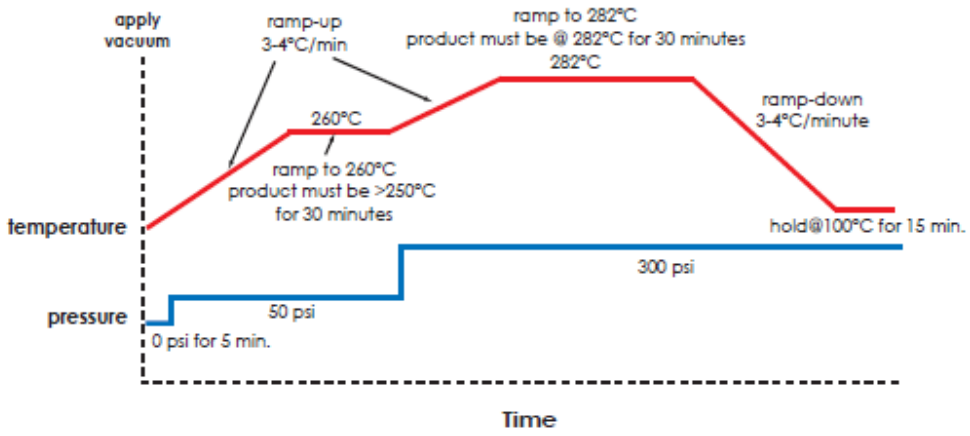

Fig. 1.5 A recommended guideline for the control of temperature and pressure during the lamination process [31]

1.2. Objectives and Overview of Thesis

Although LCP has excellent electrical properties for RF/microwave applications, it has been found that very limited work has been carried out to use it in filter design for different frequencies and applications, as briefly discussed in Section 1.1.1. The main issues that have been found are explained below.

- First of all, the number of metal layers which are involved in the design of multilayer LCP filters in open literature is less than 3, which means there are only two circuit layers and one ground. This contributes to the relatively large sizes of LCP filters as listed in Table 1.1 and does not give the designer sufficient flexibility when designing a compact multilayer LCP filter. In addition, it has been found that all of the reported multilayer LCP filters only have via connections to ground, and there are no via connections implemented to connect two circuit layers, for instance, from top layer to the middle layer.

- Secondly, most reported LCP filters [1.31] - [1.33] are for frequencies above 3 GHz to make the most of its excellent characteristics at high frequencies. However, as a low cost multilayer solution, LCP has the potential to be used for various applications below 3 GHz.

Considering the above two issues, the objectives of this thesis can be summarised as below and illustrated in Fig. 1.6.

- To reduce the size of LCP filters, a feasible solution is to deploy more layers in the design. Meanwhile, via connections among different circuit layers need to be introduced to the design. For this purpose, some low cost and reliable fabrication techniques need to be developed to ensure more layers can be integrated properly into the design. Since the general fabrication technique for multilayer LCP circuits have already been discussed in various publications [1.32]-[1.36], this thesis will mainly focus on discussing the newly developed fabrication techniques that can be used to tackle the challenges in advanced multilayer LCP circuit fabrication.

- To evaluate LCP for low frequency applications, the design of miniature and high performance bandpass filters using multilayer LCP technology needs to be explored at frequencies below 3 GHz. Novel circuit models and theories should be developed accordingly to provide optimum solutions for both wideband and narrowband applications.

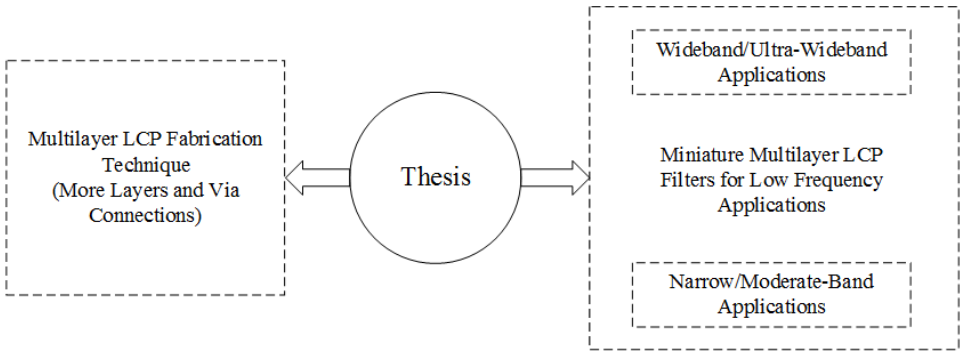

Fig. 1.6 Two objectives of this thesis

To present the work that has been undertaken for the above two objectives, this thesis is divided into seven chapters. Chapters 2 and 3 are dedicated to giving details of miniature wideband filter design with novel design approaches and implementations, while chapter 4 and 5 present high order, high performance narrowband filter designs for applications with and without transmission zeroes, respectively. Chapter 6 shows the application of multilayer LCP technology for the design of packaged reconfigurable filters. With respect to the in-house fabrication process, since it is continuously being improved throughout the duration of this work along with different filter designs, it will be discussed in several chapters. The content of each chapter is summarised below.

- In Chapter 2, a miniature ultra-wideband (UWB) filter operating at low microwave frequency band (0.5-2 GHz) is designed using cascaded fully-lumped-element highpass and lowpass filters, and for the first time in open literature, a 5-metal-layer LCP structure is used to design RF/microwave filters. An element value extraction process is also proposed to get the accurate values of different lumped-elements so that the design process relies less on the time consuming EM optimisation. Both simulations and measurements will be discussed. Several improved designs are also proposed in the chapter. Some detailed in-house fabrication technique for lamination and vias will also be discussed.

- As a continuation of Chapter 2, Chapter 3 presents another efficient approach for the design of UWB filters with finite frequency transmission zeroes. In this approach, a T-shape highpass circuit is connected in parallel with a conventional Chebyshev bandpass filter to produce an extra pole in the passband and two finite frequency transmission zeroes in the stopband. Compared with traditional designs, with the same number of poles and transmission zeros, the proposed design has fewer elements and is of compact size. The measurement result will also be presented.

- After the development of wideband filters, Chapter 4 discusses the design of miniature bandpass filters with narrow/moderate bandwidths using multilayer LCP technology. The design is based on a conventional coupled series resonator circuit model but by using purely inductive coupling, such a circuit has a strong lowpass nature. In this case, the filter response has a high selectivity on the upper passband edge. A 4-pole bandpass filter design is presented as an example and the selectivity of its upper passband edge shows similar performance characteristics to a traditional 5-pole Chebyshev bandpass filter.

- Chapter 5 develops a new theory for the application of general coupling matrix in the design of lumped element narrowband filter. In the past, a filter implemented using a conventional coupling matrix may only produce the desired frequency response in a narrow band. To solve this problem, a new type of matrix similarity transformation has been introduced. Then by applying a set of transformations, a new coupling matrix can be obtained. This coupling matrix can be used to produce a

lumped element model and by applying Π to T transformations, the model can be easily implemented on multilayer LCP substrates. To demonstrate this, two five-pole bandpass filters based on N × N and (N+2) × (N+2) coupling matrices, respectively, are presented in the chapter.

- Chapter 6 demonstrates a novel reconfigurable filter which is implemented as a LCP package. The filter uses double pole double throw switches and 4 channels with the same absolute bandwidth can be obtained. The fabrication of this filter utilises all of the fabrication techniques that have been developed in this thesis.

- Chapter 7 concludes the work carried out in this thesis and gives suggestions for future work.

References

[1.1] G. Matthaei, L. Young and E. M. T. Jones, *Microwave Filters, Impedance-Matching Networks, and Coupling Structures*, Artech House, Norwood, MA, 1964.

[1.2] D. M. Pozar, *Microwave Engineering, 2nd ed*. New York: John Wiley and Sons, inc., 1998.

[1.3] J. Hong and M. J. Lancaster, *Microstrip Filter for RF/Microwave Applications*. New York: John Wiley and Sons, inc., 2001.

[1.4] F. Tefiku, E. Yamashita, and J. Funada, "Novel directional couplers using broadside coupled coplanar waveguides for double-sided printed antennas," *IEEE Trans. Microwave Theory Tech.*, vol. 44, pp. 275–282, Feb. 1996.

[1.5] D. Deslandes and K.Wu, "Integrated microstrip and rectangular waveguide in planar form," *IEEE Microwave Wireless Compon. Lett.*, vol. 11, no. 2, pp. 68 –70, Feb. 2001.

[1.6] S. B. Cohn, "Direct-Coupled-Resonator Filter," *IRE Tran. Microw. Theory Tech.*, vol. 45, no. 2, pp.187-196, Feb. 1957.

[1.7] A. E. Atia, A. E. Williams, and R. W. Newcomb, "Narrow-band multiple-coupled cavity synthesis," *IEEE Trans. Circuits Syst.*, vol. 21, no. 5, pp. 649–655, Sept. 1974.

[1.8] R. J. Cameron, “General Coupling Matrix Synthesis Methods for Chebyshev Filtering Functions,” *IEEE Trans. Microw. Theory Tech.*, vol. 47, no. 4, pp. 433-442, Apr. 1999.

[1.9] R. J. Cameron, “Advanced Coupling Matrix Synthesis Techniques for Microwave Filters,” *IEEE Trans. Microw. Theory Tech.*, vol. 51, no. 1, pp. 1-10, Jan. 2003.

[1.10] D.C. Malocha, “SAW/BAW Acoustoelectronic Technology for Filters and Communication Systems”, *IEEE Wireless and Microwave Technology Conference*, Florida, May 2010, pp. 1-7.

[1.11] H. Yatsuda, T. Horishima, T. Eimura and T.Ooiwa, “Miniaturized SAW Filters Using a Flip-Chip Technique”, in *Proc. IEEE 1994 Ultrason. Symp.*, pp. 159-162, 1994.

[1.12] S. Yoshimoto, Yasushi Yamamoto, Y. Takahashi and E. Otsuka, “Multi-Band RF SAW Filter for Mobile Phone using Surface Mount Plastic Package”, in *Proc. IEEE 2002 Ultrason. Symp.*, pp. 113-118, 2002.

[1.13] F. Shiba, M. Yamazaki, O. Iijima and H. Yatsuda, “GPS SAW Filter Using a Wafer Level Technique”, in *Proc. IEEE 2007 Ultrason. Symp.*, pp. 937-940, 2008.

[1.14] B. Nauta, “CMOS VHF Transconductance-C Lowpass Filter,” *Electronic Letters*, vol. 26, no. 7, pp. 421-422, Mar. 1999.

[1.15] L. Su and C.-K. C. Tzuang, “A Narrowband CMOS Ring Resonator Dual-Mode Active Bandpass Filter With Edge Periphery of 2% Free-Space Wavelength,” *IEEE Trans. Microw. Theory Tech.*, vol. 60, no. 6, Jun. 2012.

[1.16] A. Otin, S. Celma and C. Aldea, “CMOS Filter with Wide Digitally Programmable VHF Range,” *Electronic Letters*, vol. 43, no. 1, pp. 421-422, Jan. 2007.

[1.17] M. Hoft and T. Shimamura, “Design of Symmetric Trisection Filters for Compact Low-Temperature Co-Fired Ceramic Realization,” *IEEE Trans. Microw. Theory Tech.*, vol 58, no. 1, pp. 165-175, Jan. 2010.

[1.18] H. Joshi and W. J. Chappell, “Dual-Band Lumped-Element Bandpass Filter”, *IEEE Trans. Microw. Theory Tech.*, vol. 54, no. 12, pp. 4169-4177, Dec. 2006.

[1.19] K. Rambabu and J. Bornemann, “Simplified analysis technique for the initial design of LTCC filters with all-capacitive coupling,” *IEEE Trans. Microw. Theory Tech.*, vol. 53, no. 1, pp. 1787–1791, May 2005.

[1.20] C. Tang and S. You, “Design methodologies of LTCC bandpass filters, diplexers, and triplexer with transmission zeros,” *IEEE Trans. Microw. Theory Tech.*, vol. 54, no. 2, pp. 717–723, Feb. 2006.

[1.21] L. K. Yeung, K.-L. Wu, and Y. E. Wang, “Low-temperature cofired ceramic LC filters for RF applications,” *IEEE Microw. Mag.*, vol. 9, no. 5, pp. 118–128, Oct. 2008.

[1.22] C.-W. Tang and D.-L. Yang, “Realization of Multilayered Wide-Passband Bandpass Filter With Low-Temperature Co-Fired Ceramic Technology,” *IEEE Trans. Microw. Theory Tech.*, vol. 56, no. 7, pp. 1668-1674, Jul. 2008.

[1.23] T. H. Duong and I. S. Kim, “New Elliptic Funtion Type UWB BPF Based on Capacitively Coupled λ/4 Open T Resonator,” *IEEE Trans. Microw. Theory Tech.*, vol., 57, no. 12, pp. 3089 – 3098, Dec. 2009.

[1.24] J. W. Sheen, “LTCC-MLC duplexer for DCS-1800,” *IEEE Trans. Microw. Theory Tech.*. vol. 47, no. 9, pp. 1883-1890, Sep. 1999.

[1.25] T. Ishizaki, H. Miyake, T. Yamada, H. Kagata, H. Kushitani, and K. Ogawa, “A first practical model of very small and low insertion loss laminated duplexer using LTCC suitable for W-CDMA portable telephones,” in *IEEE MTT-S Int. Microw. Symp. Dig.*, Boston, MA, Jun. 2000, pp. 187–190.

[1.26] K. Brownlee, S. Bhattacharya, K. Shinotani, C. P. Wong, and R. Tummala, “Liquid crystal polymer for high performance SOP applications,” in 8th *IEEE Int. Adv. Packag. Mater. Symp.*, Mar. 3–6, 2002, pp. 249–253.

[1.27] D. C. Thompson, O. Tantot, H. Jallageas, G. E. Ponchak, M. Tentzeris, and J. Papapolymerou, “Characterization of liquid crystal polymer (LCP) material and transmission lines on LCP substrate from 30–100 GHz,” *IEEE Trans. Microw. Theory Tech.*, vol. 52, no. 4, pp. 1343–1352, Apr. 2004.

[1.28] “ULTRALAM-3000-LCP-Materials Data Sheet,” Rogers Corporation, Connecticut, USA, 2012.

[1.29] S. Pinel, R. Bairavasubramanian, J. Laskar, and J. Papapolymerou, “Compact planar and vialess composite low-pass filters using folded stepped-impedance resonator on liquid-crystal-polymer substrate,” *IEEE Trans. Microw. Theory Tech.*, vol. 53, no. 5, pp. 1707–1712, May 2005.

[1.30] “Revision of part 15 of the Commision’s rules regarding ultra-wideband transmission system,” FCC, Washington, DC, Tech. Rep. ET-Docket 98-153 FCC02-48, 2002.

[1.31] R. Bairavasubramanian and J. Papapolymerou, “Fully canonical pseudo-elliptic bandpass filters on multilayer liquid crystal polymer technology,” *IEEE Microw. Wireless Compon. Lett.*, vol. 17, no. 3, pp.190–192, Mar. 2007.

[1.32] Z.-C. Hao and J.-S. Hong, “Ultra-Wideband Bandpass Filter Using Multilayer Liquid-Crystal-Polymer Technology,” *IEEE Trans. Microw. Theory Tech.*, vol. 56, no. 9, pp. 2095-2100, Sept. 2008.

[1.33] Z.-C. Hao and J.-S. Hong, “UWB Bandpass Filter Using Cascaded Miniature High-Pass and Low-Pass Filters With Multilayer Liquid Crystal Polymer Technology,” *IEEE Trans. Microw. Theory Tech.*, vol. 58, no. 4, pp. 941-948, Apr. 2010.

[1.34] “Fabrication Guidelines ULTRALAM-3000-LCP-Materials,” Rogers Corporation, Connecticut, USA, 2012.

[1.35] D. Liu, U. Pfeiffer, J. Grzyb and B. Gaucher, *Advanced Millimeter-wave Technologies: Antennas, Packaging and Circuits*, John Wiley and Sons, 2009.

[1.36] A-V. H. Pham, M. J. Chen and K. Aihara, *LCP for Microwave Packages and Modules*, Cambridge University Press, 2012.

Chapter 2

Miniature Ultra-wideband Filters Using Cascaded Highpass and Lowpass Filters and Multilayer LCP Technology

2.1. Introduction

Bandpass filters are essential components for communication and radar systems. They are usually designed to meet critical specifications, such as low passband insertion loss, high selectivity and high stopband attenuation. For a compact and low cost system, it is also desired that the filters are of very small size and compatible with low cost printed circuit board (PCB) technology, so they can be easily integrated into different systems.

Conventionally, a bandpass filter is usually fabricated on a single layer of substrate, and consists of distributed transmission line resonators and edge couplings. Various examples of this type of filters, including coupled half-wavelength resonator filters, combline filters, interdigital filters and so on, have been summarised in [2.1] and [2.2]. However, since distributed transmission line resonators are of large sizes at low frequencies, they are usually not suitable for the design of compact filters.

During the past 10 years, the development of novel multilayer packaging material has made it possible to design planar bandpass filters in a 3-D format, which reduces the size of a filter dramatically. As a popular multilayer technology, low temperature co-fired ceramic (LTCC) has been widely used in the design of multilayer microwave circuits [2.3]-[2.7]. It not only has a very low dielectric loss, but also a relatively high dielectric constant. These properties make it a very promising solution for the design of filters with small sizes and high performance.

Multilayer substrate also brings broadside couplings into the design of ultra-wideband bandpass filters. On a single layer of substrate, it is usually difficult to design wideband filters due to the fact that only weak edge couplings are available. With multilayer substrates, strong broadside couplings can be easily implemented and this makes multilayer

substrates particularly suitable for the design of wideband/ultra-wideband filters. However, filters in [2.3]-[2.6] are of narrow/moderate bandwidths. In [2.7], an ultra-wideband filter was presented, but it relies on extremely high fabrication accuracy due to the use of quarter-wavelength coupled lines with 70 μm line widths and 35μm gaps. In a multilayer design, such accuracy sometimes could not be achieved due to the registration error among different layers. Furthermore, LTCC requires over 800 ºC processing temperature and thus particular procedures have to be taken to integrate other RF modules.

Besides LTCC, organic substrate is also an option for the design of compact filters, such as the very recent Rogers Experimental Polymer (RXP) organic substrate [2.8, 2.9]. RXP substrate has a low dielectric constant between 3 and 3.5 at 1 GHz and very low processing temperature of 220 ºC, which is very suitable for RF modules integration [2.8]. However, as a newly developed technology, RXP substrates are not widely available yet and the design in [2.9] did not show superior performance in comparison with LTCC filters.

Another multilayer candidate, liquid crystal polymer (LCP), has also been popular due to its superior electrical properties up to millimeter-wave frequencies [2.10, 2.11]. It has very stable dielectric constant of 3 and loss tangent of 0.0025 over a wide frequency range. These properties make LCP a very suitable solution for the design of compact wideband filters [2.12]-[2.15]. Compared with LTCC, LCP has much lower processing temperature of 280 ºC. Although LCP has lower dielectric constant than LTCC, which makes it more challenging for RF/Microwave circuit miniaturization, it makes LCP circuit design less sensitive to fabrication tolerances than LTCC. Although some cheaper PCB laminates can be used for miniature filter designs as in [2.16], LCP offers much higher flexibility on circuit thickness and a very strong coupling can be achieved with a separation as small as 25 µm. This is very important for the design of low frequency wideband filters that requires large capacitances. Furthermore, for LCP substrates, circuit layers (core films) and prepreg layers (bonding films) have almost the same characteristics, such as thermal expansion coefficient, dielectric constant and water absorption, which can be a great benefit for practical applications.

Although UWB LCP filters operating at frequencies between 3.1 and 10.6 GHz have been reported in [2.12]-[2.15], to the author's knowledge, miniature wideband bandpass LCP filters for low RF/Microwave frequencies haven't been investigated and the large

wavelengths at these frequencies make it very challenging to reduce the size and maintain a good performance at the same time. For UWB LCP filters, compact design with a size smaller than 10 mm × 5 mm has been reported in [2.13], thus the first objective of this work is to develop a wideband bandpass filter with the same size but covering a much lower frequency band from 0.5 to 2 GHz to achieve about 80% size reduction.

To achieve this, implementing the filter on more layers is a feasible solution. However, in the open literature, LCP microwave filters have only been implemented with two circuit layers and a ground plane [2.12]-[2.15]. A reason for this is due to the less mature LCP fabrication process. When more circuit layers are involved, registration errors occurr during the lamination process and make it very difficult to achieve the designed specifications for a multilayer LCP filter. Thus, developing a reliable fabrication process for LCP multilayer circuits is another objective of this work.

For the above two objectives, the design and fabrication of an ultra-wideband filter with a passband from 0.5 to 2 GHz will be presented in this chapter. Section 2.2 will introduce some multilayer lumped-elements which will be used in the development of compact bandpass filters across the whole thesis. A value extraction process for these elements will be discussed as well. Based on these lumped-elements, a highpass filter with a cutoff frequency of 0.5 GHz and a lowpass with 2 GHz are designed in Section 2.3. These two filters are then cascaded as an ultra-wideband bandpass filter. Section 2.4 discusses a newly developed fabrication technique for multilayer LCP circuits. Then a fabricated sample for the above ultra-wideband filter is presented with its measured response. To further improve the performance, two modified designs will also be discussed. This is followed by a conclusion in Section 2.5.

2.2. Lumped-Elements on Multilayer LCP Substrates

Conventionally, distributed transmission line resonators were usually used for the design of microwave planar filters. However, since the dimensions of distributed resonators are proportional to the wavelength, they are not suitable for the design of miniature bandpass filters at low frequencies. In this work, lumped or quasi-lumped-elements implemented on multilayer LCP substrates are characterised and used for the design of compact bandpass filters.

2.2.1. Multilayer Capacitors and Inductors

Capacitor is usually the most size-consuming part in a conventional single layer filter design, where only weak edge coupling, such as that in an interdigital capacitor in Fig. 2.1 (a), is adopted. This becomes a more serious problem for the design of low frequency filters, in which large capacitances are needed. With the development of multilayer substrate, strong broadside coupling structure as shown in Fig. 2.1 (b) can be easily implemented, which reduces the size of the capacitive elements dramatically. To make the most of multilayer substrates, multilayer broadside-coupled capacitors [2.17][2.18] are adopted for this work. As shown in Fig. 2.1 (c), the 4-layer structure works as three capacitors paralleled between two ports, which theoretically can reduce the size by 67% compared to the structure in Fig. 2.1(b). Further size reduction can be achieved by using more layers with the cost of fabrication complexity. In addition, with commercially available LCP thin films, the separation between every two metal layers can be as small as 25 um, which provides much stronger coupling than such structures on normal thick substrate.

Fig. 2.2 shows the microstrip inductors [2.19] that will be used in this work. The meander line can be used to implement small series inductance between any two ports while the spiral line, with a connection via, are very suitable for achieving large inductances between any two layers in a multilayer circuit.

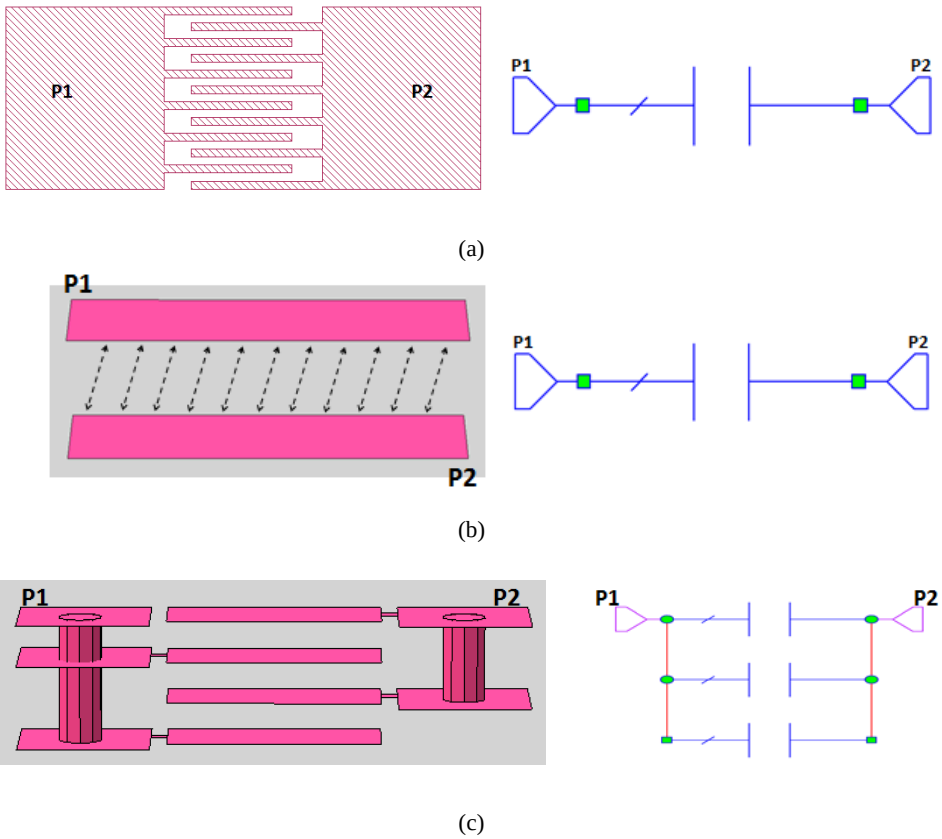

Fig. 2.1 (a) Inter-digital capacitor on a single layer substrate (b) Conventional broadside-coupling structure (b) Multilayer broadside-coupling structure

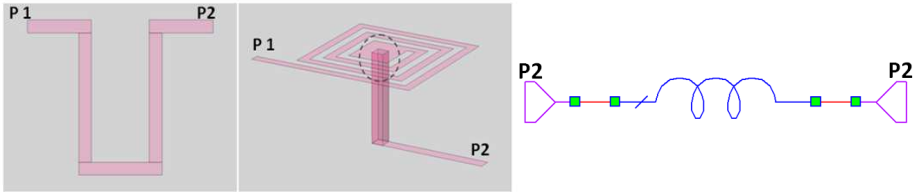

Fig. 2.2 Meander and spiral lines as inductors

2.2.2. Value Extractions for Lumped-Elements

Before putting these elements together to form a filter, it would be ideal if these elements have accurate values as required by the circuit prototype, so that even the initially designed filter can produce desired response, and the design cycle can rely less on the time consuming EM optimisation.

Although many closed-form formulas are available in [2.17] to calculate the capacitances and inductances of some microstrip elements, they are only suitable for the initial estimation. To have a more accurate control of the element capacitance/inductance in the

design flow, a value extraction process for microstrip lumped-elements is detailed here to obtain a connection between the microstrip elements and their capacitances or inductances.

Firstly, any one of those multilayer structures from Fig. 2.1 and Fig. 2.2 can be considered as a two-port network between P1 and P2. Then this two-port network is represented as a *Y* or *Z* element, depending of if the structure is capacitive or inductive, respectively, as shown in Fig. 2.3.

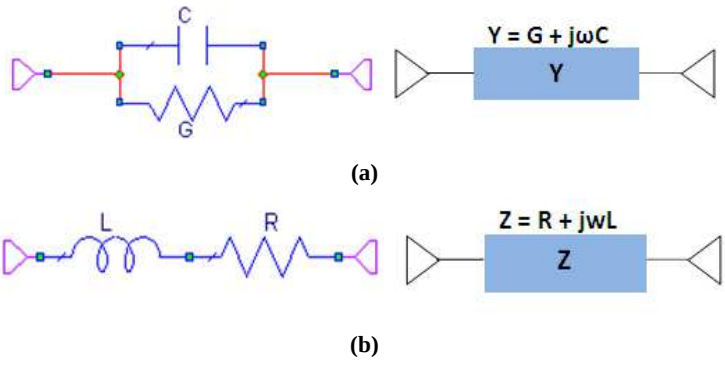

Fig. 2.3 (a) Admittance representation for a capacitor (b) Impedance representation for an inductor

For the above models, their *ABCD* parameters can be represented using equation (2.1) or (2.2). It can be seen that the admittance *Y* and impedance *Z* can actually be obtained from the value of *B* parameter. The problem of value extractions turns into finding the accurate *B* parameter. By using any EM full wave simulator, it is usually convenient to get very accurate *S* parameters, and the *B* parameter can then be calculated using (2.3). Eventually, the inductance or capacitance of a multilayer structure can be accurately extracted using (2.4) and (2.5) or (2.6) and (2.7), respectively. Quality factors (Q) can also be estimated using (2.8) or (2.9). After such an extraction, feedback can be applied to the physical structure until the required value is obtained. This process is summarised in Fig. 2.4.

$$\begin{bmatrix} A & B \\ C & D \end{bmatrix} = \begin{bmatrix} 1 & \frac{1}{Y} \\ 0 & 1 \end{bmatrix} \tag{2.1}$$

$$\begin{bmatrix} A & B \\ C & D \end{bmatrix} = \begin{bmatrix} 1 & Z \\ 0 & 1 \end{bmatrix} \tag{2.2}$$

$$B = \frac{Z_0[(1+S_{11})(1+S_{22}) - S_{12}S_{21}]}{2S_{21}} \tag{2.3}$$

$$Y = \frac{1}{B} = G + j\omega C \tag{2.4}$$

$$C = \frac{Im(Y)}{\omega} \tag{2.5}$$

$$Z = B = R + j\omega L \tag{2.6}$$

$$L = \frac{Im(Z)}{\omega} \tag{2.7}$$

$$Q_C = \frac{\omega C}{G} = \frac{Im(Y)}{Re(Y)} = \frac{Im(1/B)}{Re(1/B)} \tag{2.8}$$

$$Q_L = \frac{\omega L}{R} = \frac{Im(Z)}{Re(Z)} = \frac{Im(B)}{Re(B)} \tag{2.9}$$

It should be mentioned that with the existence of ground plane, there will always be coupling between these elements and ground. These parasitic couplings are not considered in the above value extraction. Although they could also be extracted simply by replacing the *Y* and *Z* model in Fig. 2.3 with a Π model, it is not necessary here. Firstly, all of these multilayer elements are implemented on LCP substrate with a low dielectric constant. Considering a relatively large separation between them and the ground, the coupling will be relatively weak. Secondly, all of these elements are of very small sizes. These small sizes together with a weak coupling strength would only generate a capacitance, which is much smaller than the main element values represented by the *Y* and *Z* elements in Fig. 2.3.

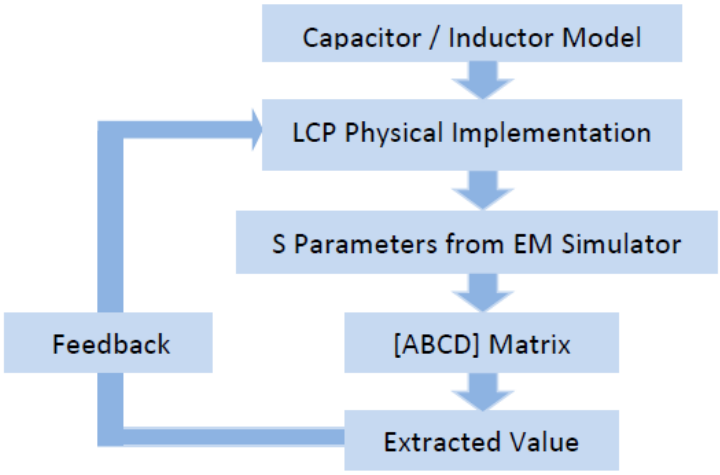

Fig. 2.4 Value extraction for multilayer capacitors or inductors

2.3. An Ultra-Wideband Bandpass Filter using Cascaded Highpass and Lowpass Filters

In this section, an ultra-wideband bandpass filter with a passband from 0.5 GHz to 2 GHz will be designed using cascaded highpass (HP) and lowpass (LP) filters. The filter has a lumped-element circuit model as shown in Fig. 2.5 (a) and its element values are listed in Table 2.1. Fig. 2.5 (b) shows the circuit simulation result [20]. Since the cutoff frequencies of these two filters are chosen separately, the design method of this work can be readily applied to designs for other frequencies. In addition, with a properly designed LP section, a wide upper stopband can be easily achieved, which will be demonstrated in the following sections. Furthermore, compared with the resonators-based bandpass filter, this cascaded type of bandpass filter can provide small and flat group delay [2.13].

The physical implementation of the filter will be done on multilayer LCP substrates with a total thickness of 0.6 mm. The relative dielectric constant and loss tangent for the LCP are 3 and 0.0025, respectively.

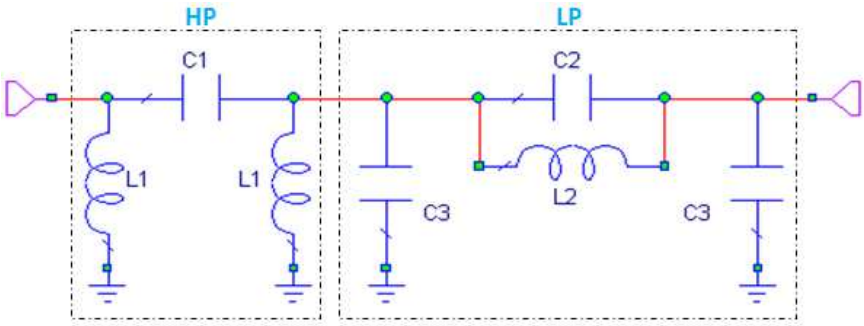

(a)

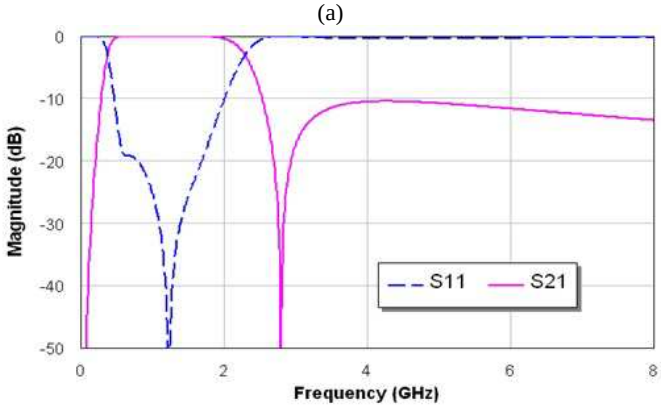

(b)

Fig. 2.5 (a) The circuit model for an ultra-wideband bandpass filter (b) Simulation results of the circuit model

C_1	L_1	C_2	L_2	C_3
5.5 pF	14.3 nH	1.33 pF	2.48 nH	1.19 pF

Table 2.1 Component Values for the circuit model

2.3.1. A Miniature Highpass Filter with a cutoff frequency of 0.5 GHz

Since size reduction is the main challenge of this work, the first consideration of choosing an appropriate prototype is the total number of elements in the prototype. Potentially, the less number of elements, the smaller the footprint of the filter implementation, though there may be some trade-off for the selectivity and stopband rejection.

Based on this, for the HP filter, a Π network, shown as "HP" in Fig. 2.5(a) is chosen to produce a Chebyshev highpass response with 0.5 GHz cutoff. For the Chebyshev highpass filter, since there is always a transmission zero located at DC, this simple highpass prototype can produce a sharp passband edge for the 0.5 GHz cutoff frequency, as shown above in Fig. 2.5(b).

To implement the relatively large capacitance C_1 in Fig. 2.5(a), a 4-layer broadside-coupled capacitor as shown in Fig. 2.1 (a) with planar dimensions in Fig. 2.6 (a) is chosen. The separation d between every two layers is chosen to be 0.05 mm for a strong coupling. The sizes of the via and via patches are chosen for the purpose of easy fabrication. The initial values of W and L are obtained according to the metal-insulator-metal (MIM) capacitance formula of (2.10), where n is the number of layers. Since this only gives an initial estimation, then by varying the W and L, more accurate capacitor values can be extracted using the method as presented in Section 2.2.2. Fig. 2.6 (b) shows the extracted capacitances for various W and L combinations at the cutoff frequency 0.5 GHz and it can be seen that the L = 2.6 mm and W = 1.1 mm combination can be chosen to implement the C_1 in the circuit prototype. Fig. 2.6 (c) shows the capacitances and Q factors of the selected combination at different frequencies, for a substrate loss tangent tanδ = 0.0025 and the conductor conductivity σ = 5.8 × 107 S/m.

$$C = \frac{\varepsilon_r WL(n-1)}{d} \tag{2.10}$$

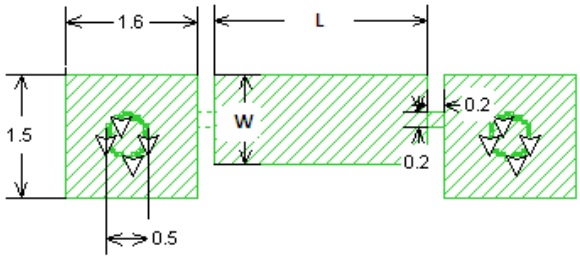

(a)

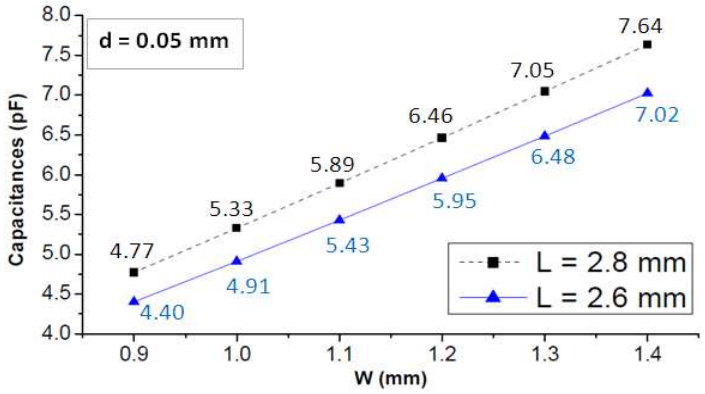

(b)

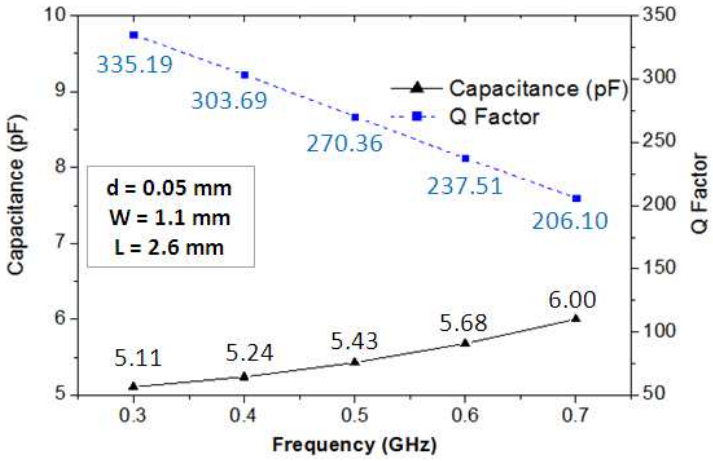

(c)

Fig. 2.6 (a) Planar dimensions for multilayer capacitor (b) Extracted capacitances for different dimensions at cutoff frequency 0.5GHz (c) Extracted capacitances and Q factors at different frequencies with εr = 3, h = 0.6 mm, tanδ = 0.0025 and σ = 5.8 × 107 S/m.

For the large inductance L_1, high impedance lines in a spiral shape should be used for a compact design, although this will decrease the Q of the inductor. Since the inductor L_1 is shunt to ground, the value extraction process need to be changed to a one-port model as shown in Fig. 2.7. Then Y_{11} is the parameter to be used for value extraction due to the short-circuit condition, according to network analysis. (2.11) and (2.12) can then be used to calculate the inductance. For this work, a spiral line with the dimensions as shown in

Fig.2.8 (a) has been chosen. The grounding via has a length of 0.6 mm, which is also the total thickness of the substrate. The dimensions of the central via and via patch are firstly chosen to be a value for easy fabrication, and then by increasing the number of turns, different inductances can be achieved. Fig. 2.8 (b) shows the extracted inductances for different number of turns and dimensions at the cutoff frequency 0.5 GHz. It can be seen that the one with 3 turns of 0.15-mm-wide line should be used for this work. Fig. 2.8 (c) shows the inductances and Q factors of the selected spiral inductor at different frequencies near the cutoff frequency. It can be seen that compared with the multilayer capacitor, spiral inductor has particularly low Q. For wideband application, this is usually not an issue, but for narrowband filters, this low Q might result in large insertion loss.

Fig. 2.7 One port model for shunt inductor

$$Y = \frac{1}{Z} = \frac{1}{R + j\omega L} = Y_{11} \tag{2.11}$$

$$L = \frac{Im(1/Y_{11})}{\omega} \tag{2.12}$$

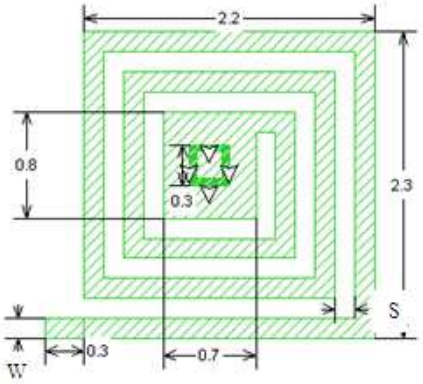

(a)

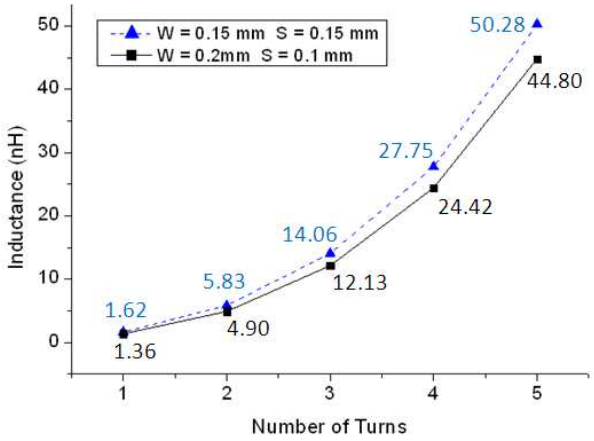

(b)

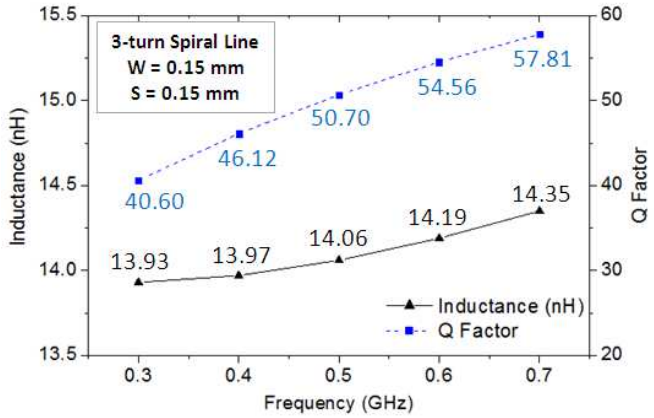

(c)

Fig. 2.8 (a)Planar dimensions for spiral inductor (b) Extracted inductances for spiral inductor with different number of turns at cutoff frequency 0.5GHz (c) Extracted inductances and Q factors at different frequencies with εr = 3, h = 0.6 mm, tanδ = 0.0025 and σ = 5.8 × 107 S/m.

By using these elements, a highpass filter with 0.5 GHz can be built with a 3-D structure as shown in Fig. 2.9 (a), which has a topology for a small footprint while minimizing parasitic

coupling between adjacent elements. Excluding the feed line, the highpass filter has a size of 6.2 mm × 4.1 mm as shown in Fig. 2.9 (b). Fig. 2.9 (c) shows the full-wave EM simulated result [2.21] of the proposed structure, compared with the response of the ideal circuit prototype from Fig. 2.5 (a). It can be seen that the simulated and theoretical *S21* responses are almost identical over a very wide frequency range from DC up to 6 GHz, which is 12 times of the cutoff frequency. Similarly, the simulated *S11* or return loss response is nearly below -15 dB over the wide passband, as predicted by the theory; despite more ripples appear in the simulated response. These additional ripples mainly result from the parasitic parameters of the microstrip quasi-lumped elements and the spurious resonances at around 7 GHz in the simulation are attributed to the self-resonance of the capacitor and inductor. Nevertheless, the designed quasi-lumped elements and their modelling equivalent circuit work well for this wideband filter design.

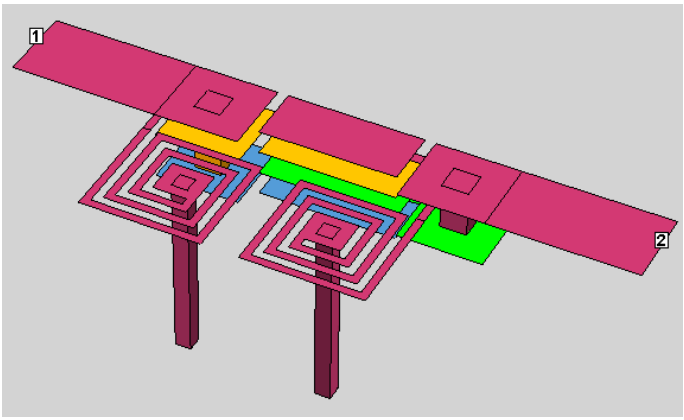

(a)

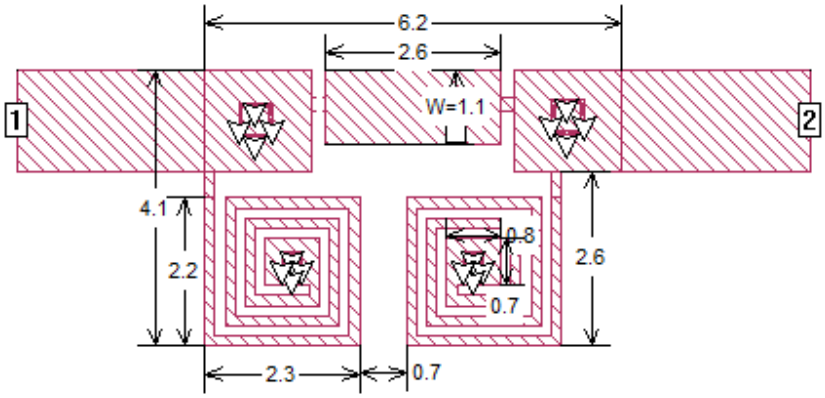

(b)

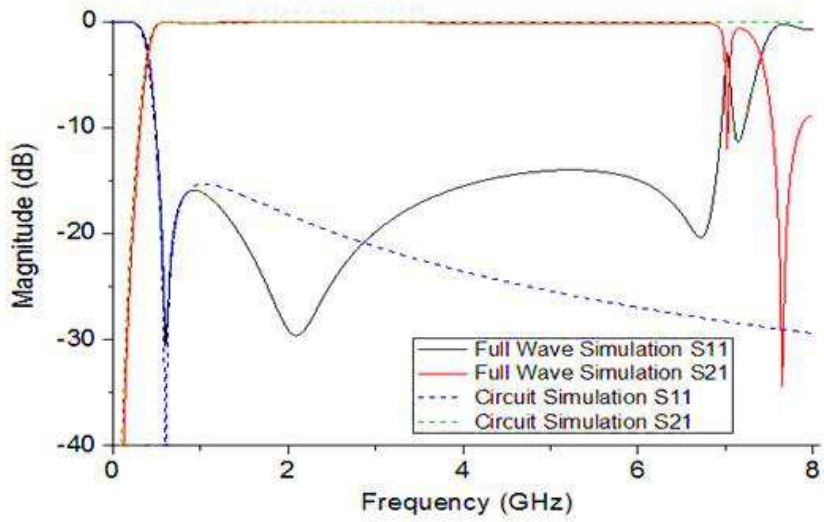

(c)

Fig. 2.9 (a) 3-D structure of the highpass filter (not on scale), (b)its planar dimensions and (c) its full wave simulation result compared with ideal circuit response.

2.3.2. A Miniature Lowpass Filter with a cutoff frequency of 2 GHz

For the lowpass filter, a simple Π network can also be used to produce the lowpass response with minimum number of elements. However, the selectivity of such a conventional Chebyshev lowpass filter would be very poor compared with the highpass filter because its transmission zero is at the infinite frequency which is far away from the desired cutoff frequency of 2 GHz. Thus, for the purpose of getting roughly symmetric passband edges at both sides, an elliptic-function lowpass prototype, shown as "LP" in Fig. 2.5(a), is chosen for the design of lowpass filter to produce a finite-frequency transmission zero near the upper side edge of the passband, as shown in Fig. 2.5 (b). This finite-frequency transmission zero results from the parallel resonant circuit consisting of L_2 and C_2.

For the implementation of this lowpass filter, inductor L_2, with a very small value, can be simply implemented with a meander high impedance line as shown in Fig. 2.10 (a). The extracted inductance values for different sizes are shown in Fig. 2.10 (b). The inductance and quality factor against frequencies for W = 0.2 mm and L = 2.1 mm are displayed in Fig. 2.10 (c).

To realize C_2, a 3-layer small size capacitor can be used. The extracted values are shown in Fig. 2.11 (a) and (b), where W and L are the dimensions as denoted in Fig. 2.6 (a). C_3 can be implemented with a conventional 2-layer broadside coupled structure, with the second layer connected to ground. Its value extraction is done in a similar way to the shunt inductor in Fig. 2.7 using Y_{11} parameter.

Based on these elements, the 3-D structure for the lowpass section can be obtained as shown in Fig. 2.12 (a). Care should be taken to achieve a small size of filter while minimizing unwanted cross couplings by adjusting the separation of the quasi-lumped elements implemented. However, since the meander inductor is on top of the multilayer capacitor, the coupling between them decreases the effective inductance of the meander line. In this case, the planar dimensions are slightly adjusted and shown in Fig. 2.12 (b). It should be mentioned that this additional parasitic capacitance together with the existing inductance could cause resonance. However, the additional parasitic capacitance is much smaller than those main capacitances in the design. This means that the resonance would only be produced at a much higher frequency outside the passband. Fig. 2.12 (c) shows the

full wave simulation result compared to the circuit response. It can be seen that the proposed structure matches well with the circuit response from very low frequency up to 6 GHz and the resonance at 7 GHz is caused by the additional parasitic capacitance between the inductor L_2 and capacitor C_2 mentioned above. This has shown that although the resonance caused by extra parasitic capacitances would not affect the passband performance, it does limit the bandwidth of the stopband. To move this resonance to even higher frequency, a feasible solution is to use a thinner track for the inductor L_2 with the cost of lower quality factor.

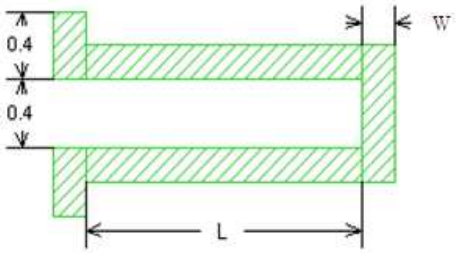

(a)

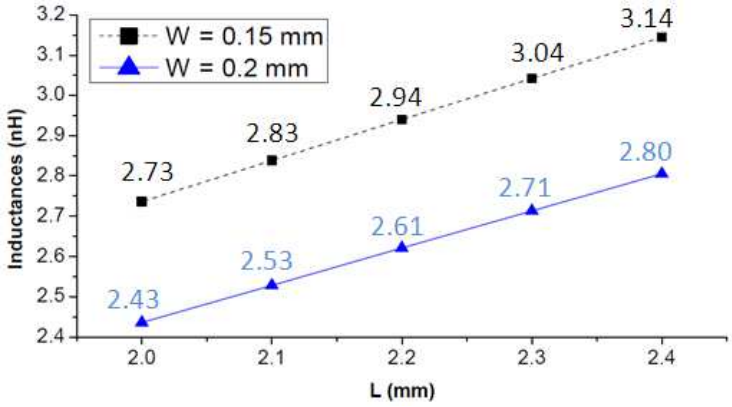

(b)

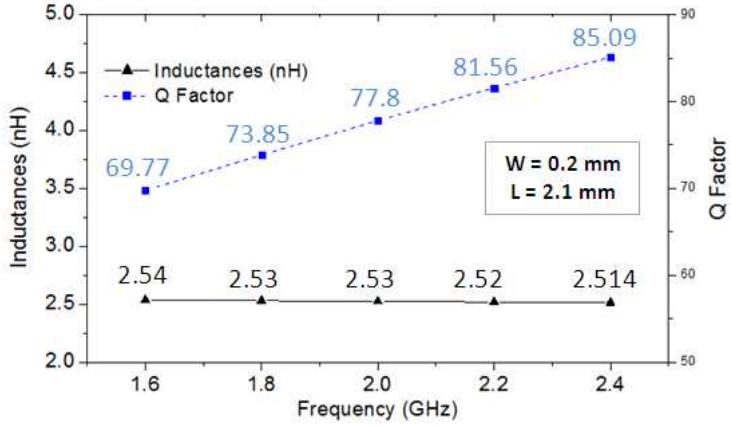

(c)

Fig. 2.10 Dimensions of a meander line inductor (b) extracted inductances for different dimensions at cutoff frequency 2GHz (c) extracted inductances and Q factors at different frequencies with ε_r = 3, h = 0.6 mm, tanδ = 0.0025 and σ = 5.8 × 107 S/m.

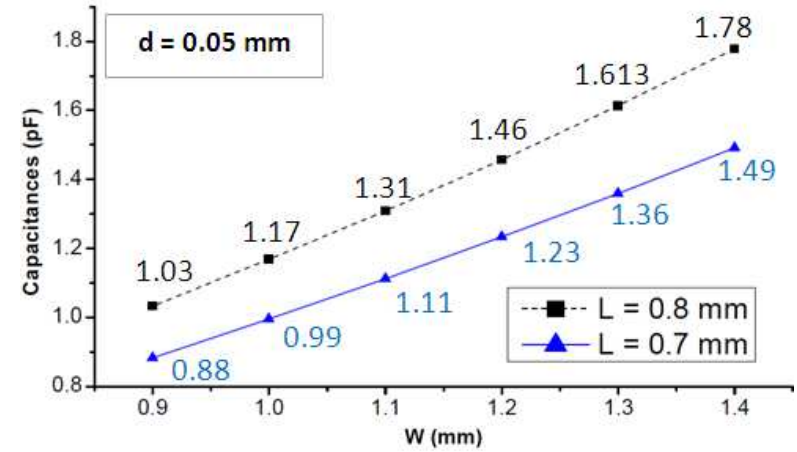

(a)

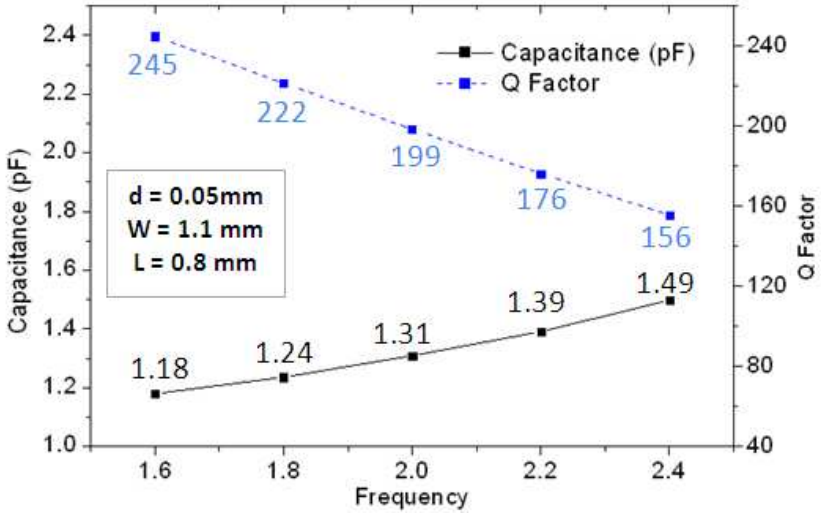

(b)

Fig. 2.11 (a) Extracted capacitances for different dimensions at cutoff frequency 2GHz (b) Extracted capacitances and Q factors for different frequencies with εr = 3, h = 0.6 mm, tanδ = 0.0025 and σ = 5.8 × 107 S/m.

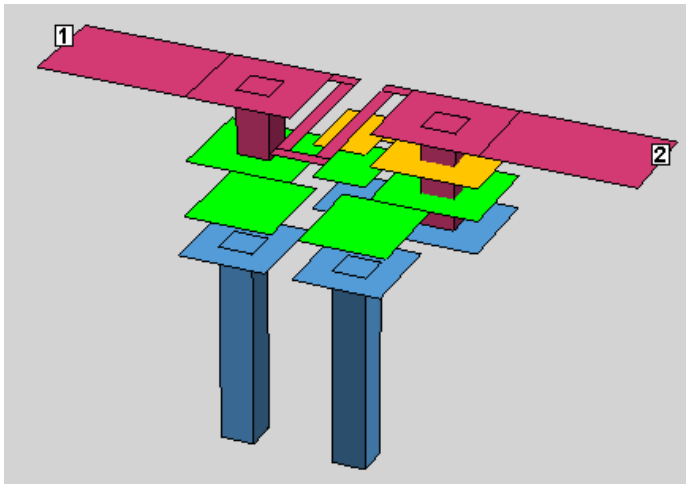

(a)

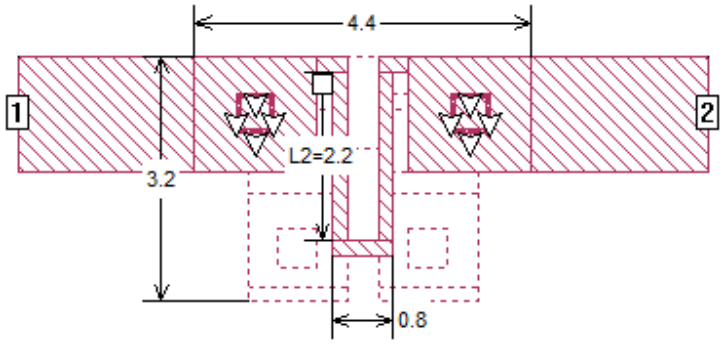

(b)

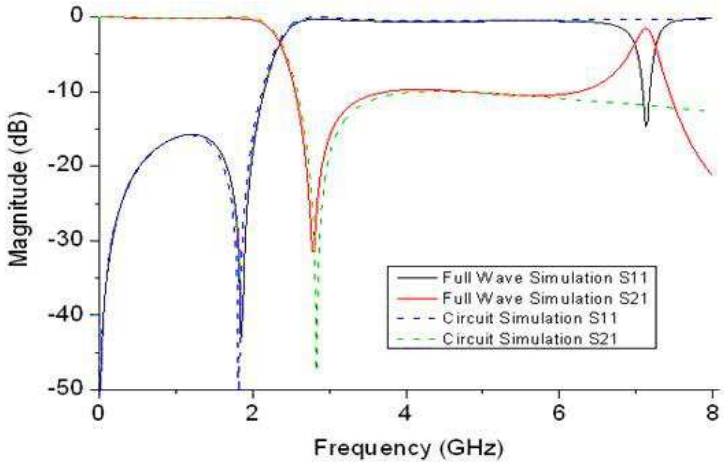

(c)

Fig. 2.12 (a) Proposed 3-D structure for the lowpass filter (not on scale), (b) its planar dimensions and (c) its full wave simulated result compared with circuit prototype response

2.4. Fabrication and Measurement

2.4.1. Multilayer Structure and Lamination

Commercially available LCP substrates can be generally divided into two types: core film and bonding film. Both of them have the same dielectric constant and loss tangent [2.22]. However, the bonding film has a melting temperature of 280 ºC, which is lower than that of 315 ºC for the core film. Thus, for multilayer circuit construction, core films are usually used as circuit boards, which can be double-side etched using normal inexpensive PCB etching process, while every bonding film is used as an adhesive layer between two core films. Fig. 2.13 shows a five-metal-layer construction which is used to implement this work. Metal layers 1 - 4 are all double-sided etched on 50 um core films to implement the multilayer circuit structure while layer 5 works as ground plane.

Fig. 2.13 Multilayer LCP structure for the implementation of filters in this chapter

For multilayer LCP circuits, there is a common issue which is the registration error during lamination. To reduce this error, in addition to the normal lamination guidelines in [2.22], the following methods can be used.

1) In general, the less number of layers, the better the registration. For the structure in Fig. 2.13, since it is only important to get a good registration among the first three layers A, B and C, which consist of all the circuit metallization, they can be laminated together first. Then a second lamination can be done to complete the structure.

2) During the heating process, the high pressure of 300 psi should only be applied after the material has reached 260 ºC for half an hour. Otherwise, the circuit metallization can be easily pushed away during the heating process if high pressure is applied at the beginning. When the material has been at 260 ºC for half an hour, instead of increasing the pressure to 300 psi as a fast transition, the author recommends that the pressure should ramped up slowly with a rate of 60 psi/min.

3) The LCP bonding films are thermoplastic adhesive materials, so pressure drop during the cooling process can cause large registration error. Thus the lamination pressure of 300 psi should be kept until the temperature is about 100 ºC then reduced slowly to 0 with a rate of 60 psi/min.

2.4.2. Via Fabrication on LCP substrates

When multilayer structure is involved, the fabrication complexity would be increased. Especially in the case of multilayer broadside-coupled capacitor as shown in Fig. 1 (b), the fabrication of connection via becomes very important for achieving good agreement between fabrication and simulation.

For multilayer LTCC circuits, via holes can be drilled on separate layers and filled with conductive paste before lamination and co-firing. However, this cannot be done for LCP. LCP bonding films will be melted during the lamination and this would refill the via holes and push the paste out. For this work, two kinds of via fabrication techniques based on through-hole plating for LCP have been investigated:

1) The first three layers A, B and C in Fig. 2.13, which contains all of the 4 circuit metal layers, can be laminated first and via holes for the multilayer capacitors can be drilled as through holes. By using through-hole plating technique, the inner wall of the vias can be wholly plated by highly conductive paste. Before doing the second lamination, to prevent the processed vias on the first three layers refilled by the bonding material from layer D in Fig. 2.13 under high lamination pressure, via holes with slightly bigger diameter should be drilled on the layer D at the same positions. Then a second lamination can be done to finish the circuit lamination. This method can also be used for the fabrication of buried vias in some circuits.

2) Via holes can also be processed after the whole lamination is done. In this way, via holes for the multilayer capacitor in Fig. 2.9 (a) will be drilled as blind holes. Then high conductivity paste can be applied to the via holes for metallization.

For the first method, the through holes are easy to be drilled and plated, but the final interconnection depends on the robustness of the plated metallization. The second method provides good connection, but as a trade-off, it requires more accurate fabrication control to get the blind holes. In this work, the second method is used and all the machining work are done using CO_2 laser for precise fabrication.

To further improve the connection, all of the multilayer interconnection vias similar to those in Fig. 2.14 (a) are modified to the structure in Fig. 2.14 (b), where the stepped vias are used. In this way, the contact area between the middle layer via patch and the plating paste will be much larger and will not only reply on the thickness of the metal layer. This will make much more reliable contacts and reduce the conductive loss.

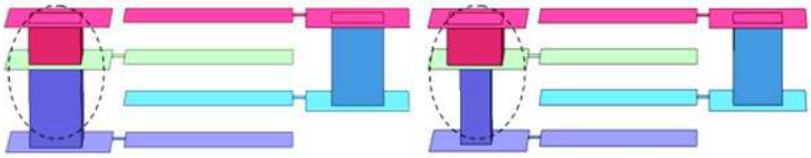

(a) (b)

Fig. 2.14 (a) Conventional and (b) Modified via structure

2.4.3. Fabricated Sample and Measured Results

Based on the designs in Section 2.3, a filter with a 3-D structure shown in Fig. 2.15 can be formed. The size of filter is just 9 mm × 4 mm × 0.6 mm, which is $0.234\lambda_g \times 0.104\lambda_g \times 0.016\lambda_g$ and λ_g is the guided wavelength on a 0.6 mm thickness substrate with dielectric constant 3, at the centre frequency of 1.25 GHz.

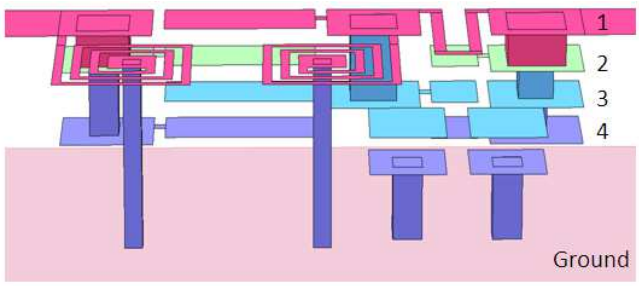

Fig. 2.15 3-D structure of the proposed design

The filter is then fabricated and measured on a Hewlett Packard 8510B network analyser. Fig. 2.16 (a) is a photograph of the fabricated filter under a microscope. The stepped vias can be easily seen. Fig. 2.16 (b) shows the measured result compared to the circuit simulation. Apart from some mismatching problem in the passband, there is only a small frequency shift at the higher cutoff, which is due to fabrication tolerance. Nevertheless, the measurement is in a good agreement with the circuit simulation up to 6.5 GHz, which is about 5 times of the centre frequency. The insertion loss is smaller than 0.7 dB between 0.5 GHz and 2 GHz and the group delay variation is within 0.3 ns between 0.6 GHz to 1.9 GHz, which is 87% of the passband.

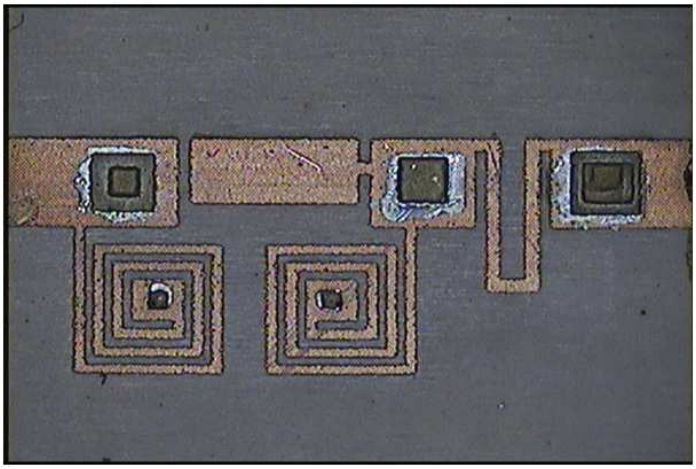

(a)

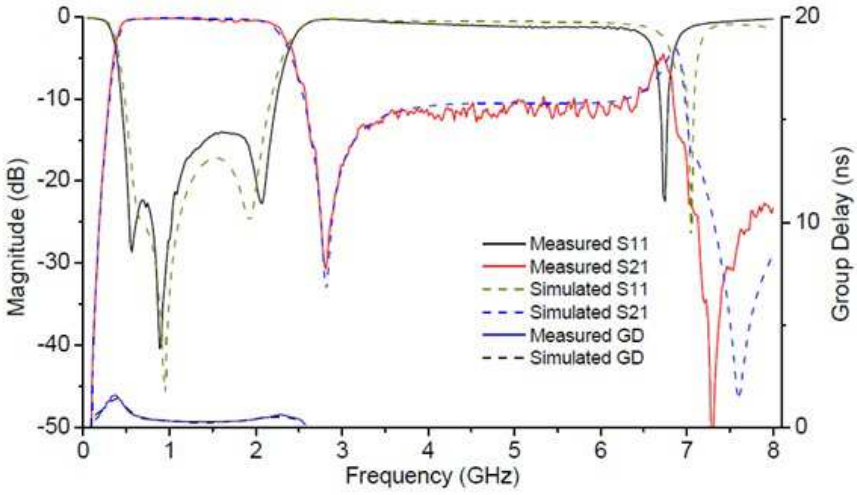

(b)

Fig. 2.16 (a) Photography of the fabricated wideband bandpass filter using multilayer LCP technology. (b) Measured result compared with circuit simulation.

2.4.4. Improved Designs

Although the design in Fig. 2.16 (a) realises the required passband performance with good selectivity at both sides of the passband, the upper stopband attenuation is only slightly better than 10 dB. To improve this, one could increase the order of the low pass filter. This method enhances both the passband and stopband responses; hence both the passband edge selectivity and stopband rejection can be improved. Fig. 2. 17 (a) and (b) show a circuit model of a higher order elliptic-function lowpass filter and its simulated response, respectively.

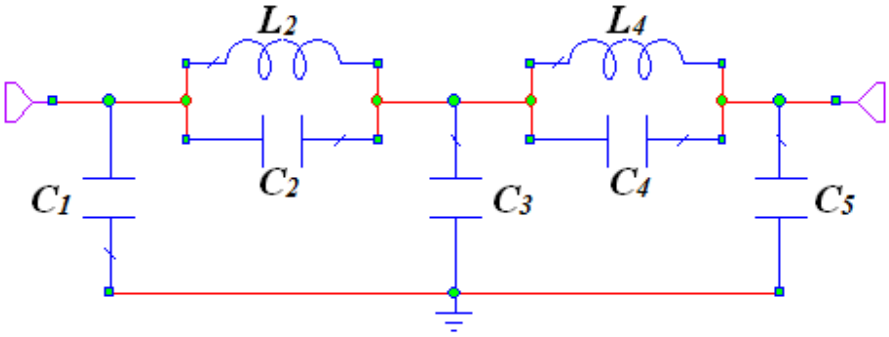

(a)

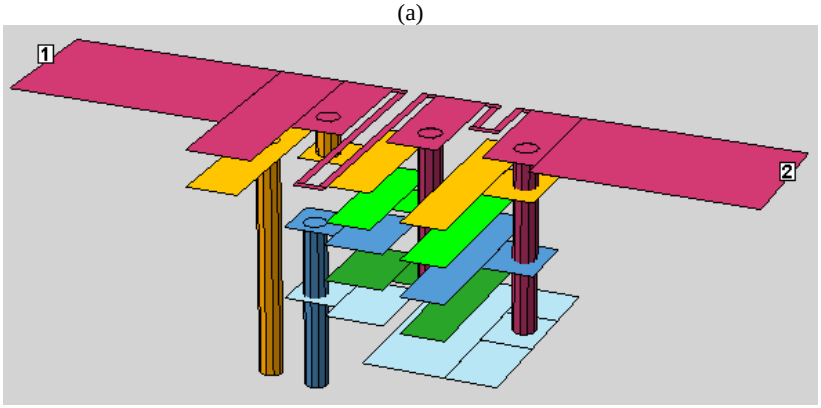

(b)

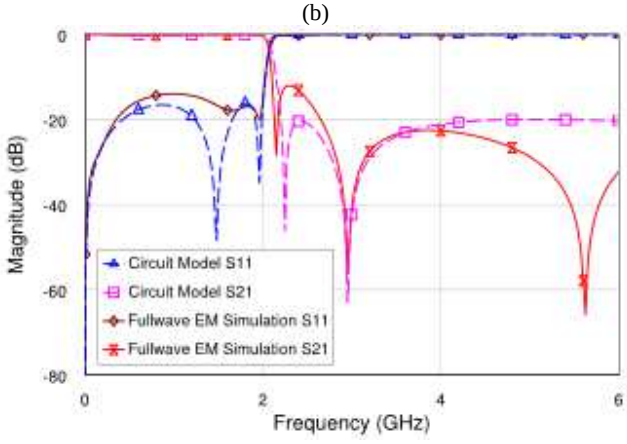

(b)

Fig. 2.17 (a) A modified lowpass filter design (C_1 = 1.29 pF, L_2 = 3.7 nH, C_2 = 0.7845 pF, C_3= 1.947 pF, C_4= 3.39 pF L_4 = 1.48 nH, C_5= 0.4632pF), (b) multilayer implementation and (c) circuit model and full wave EM simulation results

However, this will introduce more passive elements into the design, which would not only increase the size but also the insertion loss. As a compromise, the circuit prototype in Fig. 2.18 (a) is adopted as an improved design. Compared to the original circuit in Fig. 2.5 (a), this design adds only one more inductor L_3= 0.85 nH to each of the shunt branches and this works together with the shunt capacitor as a series resonator to the ground, which can produce another transmission zero in the stopband and keep the passband response almost unchanged as shown in the circuit simulation result in Fig. 2.18 (b). With this extra transmission zero, the stopband attenuation is improved from 10 dB to 18 dB up to 5.7 GHz, while the spurious band does not occur until 6 GHz, which is about 5 times of the centre frequency.

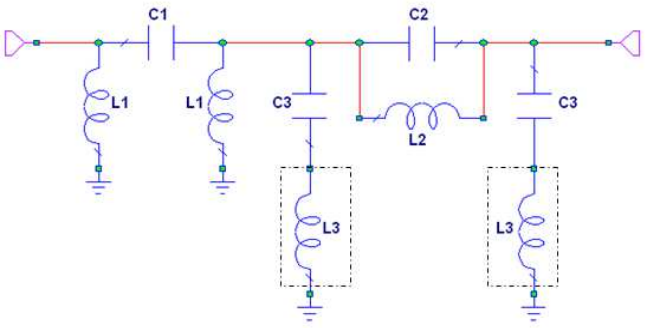

(a)

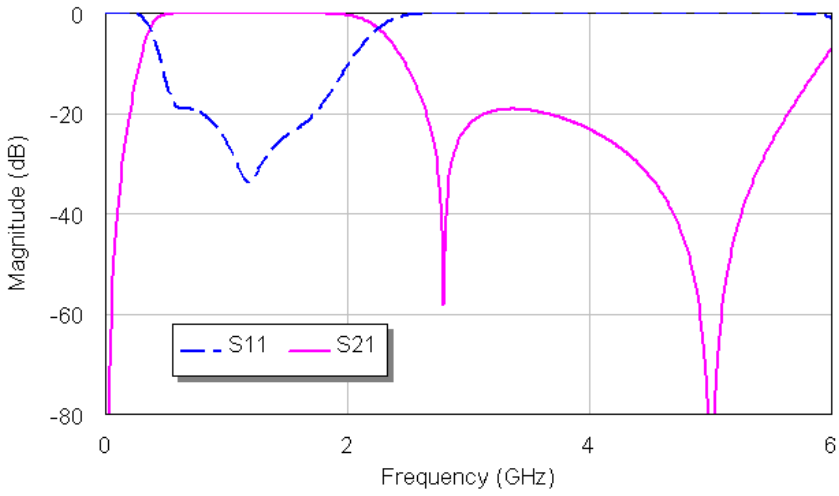

(b)

Fig. 2.18 (a) A modified circuit model and (b) Its circuit simulation result

Another advantage of this improved prototype is it is easy to implement the extra inductors on the original microstrip layout. It only changes the 4th layer with a pair of high

impedance lines as shown in Fig. 2.19(a). The total size is 10 mm × 4 mm × 0.6 mm, which is $0.065\lambda_g \times 0.026\lambda_g \times 0.004\lambda_g$, and λ_g is the guided wavelength on a 0.6 mm thickness substrate with dielectric constant 3, at the centre frequency of 1.25 GHz. This improved design has also been fabricated and the layout is almost the same as that shown in Fig. 2.16 (a). The filter is measured on a Hewlett Packard 8510B network analyser and the result is shown in Fig. 2.19(b). It can be seen that the passband has better than 13 dB return loss and 0.7 dB insertion loss. The upper stopband has been improved with better than 17 dB attenuation up to 6 GHz and 10 dB attenuation is achieved until 7 GHz. The measured group delay also matches the simulation with a variation within 0.3 ns. Compared to the circuit simulation result, there is a little frequency shift in the higher cutoff and the stopband attenuation has been decreased slightly due to fabrication tolerance. From the measured result of the two filters in this work, it can be seen that due to the smaller size of the elements, the lowpass filter that controls the upper side of the passband is more sensitive to the fabrication tolerances. This explains why both measured results show slight frequency shifting at the higher cutoff.

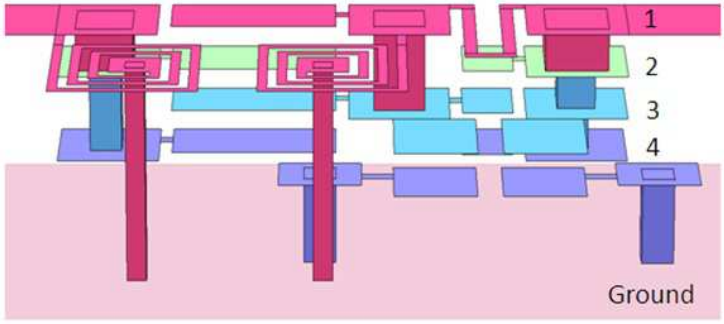

(a)

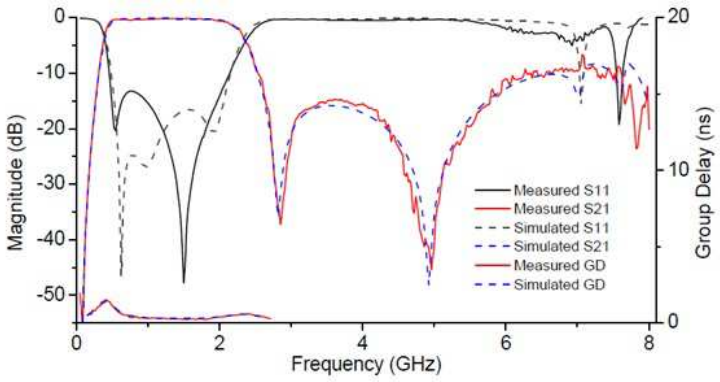

(b)

Fig. 2.19 (a) 3D structure of the improved design (b) Measured and circuit simulated response of the improved design

2.5. Conclusion

In this chapter, two compact high performance ultra-wideband filters have been designed and fabricated using the promising multilayer LCP technology. With the presented design approach, the values of microstrip lumped elements can be accurately extracted and the whole filter can be then designed efficiently with less EM optimisation. In addition, both designs are very compact and of high performance. Both filters have very wide spurious-free stopband up to 6 GHz. Transmission zeroes have been generated by the filter topology to improve the selectivity and stopband attenuation.

Another contribution of the work in this chapter is that a five-metal-layer LCP filter is presented for the first time, as all previous designs in open literature only use maximally 3 metal layers. This brings new challenges to the fabrication of multilayer LCP devices. To tackle this, new fabrication technique has been developed to reduce the registration error. Stepped via connections are also developed in this work to provide reliable connections. The agreement between measured and simulated results proves the usefulness of these fabrication techniques.

However, further size reduction can still be achieved in future. In this design, via hole sizes are relatively large as it is needed for the stepped via connection. This also results in very large via patches. To reduce the size of vias, new laser machining technique and via hole plating technique would be needed. In addition, although the second fabricated filter can produce two transmission zeros, it is still a third order bandpass filter. To improve the performance further, efficient high order prototypes need to be developed, which will be introduced in the next chapter.

References

[2.1] G. Matthaei, L. Young and E. M. T. Jones, *Microwave Filters, Impedance-Matching Networks, and Coupling Structures*, Artech House, Norwood, MA, 1980.

[2.2] J.-S. Hong, *Microstrip Filters for RF/Microwave Applications*, 2nd Edition. New Jersey: Wiley, 2011.

[2.3] Y.-X. Guo, L.C. Ong and M. Y. W. Chia and B. Luo, “Dual-Band Bandpass Filter in LTCC”, in *IEEE MTT-S Int. Microw. Symp. Dig.*, 2005, pp. 2219-2222.

[2.4] H. Joshi and W. J. Chappell, “Dual-Band Lumped-Element Bandpass Filter”, *IEEE Trans. Microw. Theory Tech.*, vol.. 54, no. 12, pp. 4169-4177, Dec. 2006.

[2.5] M. Hoft and T. Shimamura, “Design of Symmetric Trisection Filters for Compact Low-Temperature Co-Fired Ceramic Realization,” *IEEE Trans. Microw. Theory Tech.*, vol 58, no. 1, pp. 165-175, Jan. 2010.

[2.6] C.-W. Tang and D.-L. Yang, “Realization of Multilayered Wide-Passband Bandpass Filter With Low-Temperature Co-Fired Ceramic Technology,” *IEEE Trans. Microw. Theory Tech.*, vol. 56, no. 7, pp. 1668-1674, Jul. 2008.

[2.7] T. H. Duong and I. S. Kim, “New Elliptic Funtion Type UWB BPF Based on Capacitively Coupled λ/4 Open T Resonator,” *IEEE Trans. Microw. Theory Tech.*, vol., 57, no. 12, pp. 3089 – 3098, Dec. 2009.

[2.8] S. Hwang, S. Min, M. Swaminathan, V. Venkatakrishnan, H. Chan, F. Liu, V. Sundaram, S. Kennedy, D. Baars, B. Lacroix, Y. Li and J. Papapolymerou, “Characterization of next generation thin low-k and low-loss organic dielectrics from 1 to 110GHz,” *IEEE Trans. Adv. Packag.*, vol. 33, no. 1, pp. 180-188, Feb. 2010.

[2.9] S. Hwang, S. Min, M. Swaminathan, V. Sundaram and R. Tummala, “Thin-Film High-Rejection Filter Integration in Low-Loss Organic Substrate,” *IEEE Trans. Compon. Packag. Manufacturing. Tech.*, vol. 1, no. 8, pp. 1160-1170, Aug. 2011.

[2.10] K. Brownlee, S. Bhattacharya, K. Shinotani, C. P. Wong, and R. Tummala, “Liquid crystal polymer for high performance SOP applications,” in *8th IEEE Int. Adv. Packag. Mater. Symp.*, Mar. 3–6, 2002, pp. 249–253.

[2.11] D. C. Thompson, O. Tantot, H. Jallageas, G. E. Ponchak, M. Tentzeris, and J. Papapolymerou, “Characterization of liquid crystal polymer (LCP) material and transmission lines on LCP substrate from 30–100 GHz,” *IEEE Trans. Microw. Theory Tech.*, vol. 52, no. 4, pp. 1343–1352, Apr. 2004.

[2.12] Z.-C. Hao and J.-S. Hong, “Ultra-Wideband Bandpass Filter Using Multilayer Liquid-Crystal-Polymer Technology,” *IEEE Trans. Microw. Theory Tech.*, vol. 56, no. 9, pp. 2095-2100, Sept. 2008.

[2.13] Z.-C. Hao and J.-S. Hong, “UWB Bandpass Filter Using Cascaded Miniature High-Pass and Low-Pass Filters With Multilayer Liquid Crystal Polymer Technology,” *IEEE Trans. Microw. Theory Tech.*, vol. 58, no. 4, pp. 941-948, Apr. 2010.

[2.14] Z.-C. Hao and J.-S. Hong, “Ultra Wideband Bandpass Filter Using Embedded Stepped Impedance Resonators on Multilayer Liquid Crystal Polymer Substrate,” *IEEE Microw. Wireless Compon. Lett.*, vol. 18, no. 9, pp. 581-583, Sept. 2008.

[2.15] Z.-C. Hao and J.-S. Hong, “Compact Wide Stopband Ultra Wideband Bandpass Filter Using Multilayer Liquid Crystal Polymer Technology,” *IEEE Microw. Wireless Compon. Lett.*, vol. 19, no. 5, pp. 290–292, May 2009.

[2.16] G. –S. Huang, Y.-S. Lin, C.-H. Wang and C. H. Chen, “A Novel Transition-Included Multilayer Filter.” *IEEE Trans. Microw. Theory Tech.*, vol. 57, no. 4, pp. 807-814, April 2009.

[2.17] Inder Bahl, *Lumped Element for RF and Microwave Circuits*. Boston: Artech House, 2003.

[2.18] G. Brzezina, L. Roy, L. MacEachern, “A Miniature LTCC Bandpass Filter Using Novel Resonators for GPS Applications,” *in Proc. 37th European Microw. Conf.*, Oct. 2007, pp. 536-539.

[2.19] S. S. Mohan, M. del Mar Hershenson, S. P. Boyd and T. H. Lee, ‘‘Simple Accurate Expressions for Planar Spiral Inductances,’’ *IEEE J. Solid-State Circuits*, vol. 34, no. 10 , pp. 1419–1424, October 1999.

[2.20] AWR Microwave Office, Appl. Wave Res. Inc., Version 2009, El Segundo, CA, 2007.

[2.21] Sonnet *em*, Version 13.54, Sonnet Software Inc., New York, 2011.

[2.22] “Fabrication Guidelines ULTRALAM-3000-LCP-Materials,” Rogers Corporation, Connecticut, USA, 2012.

Chapter 3

A Miniature Ultra-wideband Filters Using a Novel and Efficient Circuit Model

3.1. Introduction

In previous chapter, a compact and high performance ultra-wideband (UWB) filter has been designed using multilayer LCP technology. The numbers of total elements in the designs are listed in Table 3.1. It can be seen that although both designs does not deploy too many elements, the number of reflection zeroes was only 3. Although the design in Fig. 2.18 (a) was introduced as an improved design to produce an extra transmission zero, as a compromise, it did not increase the number of reflection zeroes.

	Design in Fig. 2.5 (a)	Design in Fig. 2.18 (a)
Highpass Filter	3	3
Lowpass Filter	4	6
In Total	7	9
Number of Transmission Zeros	1	2
Number of Reflection Zeros (Poles)	3	3

Table 3.1 Number of elements in circuit models for the designs in Chapter 2

In this chapter, a novel circuit model, to the best of the author's knowledge, for an ultra-wideband filter will be introduced to produce a better performance than the design in Fig.2.18 (a), but still use the same number of components. As a collaboration project with the Department of Microelectronics& Radio Engineering, Saint Petersburg ElectroTechnical University, this work is designed for the 3.1-10.6 GHz band, which was released by the U.S. Federal Communications Commission (FCC) in 2002 for the unlicensed use for indoor and handheld ultra-wideband (UWB) systems [3.1]. However, the design approach can be easily applied to design filters at other frequencies.

For this UWB band, lots of designs have been reported in open literature. In [3.2, 3.3], multi-mode resonators were introduced to the design of UWB bandpass filters, where

multiple resonating modes are produced by one resonator structure. This can reduce the number of resonators needed to design a UWB filter. Microstrip and co-planar hybrid structures, where cross coupling can be easily implemented, are used to design compact UWB filter with finite frequency transmission zeroes [3.4, 3.5]. Optimum stub filters, introduced in [3.6] and [3.7], have also been used to design UWB filters in [3.8] and [3.9]. This type of filters had no redundant connection lines, and this makes it possible to design a high order filter with less number of stubs.

Although the above designs use different ways to reduce the number of elements needed for the design of UWB filters, they are all based on distributed elements. In this chapter, a novel lumped-element circuit model will be developed to design compact UWB filters. The circuit model is efficient and can produce 4 reflection and 2 transmission zeroes. In addition, the filter has a very simple multilayer structure, which is very suitable for low cost mass production for practical applications. In Section 3.2, the novel circuit model will be introduced and its synthesis is also detailed. A comparison between this design and other conventional designs will be made in Section 3.3. Several samples of this design have been fabricated and their measurements are shown in Section 3.4. This is then followed by a conclusion and suggestion for future work in Section 3.5.

3.2. A Novel Circuit Model for Bandpass Filters

To produce a UWB bandpass response with less than -20 dB return loss and a 3 dB bandwidth from 3.1 GHz to 10.6 GHz, a multilayer lumped element circuit model is used in this work, as shown in Fig. 3.1 (a) and its simulation response [3.10] is shown in Fig. 3.1 (b).

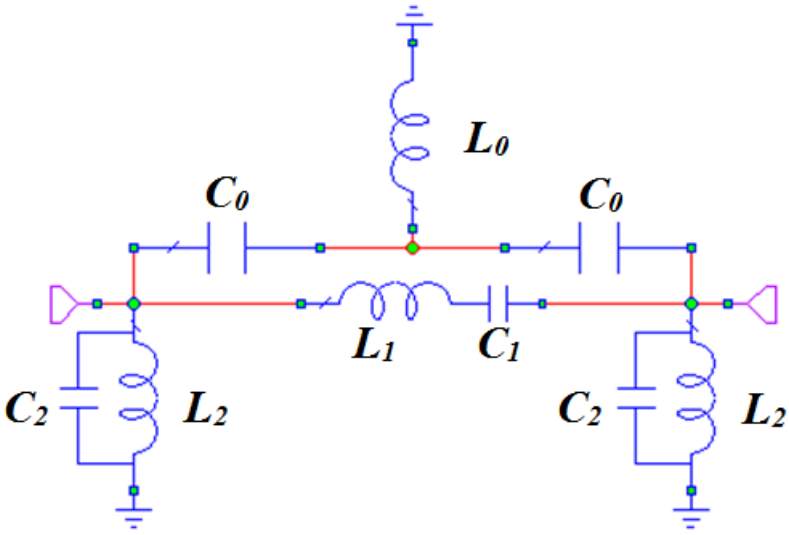

(a)

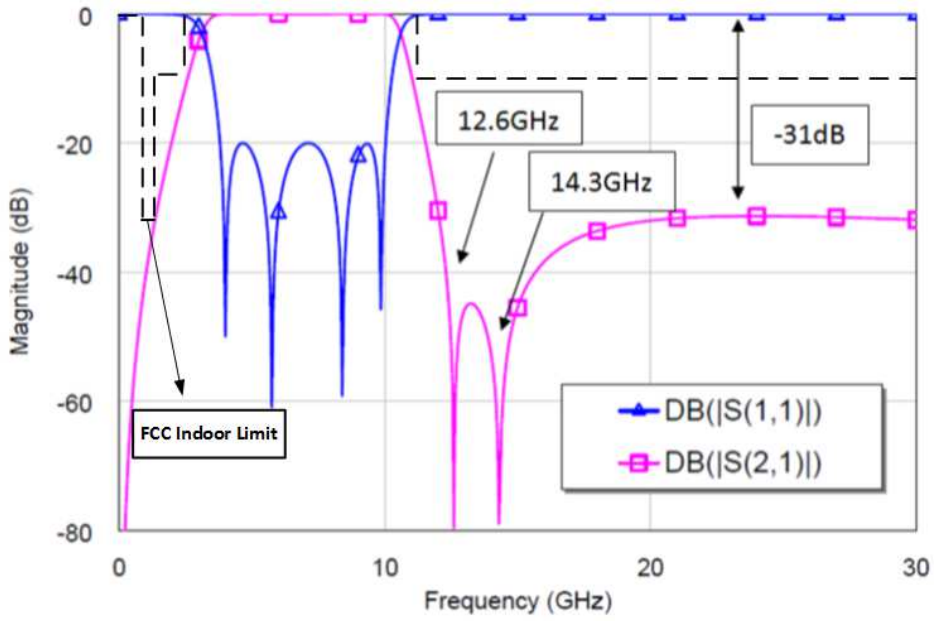

(b)

Fig. 3.1 (a) Proposed circuit model (b) Theoretical circuit simulation response for L_0=1.813 nH, C_0 = 0.0716 pF, L_1=2.119 nH, C_1= 0.499 pF, L_2=1.449 nH, and C_2=0.459 pF

The idea of this design comes from a traditional lumped element bandpass design as shown in Fig. 3.2 (a) [3.7]. This circuit is obtained directly from a Chebyshev lowpass prototype through frequency and element transformation. It is then well know that, by introducing a cross coupling capacitor C_0 in Fig. 3.2 (b) [3.7], a transmission zero can be produced. To make the most of this topology, C_0 is replaced by a T network as shown in Fig. 3.2 (c). Compared with the simple cross coupled circuit in 3.2 (b), this topology does not only gives

an extra pole in the passband near the passband edge, but also provides a second transmission zero at 14.3 GHz in the stopband, which gives a high selectivity on the upper passband edge and a wide stopband with 31 dB attenuation theoretically, as shown in Fig. 3.2 (d).

To calculate the element values needed for this design. The circuit topology in Fig. 3.2 (c) can be transformed into a simplified circuit model as shown in Fig. 3.3 (a). The dash-circled T section is then transformed to the dash-circled Π section in Fig. 3.3 (b), by using T and Π circuit equivalence. Then it could be seen from Fig. 3.3 (b) that the circuit can eventually be simplified, by combining the Z_1 and Zp, Z_2 and Z_S, respectively, to a single Π shape circuit, of which the *ABCD* parameters and *S* parameters can be easily calculated.

With the *S21* parameter, by equating it to zero, the locations of the transmission zeroes can be obtained, which are represented by (3.1) and (3.2). It can be seen that, the locations of the transmission zeroes are only determined by the T network and the series LC resonator formed by L_1 and C_1. This actually means that in this circuit, the parallel branches Z_2 and Z_s are producing the transmission zeroes below represented by (3.1) and (3.2).

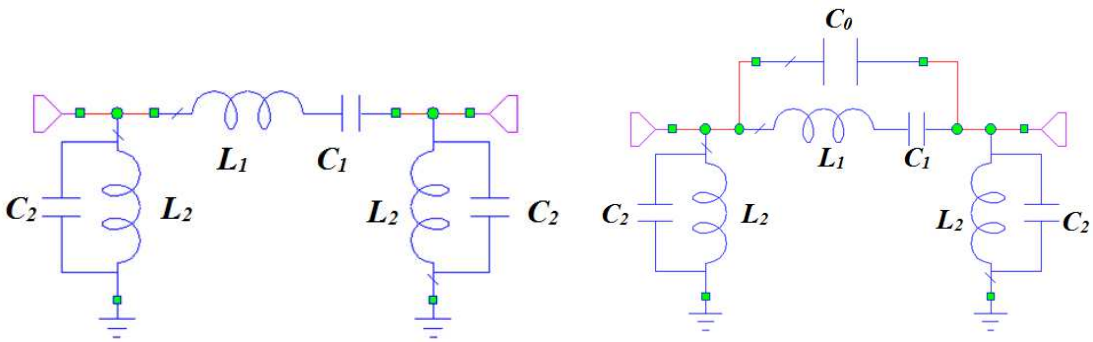

(a)

(b)

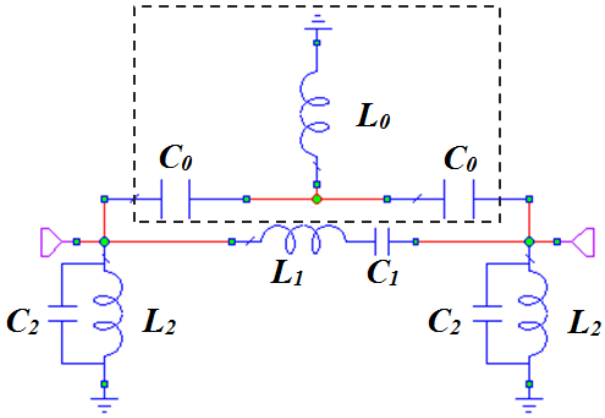

(c)

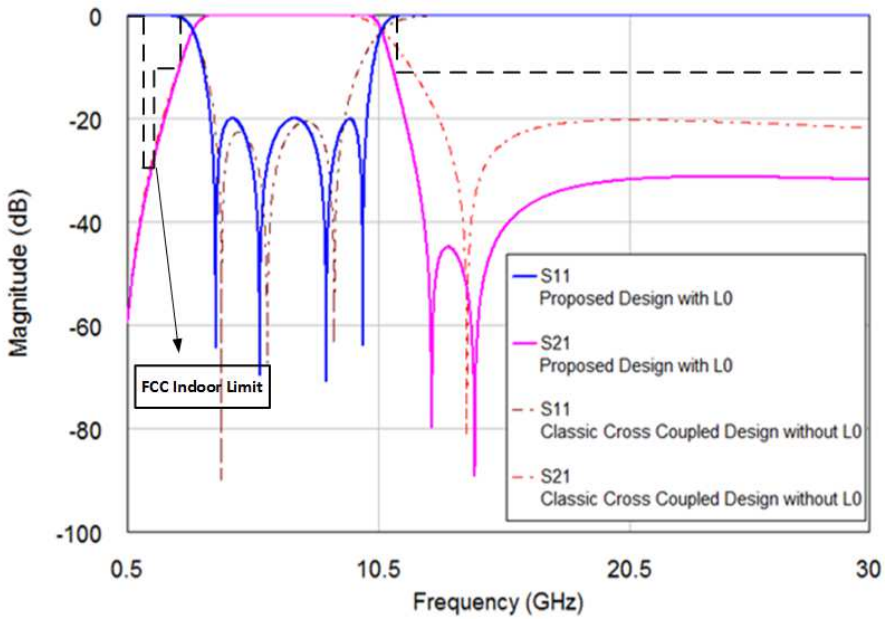

(d)

Fig. 3.2 (a) A Chebyshev bandpass filter (b) A conventional cross-coupled bandpass filter (c) the proposed filter with T network (d) simulated results of the proposed filter compared with a conventional cross-coupled bandpass filter

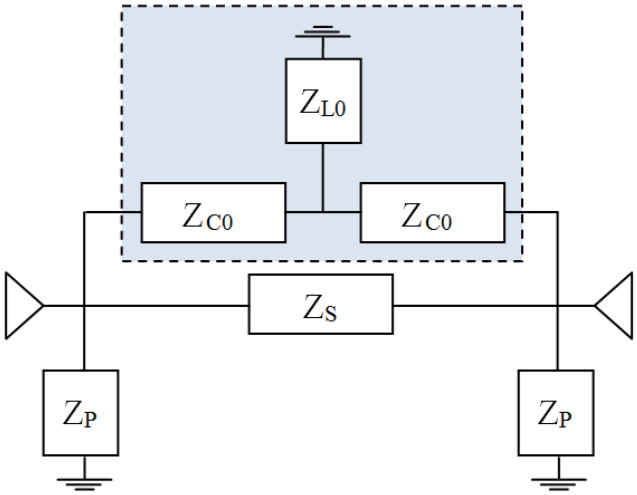

(a)

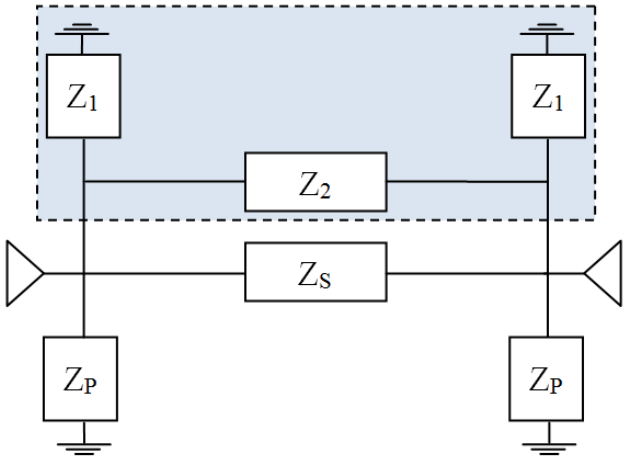

(b)

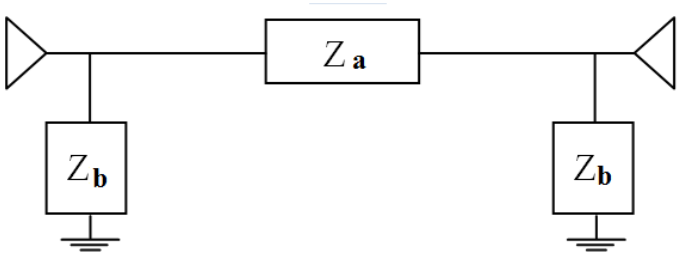

Fig. 3.3 (a) Impedance representations of the proposed circuit model (b) T to Π transformation (c) Simplified T network

$$\omega_{TZ1} = \sqrt{\frac{\frac{C_0}{2}L_0 + C_1L_0 - \sqrt{-L_0{C_1}^2L_1 + \left(C_1L_0 + \frac{C_0}{2}L_0\right)^2}}{C_0L_0C_1L_1}} \tag{3.1}$$

$$\omega_{TZ1} = \sqrt{\frac{\frac{C_0}{2}L_0 + C_1L_0 + \sqrt{-L_0{C_1}^2L_1 + \left(C_1L_0 + \frac{C_0}{2}L_0\right)^2}}{C_0L_0C_1L_1}} \tag{3.2}$$

It should be mentioned that this type of parallel resonance for producing transmission zeroes is also similar to the phase cancellation technique as has been used in [3.11], where distributed transmission lines are adopted for the designs and they are not suitable for miniature circuit design.

To obtain the values for all the LC components, CAD tools [3.10] is used for optimisation. By using (3.1) and (3.2) and a trial value for L_1, L_0 and C_0 can be calculated. Then all the other values in the schematic can be chosen to have similar values as a conventional cross coupled bandpass filter in Fig. 3.2 (b). Table 3.2 shows the value before and after optimisation.

	C_0 (pF)	L_0 (nH)	C_1 (pF)	L_1 (nH)	C_2 (pF)	L_2 (nH)
Initial	0.091	1.75	0.045	1.9	0.45	1.5
Optimized	0.0716	1.813	0.3988	2.119	0.459	1.449

Table 3.2 Initial and optimized values

3.3. A Comparision with Other Conventional Designs

To indicate the advantages and drawbacks of this design, it can be compared with a few conventional design techniques.

1) Chebyshev filters, in T or Π forms, can be easily designed using g - parameters to obtain required passband return loss, number of poles and equal ripple bandwidths. However, such a conventional design won't produce transmission zeroes. In addition, for a 4-pole Chebyshev bandpass filter, although it only consists of 8 elements, it requires asymmetrical circuit model and may need the two ports impedance to be different [3.12], which may be not convenient for practical applications.

2) Coupled resonator theory [3.13] is another classic method and very useful for designing bandpass filters with transmission zeroes. However, this design method is more suitable for narrow band design. In terms of the number of elements, a 4-pole coupled resonator filter with 2 transmission zeroes in the upper stopband may need 4 *LC* resonators (8 elements), 3 inter-resonator coupling elements, 2 cross coupling elements and at least 2 input/output matching elements, while the proposed design in this paper uses 9 elements in total.

However, the novel circuit model in this work also has its drawback. Classic design techniques as mentioned above are very flexible and they can be used to design a filter with any number of poles theoretically. The proposed design is a 4-pole filter with 2 transmission zeroes. If a higher order response is required, a cascaded design can be easily formed. However, it would also be interesting to investigate the possibility of designing this type of higher order bandpass filter directly in future.

3.4. Implementation and Measurement

The proposed filter design is implemented on multilayer LCP substrates. The fabrication process has been detailed in Chapter 2. Since one of the main objectives of this design is to provide a simple UWB filter structure which can lead to low cost and high yield mass production, the implementation has been designed to be as simple as possible.

To achieve this objective, the schematic in Fig. 3.2 (c) has been re-arranged to the one in Fig. 3.4 (a), where the series capacitor C_1 in the main path has been split into two capacitors with values of ($2 \times C_1$), so that it results in a symmetric circuit topology. Then the circuit model can be implemented as a two-layer structure as shown in Fig. 3.4 (b) and its dimentions are in Fig. 3.4 (c) and (d). It can be seen that, with such a symmetric circuit model in Fig. 3.4 (a), the series capacitor C_1 in the series path would no longer needed to be implemented with connection vias as shown in Fig. 3.5. This simplifies the circuit structure and also reduces the fabrication cost for mass production.

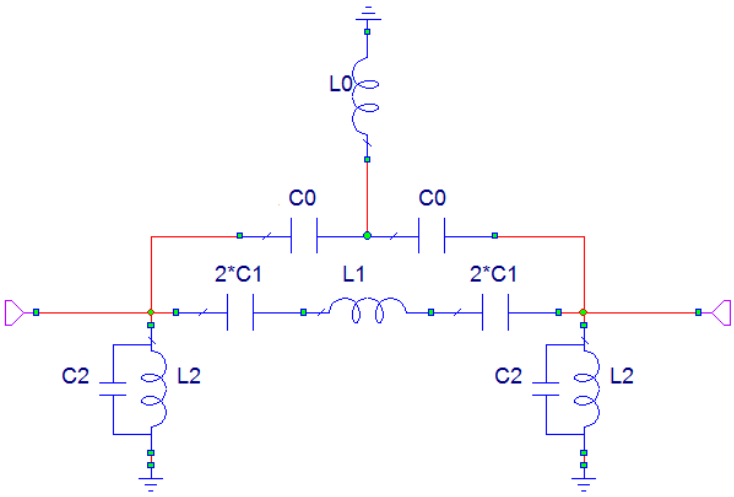

(a)

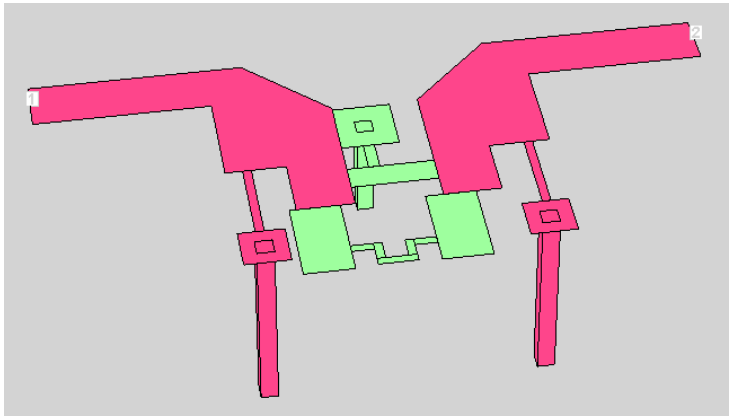

(b)

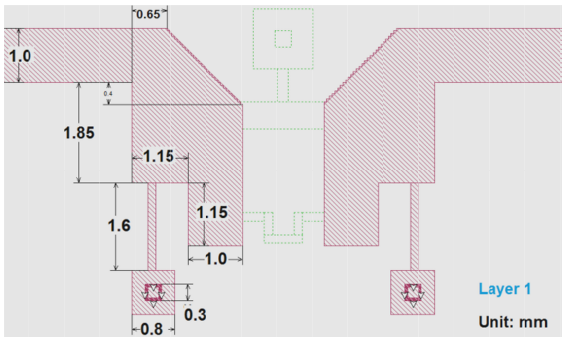

(c)

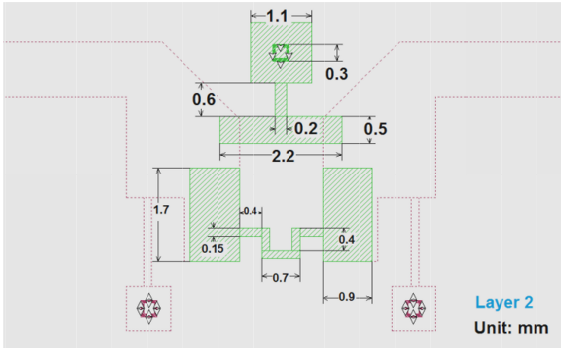

(d)

Fig. 3.4 (a)Modified circuit model (b) A two-layer implementation (c) top layer and (d) second layer dimensions

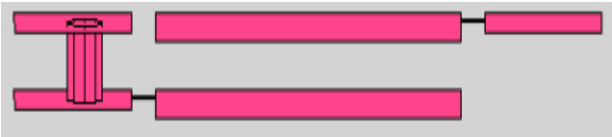

Fig. 3.5 A two-layer broadside-coupled capacitor

However, there is also a drawback for this type of implementation. For the proposed structure in Fig. 3.4 (a), a total capacitance of ($4 \times C_1$) has to be implemented in a broad-side coupled way, while originally only C_1 needs to be implemented. This would lead to a larger coupling area with a lower self-resonant frequency.

For the very small value of C_0, any poor fabrication tolerance can lead to a large frequency shift for the transmission zeroes. As shown in Fig. 3.4 (c) and (d), the copper patch on the 2nd layer for capacitor C_0 is much smaller than the one on the top layer. This can lead to less capacitance change in case of alignment errors during the lamination process.

Fig. 3.6 shows the full wave EM simulation result obtained from a commercial simulator [3.14] compared with the ideal circuit response from Fig. 3.1 (b). The EM simulation result is in a good agreement with the circuit response in the passband. However, owing to some parasitic effects of the quasi-lumped elements implemented, only one transmission zero is observed in the upper stopband, which results in 23 dB stopband attenuation instead of 31 dB from Fig. 3.1 (b).

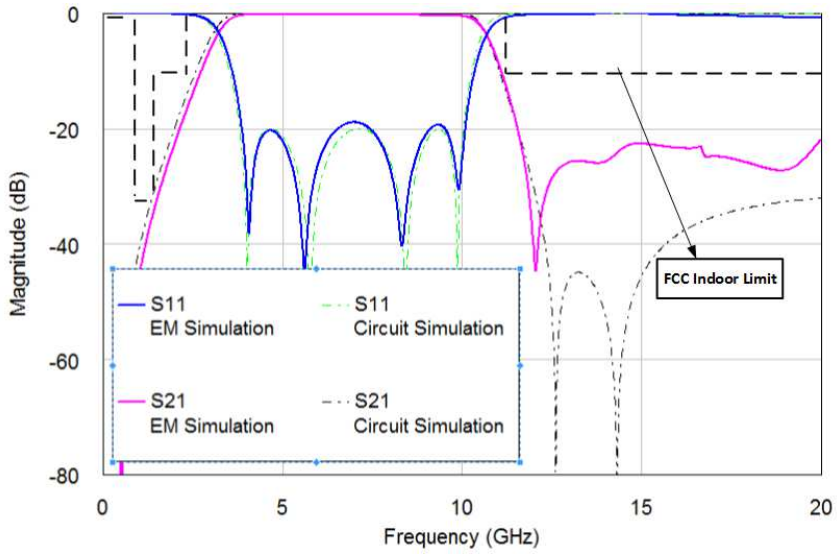

Fig. 3.6 Full wave EM simulation (solid lines) compared with circuit simulation (dashed lines)

The proposed circuit is fabricated as shown in Fig. 3.7 (a). The size of the filter excluding the 50 Ohm feed line is 5.6 mm × 5.6 mm × 0.4 mm, which is $0.2\lambda_g \times 0.2\lambda_g \times 0.014\lambda_g$, where λ_g is the guided wavelength at the UWB centre frequency of 6.85 GHz. Compared with the previous miniature LCP UWB filter in [3.15], it occupies 30% less planar area with similar performance.

The circuit is connected with Anritsu 3680 Test Fixture and measured on a HP8510 Network Analyser. The measured result compared with simulation is shown in Fig. 3.7 (b), from which it can be seen that the measurement agrees with simulation very well. It has less than 0.3 dB mid-band insertion loss, 15 dB return loss and 21 dB out-of-band rejection. It also produces very flat group delay as shown in Fig. 3.7 (c), and the variation between 4GHz and 10GHz, which is about 80% of the whole passband, is within 0.1nS. In addition, for this design, 3 samples have been fabricated and measured. They are all in good agreement with the simulation as shown in Fig. 3.8 and demonstrate a high yield of the fabrication of the filter.

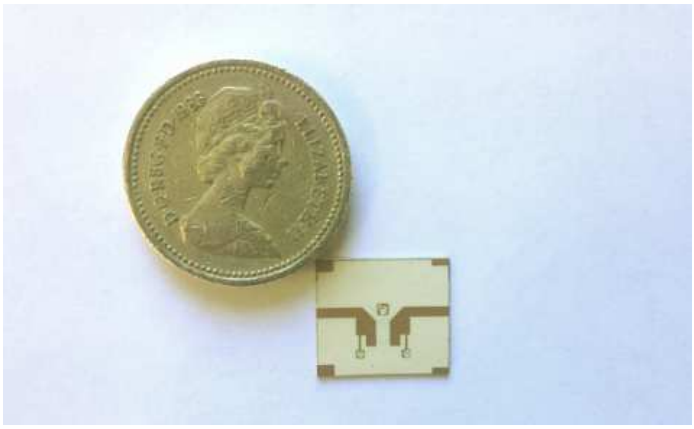

(a)

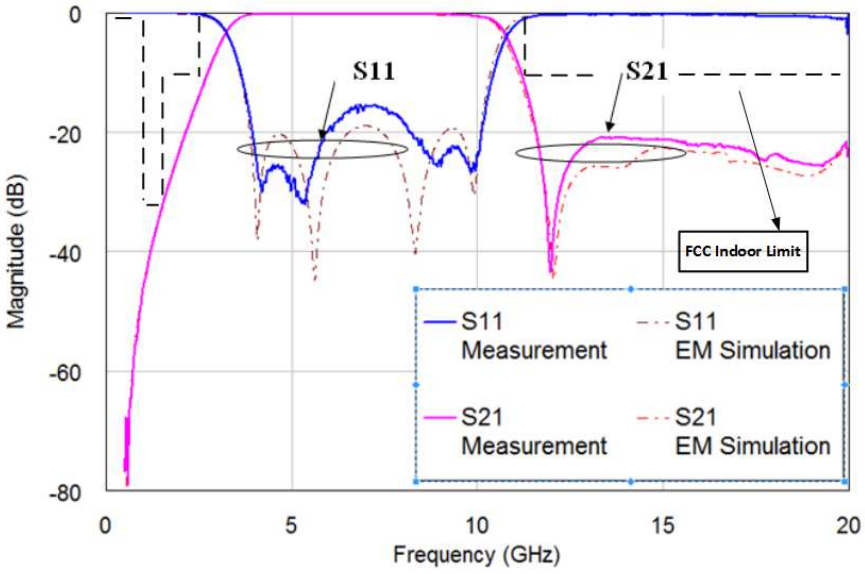

(b)

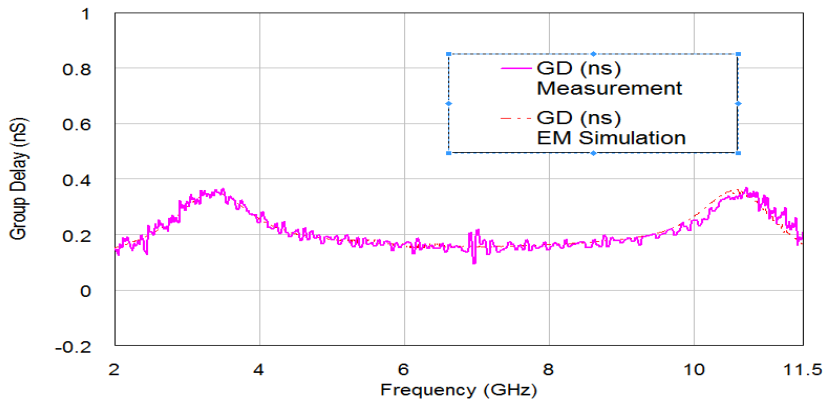

(c)

Fig. 3.7 (a) Photo of a fabricated sample (b) S parameters and (c) Group Delay comparison between measurements and EM simulations.

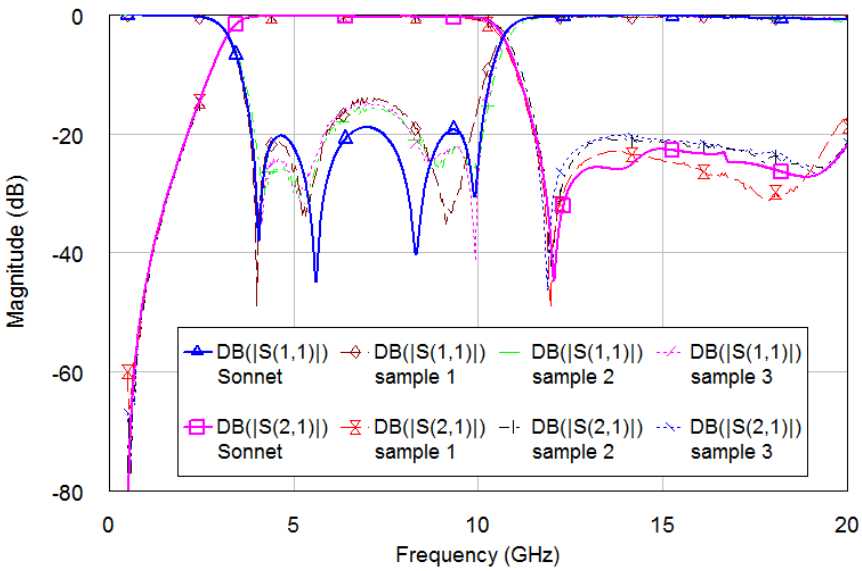

Fig. 3.8 Measurement results of all fabricated samples.

3.5. Conclusion and Suggestions for Future Work

As an extension of the work in Chapter 2, this chapter introduces a different circuit model for the design of lumped-element UWB filter. The circuit model has only 9 elements but it is capable of producing 4 reflection and 2 transmission zeroes, while in previous chapter, a filter with 3 reflection and 2 transmission zeroes needs 10 elements.

The multilayer implementation of the filter is also very interesting. It eliminates the need of connection vias between two circuit layers. This leads to a simple fabrication. The measurements of all fabricated samples are in good agreement with the simulation, which indicates that the proposed design is a very good candidate for mass production for practical UWB systems.

However, as a preliminary study for this novel circuit model, only a 4-pole design is presented. Some further work can be done to develop a systematic approach to design high performance and compact UWB filters with frequency response of higher orders.

References

[3.1] “Revision of part 15 of the Commision’s rules regarding ultra-wideband transmission system,” FCC, Washington, DC, Tech. Rep. ET-Docket 98-153 FCC02-48, 2002.

[3.2] L. Zhu, S. Sun, and W. Menzel, “Ultra-wideband (UWB) bandpass filter using multiple-mode resonator,” *IEEE Microwave Wireless Compon. Lett.*, vol. 15, no. 11, pp. 796–798, Nov. 2005.

[3.3] S. W. Wong and L. Zhu, “Quadruple-mode UWB bandpass filter with improved out-of-band rejection,” *IEEE Microwave Wireless Compon. Lett.*, vol. 19, pp. 152–154, Mar. 2009.

[3.4] H. Wang, L. Zhu, and W. Menzel, “Ultra-wideband (UWB) bandpass filter with hybrid microstrip/CPW structure,” *IEEE Microwave Wireless Compon. Lett.*, vol. 15, no. 12, pp. 844–846, Dec. 2005.

[3.5] N. Thomson and J.-S. Hong, “Compact ultra-wideband microstrip/coplanar waveguide bandpass filter,” *IEEE Microwave Wireless Compon. Lett.*, vol. 17, no. 3, pp. 184–186, Mar. 2007.

[3.6] R. Levy, “A new class of distributed prototype filters with applications to mixed lumped/distributed component design,” *IEEE Trans.*, *MTT-18*, Dec. 1970, 1064-1071.

[3.7] J.-S. Hong, *Microstrip Filters for RF/Microwave Applications*, 2nd Edition. New Jersey: Wiley, 2011.

[3.8] J.-S. Hong and H. Shaman, “An optimum ultra-wideband microstrip filter,” *Microwave Opt. Technol. Lett.*, vol. 47, no. 3, pp. 230–233, Nov. 2005.

[3.9] H. Shaman and J.-S. Hong, “A novel ultra-wideband (UWB) bandpass filter (BPF) with pairs of transmission zeroes,” *IEEE Microwave Wireless Compon. Lett.*, vol. 17, no. 2, pp. 121–123, Feb. 2007.

[3.10] AWR Microwave Office, Appl. Wave Res. Inc., Version 2009, El Segundo, CA, 2007.

[3.11] R. G´omez-Garc´ıa and J. I. Alonso, “Design of sharp-rejection and lowloss wide-band planar filters using signal-interference techniques,” *IEEE Microw. Wireless Compon. Lett.*, vol. 15, no. 8, pp. 530–532, Aug. 2005.

[3.12] G. Matthaei, L. Young and E. M. T. Jones, *Microwave Filters, Impedance-Matching Networks, and Coupling Structures*, Artech House, Norwood, MA, 1980.

[3.13] R. J. Cameron, R. Mansour and C. M. Kudsia, *Microwave Filters for Communication Systems: Fundamentals, Design and Applications*. New York: Wiley, 2007.

[3.14] Sonnet *em*, Version 13.54, Sonnet Software Inc., New York, 2011.

[3.15] Z.-C. Hao and J.-S. Hong, "Ultra-Wideband Bandpass Filter Using Multilayer Liquid-Crystal-Polymer Technology," *IEEE Trans. Microw. Theory Tech.*, vol. 56, no. 9, pp. 2095-2100, Sept. 2008.

Chapter 4
Miniature Bandpass Filters with Moderate/Narrow Bandwidths and Excellent Stopband Performance

4.1. Introduction

In previous chapters, the design and fabrication of ultra-wideband (UWB) filters using multilayer LCP technologies were discussed. However, as a popular low cost multilayer solution for compact microwave devices, liquid crystal polymer (LCP) has not been involved in the design of bandpass filters with moderate/narrow bandwidths. In particular at a low RF band such as the very high frequency (VHF) band, where it is essential to reduce the size of planar RF components.

For such moderate/narrow-band applications, it is not only required the bandpass filter to have very good passband performance, such as low insertion loss, but also a very good stopband performance, such as high selectivity near the passband edges, wide stopband with high attenuation to suppress the interference from other systems.

In order to design narrowband filters, coupled resonator circuits and their derivations are the most popular candidates. The development of such type of filters started with direct-coupled-resonator filters to produce the all-pole bandpass response [4.1]. Then the theory was applied to different types of resonators and couplings in [4.2]-[4.7]. Recently, with the development of advanced material and fabrication technologies, novel coupled resonator filters have been designed. In [4.8] and [4.9], substrate integrated waveguide (SIW) cavities and high temperature superconductors are used, respectively, to reduce the insertion loss of filters. In [4.10] and [4.11], MMIC and CMOS technologies make it possible to implement advanced filters in a very small format. Multilayer low temperature co-fired ceramic (LTCC) filters are designed in [4.12] and [4.13] as a low cost and high performance solution.

LCP, another multi-layer solution has a number of advantages over LTCC, which include: low-cost and low processing temperature. This makes it desirable to investigate the performance of LCP for applications requiring moderate/narrow bandwidths. There have been to the author's knowledge, previous multilayer LCP designs presented [4.14, 4.15],

however these are for ultra-wideband applications. Furthermore in [4.16], a second order narrowband bandpass filter was designed on LCP; but no fabrication and measurement were done to investigate the real performance, such as insertion loss and fabricated quality (Q) factors of LCP filters with narrow/moderate bandwidths.

In this chapter, a multilayer LCP bandpass filter centred at 250MHz, with a fractional bandwidth (FBW) of 20%, is presented. Section 4.2 describes the synthesis procedure of the proposed design and its physical implementation on multilayer LCP substrates. Section 4.3 gives a short comparison between this design and other conventional topologies to demonstrate its superior stopband performance. Section 4.4 shows the LCP implementation of this design. A fabricated LCP sample and its measured response are presented in Section 4.5. This is followed by a short conclusion in Section 4.6.

4.2. Filter Synthesis

For this work, a 4th order bandpass filter is designed with a centre frequency of 250 MHz and equal ripple *FBW* of 20%. The passband return loss is better than -20 dB, which is equivalent to passband ripple of 0.043 dB. This specification and its corresponding Chebyshev lowpass prototype element values are listed in Table 4.1.

FBW	Z_0	ω_0	Passband Ripple	*g0*	*g1*	*g2*	*g3*	*g4*	*g5*
20%	50Ω	250 MHz	0.043 dB	1	0.9314	1.2920	1.5775	0.7628	1.2210

Table 4.1 Element Values for 4th order Chebyshev lowpass prototype filters

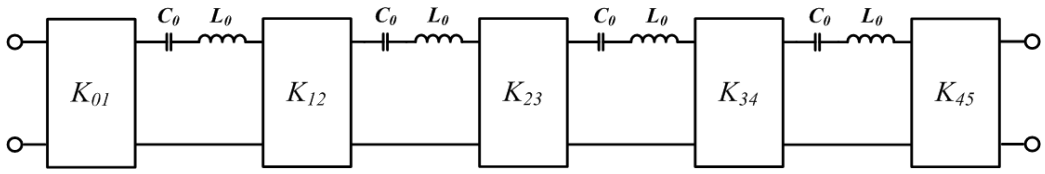

Fig. 4.1 A 4th order coupled-series-resonator bandpass filter

The design starts with a conventional 4-pole coupled-series-resonator filter in Fig. 4.1, where $K_{j,j+1}$ denotes the impedance inverters between any two adjacent series resonators. To calculate all the parameters, L_0 is chosen to be 45nH first, then C_0 and $K_{j,j+1}$ can be calculated using (4.1)-(4.4) [4.18]. For coupled series resonators, capacitive or inductive T-shape impedance inverters, as shown in Fig. 4.2 (a) or (b), respectively, can be used to replace the ideal frequency-independent inverters, although these practical inverters would

only have the same performance as ideal inverters at one frequency only, which will be discussed in later sections.

$$C_0 = \frac{1}{{\omega_0}^2 L_0} \tag{4.1}$$

$$K_{01} = \sqrt{\frac{Z_0 FBW \omega_0 L_0}{g_0 g_1}} \tag{4.2}$$

$$K_{j,j+1} = FBW \omega_0 L_0 \sqrt{\frac{1}{g_j g_{j+1}}}, j = 1, 2, 3 \tag{4.3}$$

$$K_{45} = \sqrt{\frac{Z_0 FBW \omega_0 L_0}{g_4 g_5}} \tag{4.4}$$

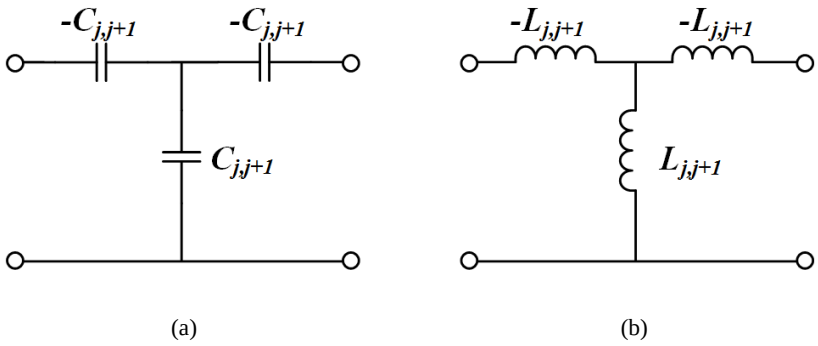

Fig. 4.2 T-shape impedance inverters: (a) capacitive and (b) inductive

4.2.1. Series Resonators with T-shape Inductive Inverters

Normally, it is preferable to use inductive T-shape inverters with series resonators as shown in Fig. 4.3 (a). In this schematic, inverters placed between any two adjacent resonators are of the form of Fig. 4.2 (b) and their element values can be easily calculated using (4.5) [4.18]. However, inverters at the input and output could not be implemented in the same way, as there is no reactance to absorb the negative inductance/capacitance at the input and output. To solve this problem, for the input inverter for instance, it could be assumed that the T network in Fig. 4.4 (b) is the equivalent circuit of Fig. 4.4 (a). By equating the real part of the input impedance Z_{in} looking into the left, (4.6) can be obtained. To remove the difficulty of obtaining L_{01} directly, L_{r0} can be introduced and (4.7) can be used to replace L_{s0} in (4.6). Then L_{01} can be obtained using (4.8). Then by equating the imaginary part, which should be zero, L_{s1} could be obtained using (4.9). At this stage, choose L_{r0} to be 30nH and then all the element values are known. By absorbing all the

negative inductances into adjacent series resonators, a filter schematic in Fig. 4.3 (b) can be obtained. It should be mentioned that by reviewing (4.5)-(4.9), it could be seen that all the calculations are done at the centre frequency ω_0 only. This explains why these inverters have identical performance as ideal inverters at a single frequency and are usually for narrowband applications. Thus an optimisation should be applied to obtain the desired performance, such as -20 dB return loss, over a relatively wide frequency range. Table 4.2 shows the calculated and optimised values of the L and C components in the circuit. All of these values are relatively small for filters operating at such a frequency and can be easily implemented on multilayer substrates. The simulation results of the schematic before and after optimisation are shown in Fig. 4.5 (a). However, by reviewing the schematic, it can be seen that all the shunt coupling inductors work as extra highpass elements. This is proved in Fig. 4.5 (b) by comparing the performance of the filter in Fig. 4.3 (b) with that of an ideal 4th order Chebyshev bandpass filter. It could be seen that the filter in Fig. 4.3 (b) gives a faster roll-off at the lower passband edge while slower at the upper edge.

$$L_{j,j+1} = \frac{K_{j,j+1}}{\omega_0} \text{ for } j = 1 \text{ to } 3 \tag{4.5}$$

$$L_{01} = \frac{K_{01}}{\omega_0}\sqrt{\frac{{Z_0}^2 + {\omega_0}^2(L_{s0} + L_{01})^2}{{Z_0}^2}} \tag{4.6}$$

$$L_{s0} = L_{r0} - L_{01} \tag{4.7}$$

$$L_{01} = \frac{K_{01}}{\omega_0}\sqrt{\frac{{Z_0}^2 + {\omega_0}^2{L_{r0}}^2}{{Z_0}^2}} \tag{4.8}$$

$$L_{s1} = \frac{{Z_0}^2 L_{01} + {\omega_0}^2(L_{r0} - L_{01})L_{01}L_{r0}}{{Z_0}^2 + {\omega_0}^2{L_{r0}}^2} \tag{4.9}$$

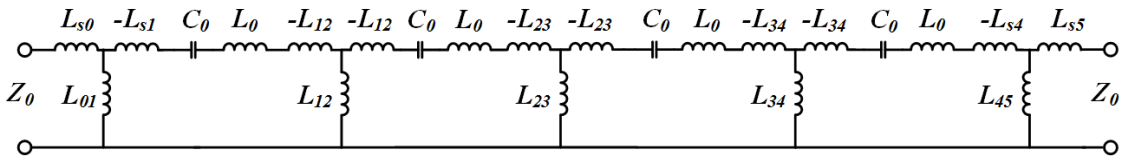

(a)

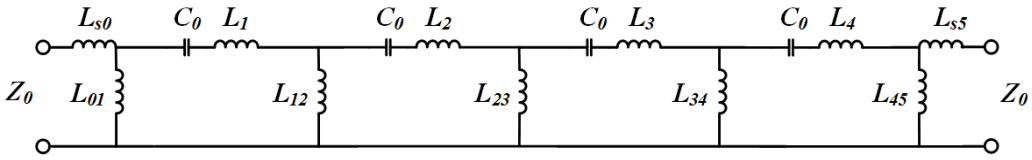

(b)

Fig. 4.3 A 4th order bandpass filter using series resonators and T-shape inductive inverters. (a) Initial Circuit. (b) Circuit after absorbing negative inductances.

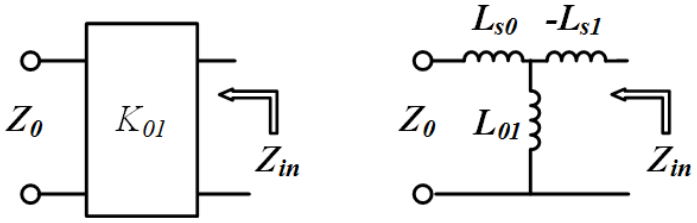

(a) (b)

Fig. 4.4 (a) Input coupling inverter and (b) its equivalent implementation

	C_0	L_1=L_4	L_2=L_3	L_{s01}=L_{s45}	L_{01}=L_{45}	L_{12}=L_{34}	L_{23}
Calculated	9.006 pF	21.8 nH	30.49 nH	5.9 nH	24.1 nH	8.204 nH	6.304 nH
After Optimization	9.006 pF	23.64 nH	32.04 nH	6.954 nH	23.02 nH	7.89 nH	6.38 nH

Table 4.2 The values of the 4-pole coupled-series-resonator filter with inductive inverters

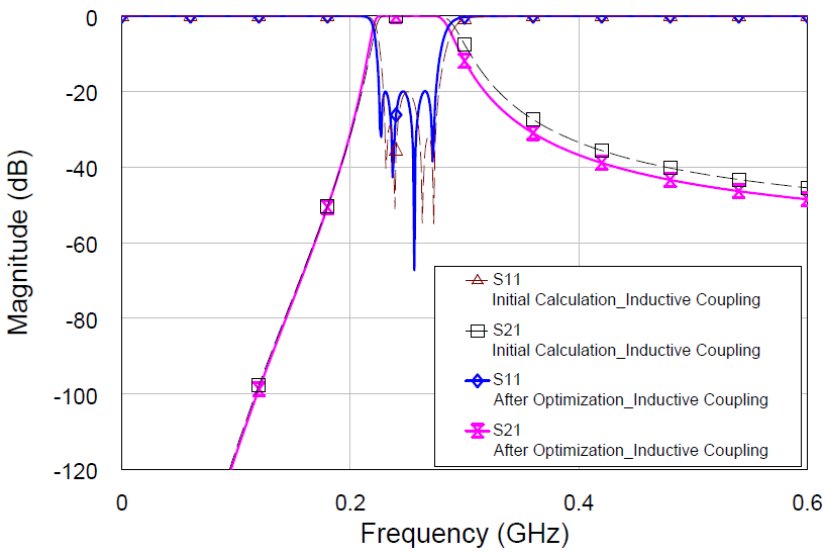

(a)

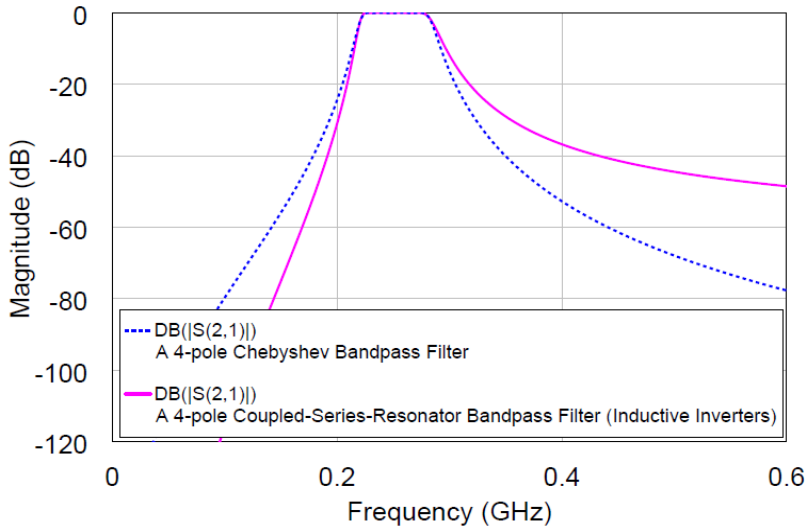

(b)

Fig. 4.5 A 4th order bandpass filter using series resonators and T-shape inductive inverters. (a) Its simulation results before and after optimization (c) Its selectivity in comparison with a conventional 4-pole Chebyshev bandpass filter

4.2.2. Series Resonators with T Shape Capacitive Inverters

The above design approach is quite straight forward as negative inductances can be easily absorbed considering the series connections. However, it would be interesting to test if T shape capacitive inverters could be used. Similarly to Fig. 4.3 (a), T-shape capacitive inverters are used to replace the ideal inverters in 4.6 (a) and (4.10) from [4.18] can be used to calculate the initial coupling elements values. Then using the same way as in Fig. 4.4, (4.11)-(4.12) to calculate the values of input elements and the output elements will have the

same values due to symmetry. However, considering (4.10), for a bandpass filter with a narrow/moderate bandwidth, $K_{j,j+1}$ would be small and thus the value of the coupling capacitor $C_{j,j+1}$ would be very large. Such large capacitance is difficult to implement even on multilayer substrates as they would have a very large size, which means they will have very low self-resonant frequency (SRF). Up to this point, filter designers would think that series resonators only naturally work well with T-shape inductive inverters other than capacitive inverters.

To solve this problem, the following procedure can be applied to the schematic in Fig.4.6 (a). Firstly, every resonator capacitor C_0 can be split into two series capacitors, each with a value of ($2 \times C_0$). They can then be used to absorb the negative capacitances from the original T-shape inverter and new T networks can be formed. T to Π transformations can then be applied to these new T networks in Fig. 4.7(a). (4.13)-(4.15) together with Fig. 4.7 (b) illustrate the calculations for the T to Π transformation. After this transformation, a schematic in Fig. 4.7 (c) is obtained. Choosing C_{r0} = 8.65pF, all the calculated and optimized element values are listed in Table 4.3. Fig. 4.8 (a) shows the simulated response for the circuit in Fig. 4.7 (c) before and after optimisation.

$$C_{j,j+1} = \frac{1}{\omega_0 K_{j,j+1}} \text{ for } j = 1 \text{ to } 3 \tag{4.10}$$

$$C_{01} = \frac{C_{r0} Z_0}{K_{01}} \sqrt{\frac{1}{1 + \omega_0{}^2 C_{r0}{}^2 Z_0{}^2}} \tag{4.11}$$

$$C_{s1} = \frac{C_{01}{}^2 (1 + \omega_0{}^2 C_{r0}{}^2 Z_0{}^2)}{C_{01} - C_{r0} + \omega_0{}^2 C_{r0}{}^2 C_{01} Z_0{}^2} \tag{4.12}$$

Again, by reviewing the schematic in Fig. 4.7 (c), it could be seen that all the shunt capacitors work as extra low pass elements. This is proved by comparing the response of the proposed schematic with that of an ideal 4th order Chebyshev bandpass filter in Fig. 4.8 (b). The proposed schematic shows excellent selectivity at the upper passband edge and the stopband attenuation is over 70 dB at 0.4 GHz, while the cost is slower than expected roll-off at the lower passband edge.

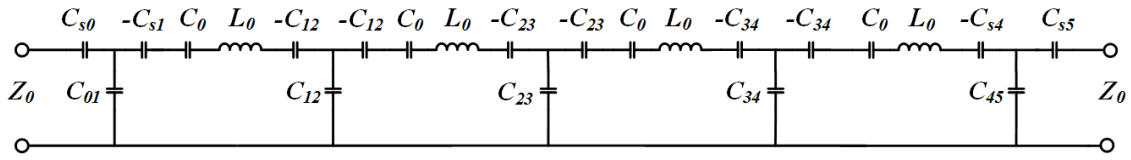

(a)

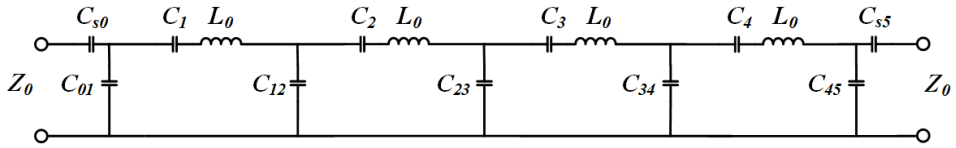

(b)

Fig. 4.6 A 4th order bandpass filter using series resonators and T-shape capacitive inverters

$$Z_a = \frac{Z_1Z_2 + Z_1Z_3 + Z_2Z_3}{Z_2} \tag{4.13}$$

$$Z_b = \frac{Z_1Z_2 + Z_1Z_3 + Z_2Z_3}{Z_1} \tag{4.14}$$

$$Z_c = \frac{Z_1Z_2 + Z_1Z_3 + Z_2Z_3}{Z_3} \tag{4.15}$$

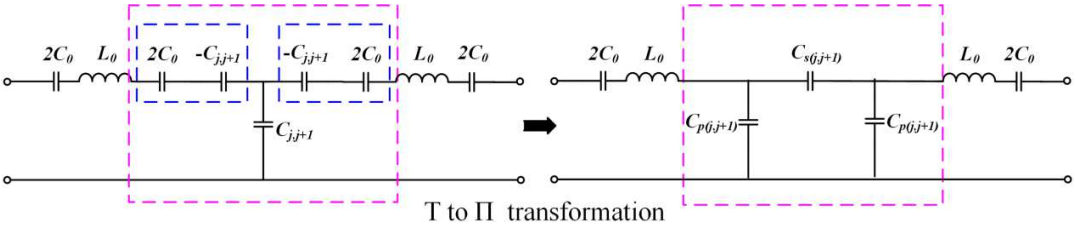

(a)

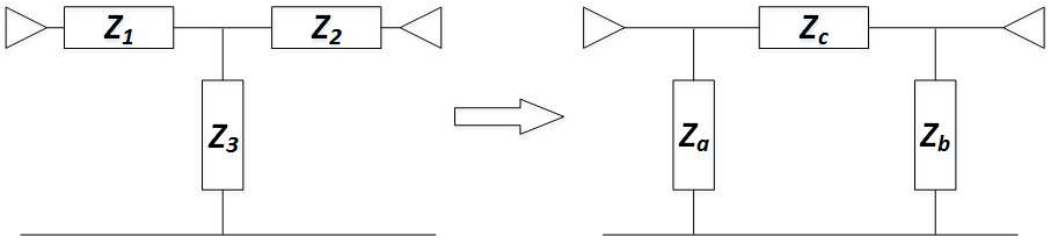

(b)

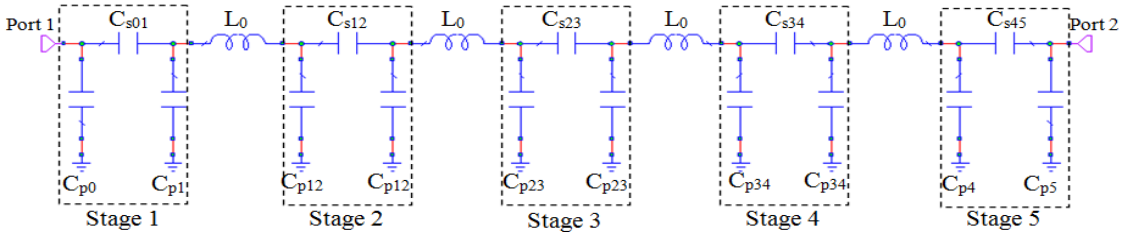

(c)

Fig. 4.7 (a) T to Π transformation (b) Equivalent block view (c) The final schematic for the proposed filter

	L0	**C_{s01} = C_{s45}**	**C_{s12} = C_{s34}**	**C_{s23}**	**C_{p0} = C_{p5}**	**C_{p1} = C_{p4}**	**C_{p12} = C_{p34}**	**C_{p23}**
Calculated	45nH	16.98pF	7.58pF	5.48pF	3.02pF	8.49pF	13.2pF	14.07pF
After optimization	42.8nH	16.05pF	7.47pF	5.33pF	3.50pF	9.33pF	14.13pF	14.46pF

Table 4.3 The element values of the 4-pole coupled-series-resonator filter with inductive inverters

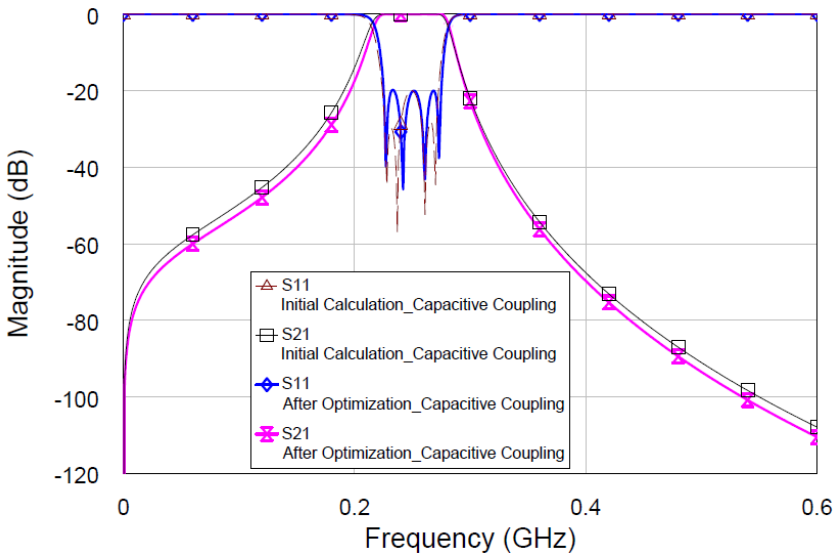

(a)

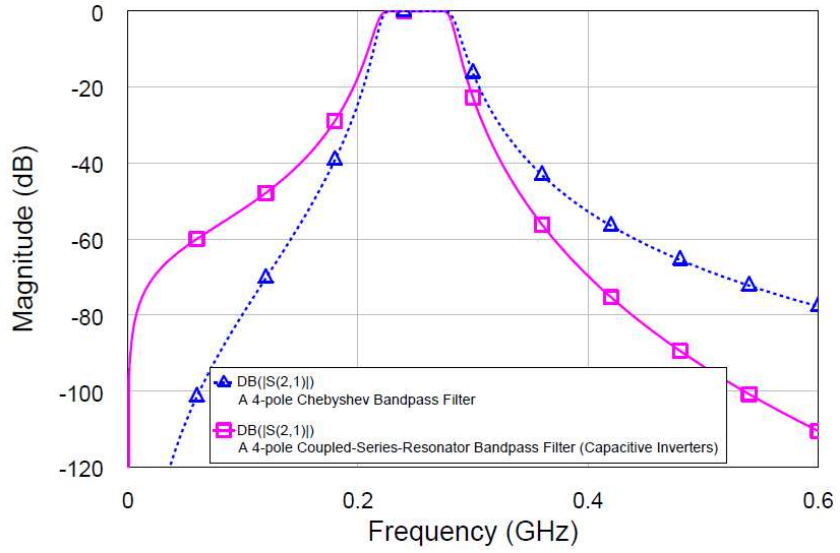

(b)

Fig. 4.8 A 4th order bandpass filter using series resonators and capacitive inverters. (a) Its simulation results before and after optimization (b) Its selectivity in comparison with a conventional 4-pole Chebyshev bandpass filter

4.3. A Short Comparison with Other Conventional Designs

It has been shown in Fig. 4.8(b) above that the proposed design shows better selectivity at upper passband edge than conventional 4th order Chebyshev bandpass filter design. Furthermore, as reflected by the g values in Table 4.1, 4th order and any other even order Chebyshev bandpass filters do not have a symmetric form. For instance, in Table 4.1, $g_0 \neq g_5$, indicating that the filter requires different input and output port impedances, which is

not convenient. However, as has been shown in Fig. 4.7 (c), the proposed filter has a very symmetric form, which can be an advantage in most applications, as no extra impedance matching network is needed.

To further highlight the advantages of this design, its performance is compared with a conventional 5-pole Chebyshev bandpass filter in Fig. 4.9. It can be seen that the proposed 4-pole filter has a much greater selectivity on the upper passband edge than the conventional 4-pole Chebyshev bandpass filter and is almost as good as the 5-pole one. When the frequency is above 500 MHz, it even gives greater stopband attenuation than a conventional 5-pole Chebyshev design. As a trade-off, the proposed design does not have as good selectivity as other filters for the lower passband edge. This indicates that in applications where upper passband edge selectivity and stopband attenuation is critical, the design in this chapter could be a very suitable candidate to replace higher order conventional bandpass filters. With less number of resonators, this design will bring the benefit of less insertion loss and smaller size.

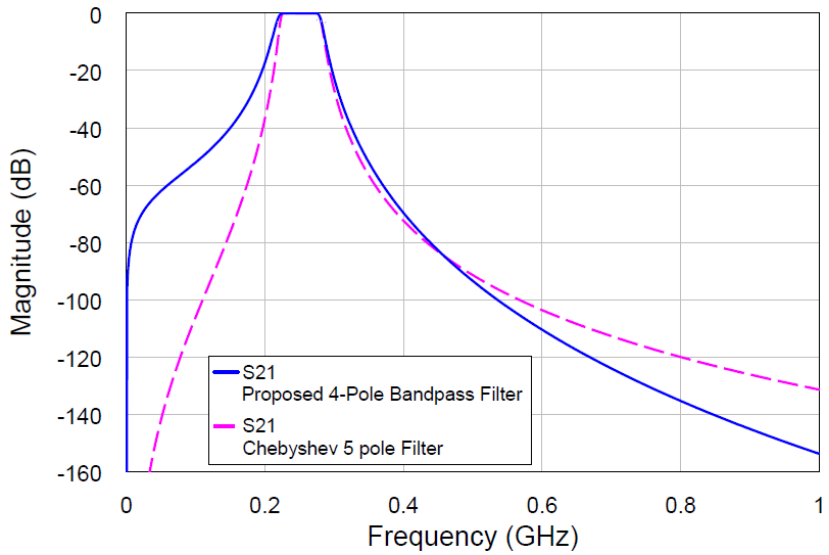

Fig. 4.9 A comparision between the proposed 4th order bandpass filter and a conventional 5th order Chebyshev bandpass filter

4.4. The LCP Implementation of the Proposed Design

Based on the circuit model in Fig. 4.7 (c), the multilayer LCP design shown in Fig. 4.10 (a) is produced as a compact implementation. The multilayer LCP structure has a total thickness of 0.4mm, with dielectric constant and loss tangent of 3 and 0.0025 respectively.

The structure consists of four copper layers for the circuit patterns and one for the ground as shown in Fig. 4.10 (b). The separation between every two adjacent circuit layers is 50 µm to provide a high capacitance density for the multilayer capacitors. The metal layers are made of copper and have a conductivity of 5.8×10^7 S/M.

Based on the element values extraction process as presented in [4.15], the multilayer LCP filter is designed and then optimised to obtain the required performance. The final dimensions of different stages of the design are detailed in Fig. 4.11 (a)-(c).

Fig. 4.12 (a) shows the full wave EM simulation [4.19] result of the lossless LCP structure in comparison with the circuit simulation [4.20] result of the circuit model. It can be seen that multilayer structure can produce an almost identical response to the ideal circuit model upto 0.5 GHz.

Since all of the multilayer elements that are being used in this design are low Q elements, the insertion loss of the proposed design can be an issue. Fig. 4.12 (b) shows the full wave EM simulation result of the candidate structure with conductor and dielectric loss. The passband return loss is around -20 dB, and the mid-band insertion loss is about -2.9 dB. For such a coupled-resonator circuit, the passband performance is mainly degraded by the loss of the resonators when a current is passing through them. For multilayer lumped elements on LCP, as discussed previously in Chapter 2, the Q of capacitors is around 300, while inductors using 0.1 -0.4mm line widths may only have a Q between 30 and 50. Thus it would be expected that by increasing the Q of the resonator inductors, the insertion loss of the filter can be largely improved. For this 4-pole filter, by increasing the Q of the resonator inductors to 200, the insertion loss can be decreased to -1.1 dB. The cost of this is larger inductor size and lower SRF, which would degrade the stopband performance. Fig. 4.12 (c) shows the wideband simulation result of the proposed filter and it can be seen that the design shows a very wide harmonic free stopband up to 2.34 GHz, which is 9.4 times the centre frequency. The out of band rejection is better than 70 dB between 0.4 GHz and 2.2 GHz.

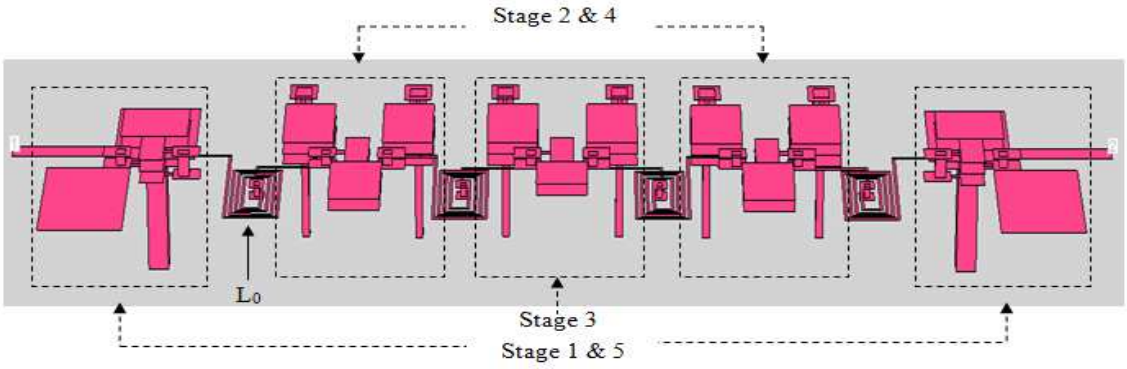

(a)

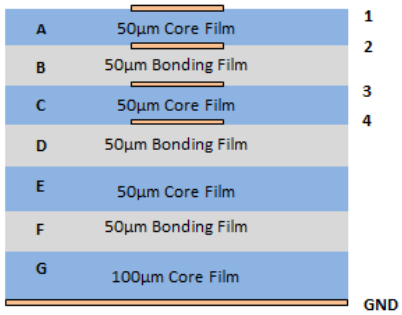

(b)

Fig. 4.10 (a) 3D structure of the proposed multilayer LCP bandpass filter and its (b) multilayer stack-up

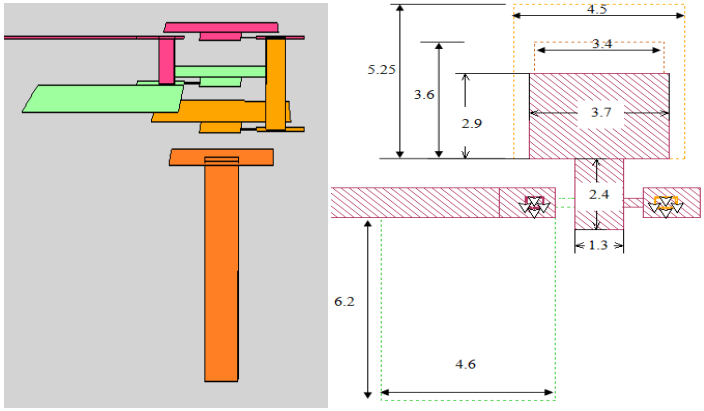

(a)

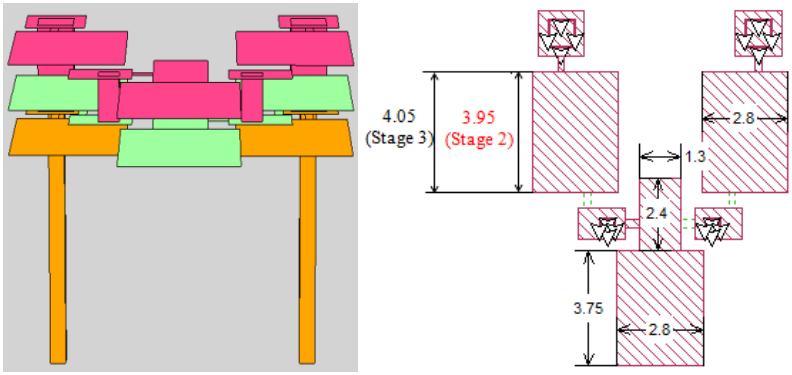

(b)

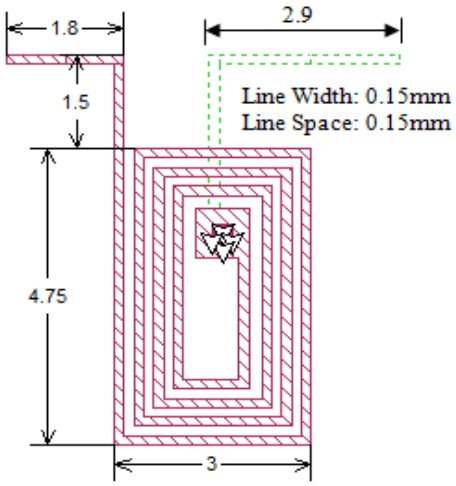

(c)

Fig. 4.11 3D structure and planar dimensions (unit: mm) for (a) stage 1 and (b) stage 2 and 3 (c) planar dimensions for the inductor L_0

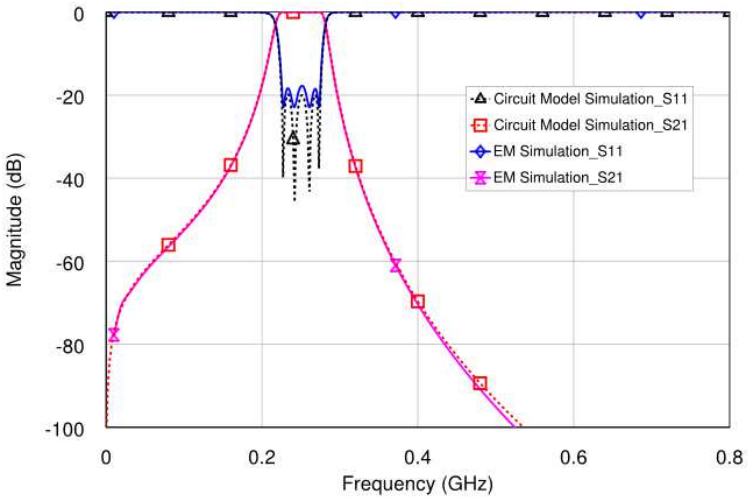

(a)

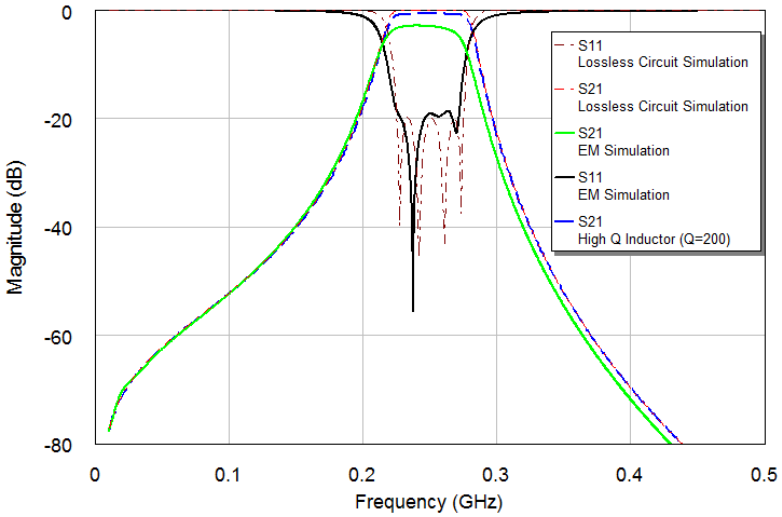

(b)

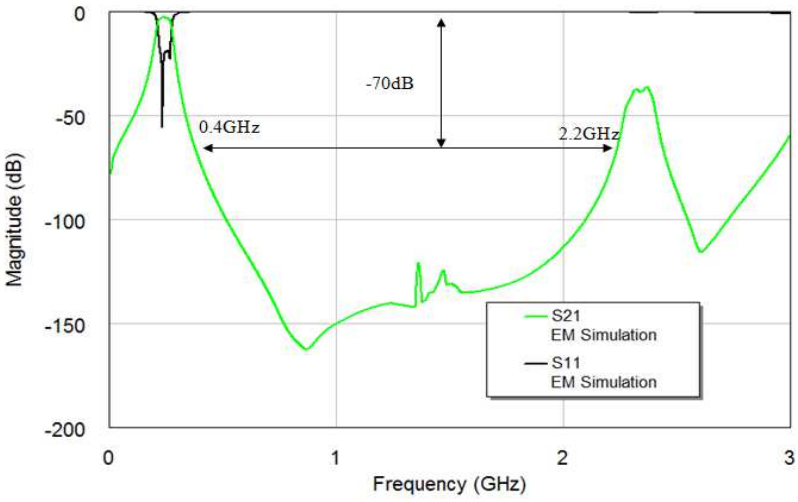

(c)

Fig. 4.12 (a) A comparision between the full wave simulation result and the circuit model simulation result (b) The insertion loss of the proposed LCP implementation (c) Wideband Performance

4.5. Fabrication and Measurement

A sample for the proposed design has been fabricated, as shown in Fig. 4.13 (a), using the manufacturing techniques developed in [4.15]. Excluding the 50 Ohm feed line, the filter has a size of 56.7 mm × 13.75 mm × 0.4 mm, which is only $0.074\lambda_g \times 0.018\lambda_g \times 0.00052\lambda_g$, where λ_g is the guided wavelength at the centre frequency of 250 MHz. The sample is measured on a HP8510B network analyzer with SMA connectors. The measured narrowband and wideband S-parameters are shown in Fig. 4.13 (b) and (c), respectively. The stopband performance is excellent and the S21 is down to -70 dB, which is already around the noise floor. The 2nd harmonic only appears at about 9.5 times the centre frequency and is below -36 dB. The measured best in-band insertion loss is -3.1 dB, which is only 0.2 dB higher than EM simulation. In general, the measurement is in a very good agreement with the EM simulation, apart from about 15 MHz frequency shifting, which is due to fabrication tolerance.

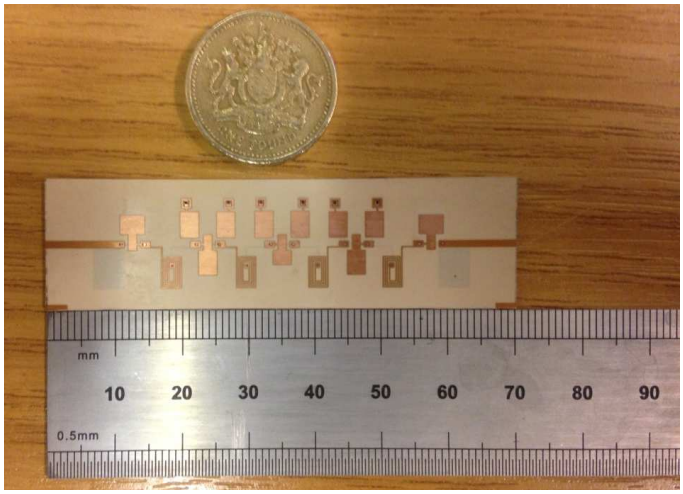

(a)

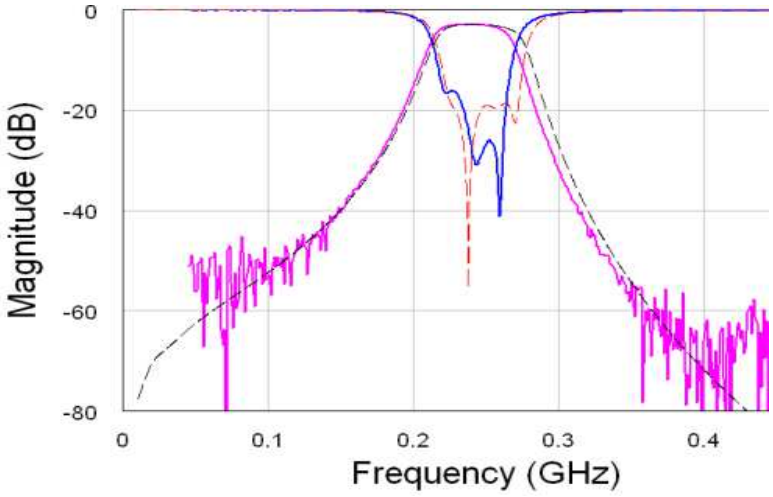

(b)

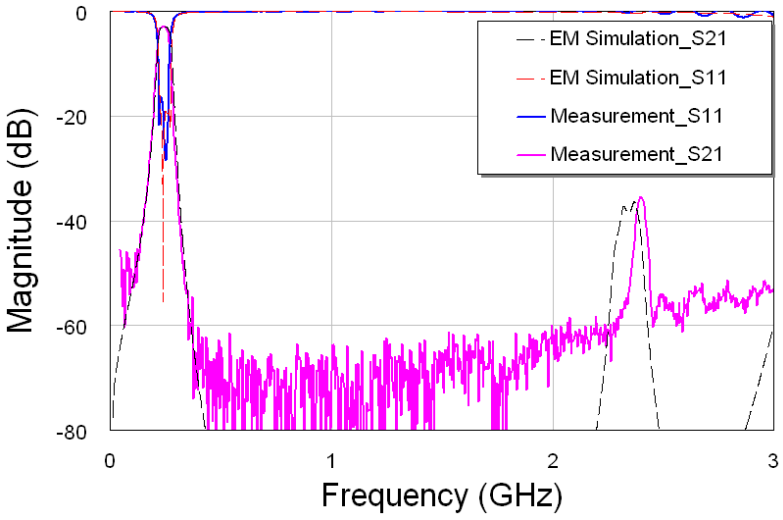

(c)

Fig. 4.13 (a) A photograph of the fabricated filter (b) Its measured narrow band performance (c) Wideband performance

4.6. Conclusion

In this chapter, a compact bandpass filter with moderate/narrow bandwidth using multilayer LCP technology has been designed and fabricated for the first time. Although based on the conventional coupled-resonator theory, this design explores the unusual combination of series resonators and T-shape capacitive inverters. T to Π transformations have been used during the design to make the circuit easy to implement on a multilayer substrate. A comparison between this design and other conventional designs has also been made and shows the superior upper stopband performance of the proposed design. This shows a promising future for the proposed design in practical RF/microwave applications.

The design has also been fabricated using multilayer LCP technology, which gives a very small foot print for the proposed design. The measured result of the fabricated sample agrees very well with the EM simulation result. From the work in this chapter, promising feedback about the possibility of using multilayer LCP technology for the design and fabrication of narrowband/moderate-band filters has been obtained. However, although the design in this chapter has excellent selectivity at the upper passband edge, it would be more desirable in some applications that finite frequency transmission zeroes can be generated near the passband. This will be investigated in the next chapter.

References

[4.1] S. B. Cohn, "Direct-Coupled-Resonator Filter," *IRE Tran. Microw. Theory Tech.*, vol. 45, no. 2, pp.187-196, Feb. 1957.

[4.2] E. H. Bradley, "Design and Development of Strip-line Filters," *IRE Tran. Microw. Theory Tech.*, vol. 4, no. 2, pp. 86-93, Apr. 1956.

[4.3] S. B. Cohn, "Parallel-Coupled Transmission-Line-Resonator Filters," *IRE Trans. Microw. Theory Tech.*, vol. 6, no. 2, pp. 223-231, Apr. 1958.

[4.4] G. L. Matthaei, "Interdigital Band-Pass Filters," *IRE Trans. Microw. Theory Tech.*, vol. 10, no. 6, pp. 479-491, Nov. 1962.

[4.5] R. M. Fano, and A. W. Lawson, "Microwave Filters Using Quarter-Wave Couplings," *IRE Trans. Microw. Theory Tech.*, vol. 35, no. 11, pp. 1318-1323, Nov. 1947.

[4.6] E. G. Cristal, and S. Frankel, “Design of Hairpin-Line and Hybrid Hairpin-Parallel-Coupled-Line Filters,” in *IEEE MTT-S Int. Microw. Symp. Dig.*, May 1971, pp.12-13.

[4.7] J. -S. Hong, and M. J. Lancaster, “Canonical microstrip filter using square open-loop resonators,” *Electron. Lett.*, vol. 31, no. 23, pp. 2020-2022, Nov. 1995.

[4.8] H.-Y. Chien, T. M. Shen, T.-Y. Huang, W. H. Wang, and R. B. Wu, “Miniaturized bandpass filters with double-folded substrate integrated waveguide resonators in LTCC,” *IEEE Trans. Microw. Theory Tech.*, vol. 57, no. 7, pp. 1774–1782, Jul. 2009.

[4.9] J. S. Hong, M. J. Lancaster, D. Jedamzik, and R. B. Greed, “On the development of superconducting microstrip filters for mobile communications applications,” *IEEE Trans. Microw. Theory Tech.*, vol. 47, no. 9, pp. 1656–1663, Sep. 1999.

[4.10] W. –C. Chien, C. –M. Lin, P. K. Singh, S. Basu, C.-H. Hsiao, G.-W. Huang, and Y.-H. Wang, “MMIC Compact Filters With Third Harmonic Suppression for V-Band Applications”, *IEEE Microw. Wireless Comp. Lett.*, vol. 21, no. 6, pp. 295 - 297, June 2011.

[4.11] L. Su and C. –K. Clive Tzuang, “A Narrowband CMOS Ring Resonator Dual-Mode Active Bandpass Filter With Edge Periphery of 2% Free-Space Wavelength,” *IEEE Trans. Microw. Theory Tech.*, vol. 60, no. 6, pp. 1605–1616, June 2012.

[4.12] G. Brzezina, L. Roy and L. MacEachern, “Design Enhancement of Miniature Lumped-Element LTCC Bandpass Filters,” *IEEE Trans. Microw. Theory Tech.*, vol. 57, no. 4, pp. 815–823, April 2009.

[4.13] M. Hoft and T. Shimamura, “Design of symmetric trisection filters for compact low-temperature co-fired ceramic realization,” *IEEE Trans. Microw. Theory Tech.*, vol. 58, no. 1, pp. 165-175, Jan. 2010.

[4.14] Z.-C. Hao and J.-S. Hong, “UWB Bandpass Filter Using Cascaded Miniature High-Pass and Low-Pass Filters With Multilayer Liquid Crystal Polymer Technology,” *IEEE Trans. Microw. Theory Tech.*, vol. 58, no. 4, pp. 941-948, Apr. 2010.

[4.15] S. Qian and J.-S. Hong, “Miniature Quasi-Lumped Element Wideband Bandpass Filter at 0.5-2 GHz Band Using Multilayer Liquid Crystal Polymer Technology,” *IEEE Trans. Microw. Theory Tech.*, vol.60, no. 9, pp.2799-2807, Sept. 2012.

[4.16] S. Mukherjee, B. Mutnury, S. Dalmia, and M. Swaminathan, “Layoutlevel synthesis of RF inductors and filters in LCP substrates for Wi-Fi applications,” *IEEE Trans. Microw. Theory Tech.*, vol. 58, no. 4, pp. 2196–2210, Apr. 2005.

[4.17] J.-S. Hong, *Microstrip Filters for RF/Microwave Applications*, 2nd Edition. New Jersey: Wiley, pp. 379-384, 2011.

[4.18] G. L. Matthaei, L. Young and E.M.T. Jones, *Microwave Filters, Impedance-matching Networks and Coupling Structures*, Artech House, 1980.

[4.19] Sonnet *em*, EM User’s Manual, Version 12, NY 2009.

[4.20] AWR Microwave Office, Appl. Wave Res. Inc., Version 2009, El Segundo, CA, 2007.

Chapter 5
Miniature Bandpass Filters with Transmission Zeroes using Mixed Couplings

5.1. Introduction

In Chapter 4, a compact coupled-resonator filter was designed and fabricated using multilayer LCP technology. Although the filter had superior stopband performance, it lacks finite frequency transmission zeroes near the passband. Since introducing such zeroes can significantly improve the selectivity of the filter, which was discussed in Chapter 2 and 3, it is desired that compact filters with narrow/moderate bandwidths can have cross couplings to generate transmission zeroes near the passband.

In open literature, various types of cross-coupled filters have been developed. These filters include the very popular cascaded trisection (CT) [5.1, 5.2] and cascaded quadruplet (CQ) filters [5.3, 5.4]. With the development of coupling matrix synthesis in [5.5]-[5.6], arbitrarily defined transmission zeroes can be produced. To produce the maximum number of transmission zeros for an N^{th} order filter, (N+2) × (N+2) coupling matrices are then introduced in [5.7] to include the source and load into the coupling diagram. This gives the fully canonical structure and N finite frequency transmission zeroes can be produced for an N-pole bandpass filter.

However, a filter implemented using a conventional coupling matrix may only produce the desired frequency response in a narrow bandwidth. This means although the passband return loss can be optimised to meet the specification, the selectivity, the whole shape of S21, and the stopband attenuation can be very different from the ideal coupling matrix prototype, which is a circuit model using ideal frequency-independent inverters. This problem is detailed below.

The procedure of designing a narrowband bandpass filter using a coupling matrix is shown in Fig. 5.1. With the coupling matrix, a circuit consisting of ideal series/parallel LC resonators and frequency-independent impedance/admittance inverters is formed as the starting point; this is referred to as coupling matrix prototype in this chapter. This circuit accurately produces the pre-defined arbitrary response and is called “Circuit 1” in Fig. 5.1.

Then the resonators and inverters in this coupling matrix prototype are replaced by practical microwave resonator models and frequency dependent inverters, respectively. This forms the “Circuit 2” in Fig. 5.1. It should be mentioned that, although “Circuit 2” in Fig. 5.1 has the form of lumped element, it actually could be in other forms, such as a filter model consists of half wavelength transmission lines and edge coupling models. Eventually this “Circuit 2” is translated to waveguide, coaxial line or microstrip structure in commercially available full wave EM simulation tools and is then the “Circuit 3” in Fig. 5.1.

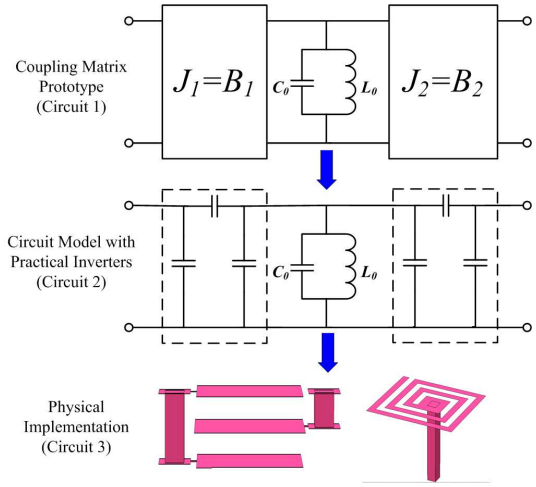

Fig. 5.1 The design flow of coupled resonator filters using multilayer lumped-elements

In the above design flow, “Circuit 1” should be the ultimate design target and all implementations should be aimed to match it. However, there is only a very narrowband match between “Circuit 1” and “Circuit 2”, which is due to the resonators and couplings that are used. Furthermore, in most cases, obtaining the match between “Circuit 2” and “Circuit 3” in this design flow is more emphasized in publications, while “Circuit 1” is only used for initial analysis and then ignored. Eventually, only a very narrowband agreement is obtained between “Circuit 1” and “Circuit 3”.

To produce a coupling matrix that can be used to design coupled-resonator bandpass filters with wideband response match between “Circuit 1” and “Circuit 2”, new approaches have been investigated in open literature. [5.8] starts by producing the transversal circuit, which can be then transformed to other topologies. The approach in [5.9] is developed by assuming all the main couplings are inductive or capacitive, and then the resultant coupling matrix can take into account the frequency-dependency of the impedance/admittance inverters. However, the transformation methods in [5.8] are complicated and it would be

more preferable that filter design can be carried out based on the general coupling matrix synthesis procedures as detailed in [5.5]-[5.7]. The method in [5.9] actually produces a different type of matrix from [5.5]-[5.7] as it only consists of capacitive couplings or inductive couplings. In Chapter 4, it was already proved that filters using such type of pure couplings will have very different frequency response from the original coupled-resonator filter prototype. In addition, none of these papers present physical implementations and measured responses of filters with finite-frequency transmission zeroes.

To tackle this issue, a novel systematic design approach will be discussed in this chapter. Section 5.2 will introduce a new type of similarity transformation, which can be used to change signs of couplings in a coupling matrix. Then it will be proved in Section 5.3 that, if a frequency-dependent capacitive coupling is combined with an inductive coupling, the frequency response will be very close to that of two ideal frequency-independent couplings. This type of mixed-coupling actually forms a bridge between ideal inverters and practical inverters, and it is the key of matching "Circuit 1" and "Circuit 2" in a wide bandwidth. By combining the conclusions from Section 5.2 and 5.3, it can be seen that by applying a set of similarity transformations to a coupling matrix, a more desired coupling matrix with equal number of inductive and capacitive couplings can be produced. Then this leads to a cross coupled lumped-element circuit with the best possible wideband response match with the original coupling matrix prototype. Section 5.4 then applies these theories to direct-coupled-resonator filters to show the differences between coupling matrix prototype and common filter implementations. To demonstrate the applications of these theories to the design of cross-coupled filters, a bandpass filter, based on an N×N coupling matrix, is designed and fabricated using multilayer LCP technology as an example in Section 5.5. Section 5.6 will then show how this approach can be applied to an (N+2) × (N+2) coupling matrix to produce maximum number of transmission zeroes for an N-pole bandpass filter. The general design procedure is summarised in Section 5.7. This is then followed by a conclusion for this chapter.

5.2. A Special Type of Similarity Transformation for Coupling Matrices

For coupled-resonator filter design, once the specification of a filter is given, a coupling matrix can be produced using the synthesis method presented in [5.5] and [5.6]. This matrix is then reduced to a simplified and easy-to-implement coupling matrix, such as the folded

configuration in Fig. 5.2 (a) and (b), or other forms such as the CUL-DE-SAC configuration in [5.10]. During this simplification, a type of matrix similarity transformation, called matrix rotation is used and it does not change the frequency response represented by the coupling matrix as proved in [5.10]. However, such rotation does not change the signs of the entries in a coupling matrix.

	1	2	3	4	5
1	m_{11}	m_{12}	0	0	m_{15}
2	.	m_{22}	m_{23}	m_{24}	m_{25}
3	.	.	m_{33}	m_{34}	0
4	.	.	.	m_{44}	m_{45}
5	.	.	.	.	m_{55}

(a)

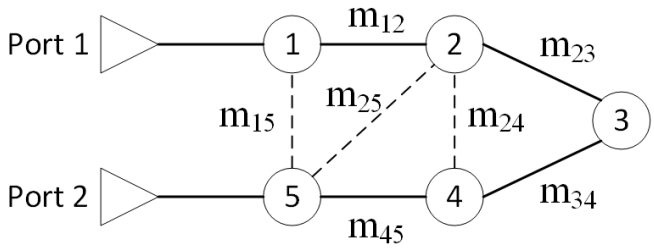

(b)

Fig. 5.2 (a) A simplified coupling matrix for a 5th order bandpass filter and (b) its coupling diagram

$$\mathbf{M_r} = \mathbf{T_k} \cdot \mathbf{M_{r-1}} \cdot \mathbf{T_k^{-1}} \tag{5.1}$$

In general, the similarity transformation for a coupling matrix $\mathbf{M_{r-1}}$ has the form of (5.1), where $\mathbf{T_k}$ is an orthogonal matrix and $\mathbf{M_r}$ the new coupling matrix. To change the signs of non-diagonal elements in $\mathbf{M_{r-1}}$, a special type of orthogonal matrix is used and shown in Fig.5.3.

	1	2	…	k	…	N-1	N
1	1	0	0	0	0	0	0
2	0	1	0	0	0	0	0
⋮	0	0	1	0	0	0	0
k	0	0	0	**-1**	0	0	0
⋮	0	0	0	0	1	0	0
N-1	0	0	0	0	0	1	0
N	0	0	0	0	0	0	1

Fig. 5.3 A special orthogonal matrix $\mathbf{T_k}$

It can be seen that $\mathbf{T_k}$ is almost the same as the identity matrix **I** except that the element m_{kk} is -1. The inversed matrix $\mathbf{T_k}^{-1} = \mathbf{T_k}$. When such a similarity transformation is applied to the coupling matrix $\mathbf{M_{r-1}}$, elements in row *k*, m'_{ki}, and column k, m'_{ik}, of the new matrix $\mathbf{M_r}$ are changed according to (5.2)-(5.4).

$$m'_{ki} = -m_{ki}, i \neq k \tag{5.2}$$

$$m'_{ik} = -m_{ik}, i \neq k \tag{5.3}$$

$$m'_{kk} = m_{kk} \tag{5.4}$$

It should be mentioned that, unlike the similarity transformation in [5.10], the special orthogonal matrix $\mathbf{T_k}$ being used here is not a rotation matrix, thus this similarity transformation is not a matrix rotation process, but it can be called a matrix reflection [5.11]. It can be seen that after such a similarity transformation with the special orthogonal matrix $\mathbf{T_k}$, signs of all elements in row k and column k are changed except that, the diagonal element m_{kk} , which represents the frequency offset of the resonator k, is not affected. If a coupling diagram is used, such a similarity transformation changes the signs of couplings associated with the resonator k. Fig. 5.5 shows the new coupling diagram after applying such a similarity transformation on the coupling diagram in Fig. 5.2 (b) with a transformation matrix $\mathbf{T_2}$ in Fig. 5.4.

	1	2	3	4	5
1	1	0	0	0	0
2	0	-1	0	0	0
3	0	0	1	0	0
4	0	0	0	1	0
5	0	0	0	0	1

Fig. 5.4 An orthogonal matrix T_2

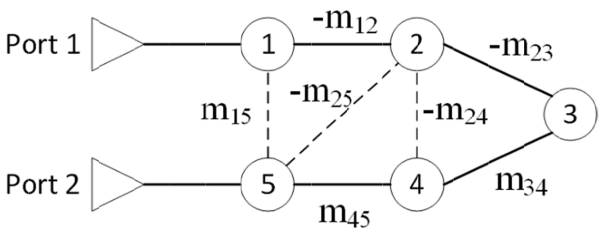

Fig. 5.5 New coupling diagram after applying T_2 to the diagram in Fig 5.2. (b)

5.3. Non-ideal Inverters

The theory of coupled-resonator filter is usually used to design narrowband filter as have been mentioned in Chapter 4. This is because practical microwave resonators and impedance/admittance inverters have the required performances only within a very limited bandwidth. In a coupled-distributed-resonator filter, both the resonators and couplings are based on narrowband assumptions. In a coupled-lumped-resonator filter, although the lumped element resonators behave like ideal lumped-element resonators over a much wider bandwidth than distributed resonators, lumped-element T or π inverters in Fig. 5.6 are frequency-dependent. Although they have frequency-invariant phase shift, their characteristic impedances depend on the frequency, as shown by (5.5) and (5.6) [5.12]. In this case, to design a coupled-lumped-resonator filter with wideband matching with the coupling matrix prototype, the non-ideal effect from the lumped element inverters should be minimized.

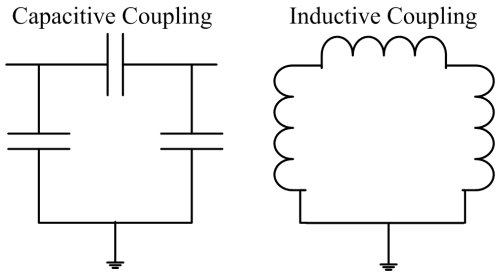

Fig. 5.6 Lumped element admittance inverters

$$|J| = \omega C \tag{5.5}$$

$$|J| = \frac{1}{\omega L} \tag{5.6}$$

Considering the two port network as shown in Fig. 5.7, two admittance inverters are separated by a shunt parallel resonator. The *S21* of such a network is represented by (5.7), which is obtained from network analysis. In an ideal case, the two inverters have frequency-independent values B_1 and B_2, respectively. Then by substituting (5.8), which represents the resonator's frequency response, into (5.7), (5.9) can be obtained. It can be seen that the only frequency dependency of the *S21* for such a network come from $Y_R(\omega)$, which is the impedance of the resonator.

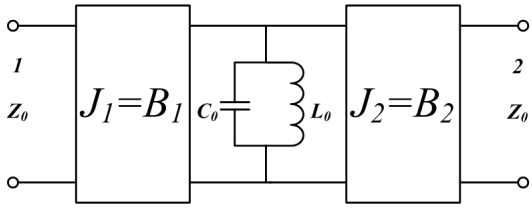

Fig. 5.7 A two port network consisting of two admittance inverters and a resonator

$$|S_{21}(\omega)| = \left| \frac{-2}{\frac{J_2}{J_1} + \frac{j(\omega C_0 - \frac{1}{\omega L_0})}{Z_0} \cdot \frac{1}{J_1 J_2} + \frac{J_1}{J_2}} \right| \tag{5.7}$$

$$Y_R(\omega) = j(\omega C_0 - \frac{1}{\omega L_0}) \tag{5.8}$$

$$|S_{21}(\omega)| = \left| \frac{-2}{\frac{B_2}{B_1} + \frac{Y_R(\omega)}{Z_0} \cdot \frac{1}{B_1 B_2} + \frac{B_1}{B_2}} \right| \tag{5.9}$$

However, there is no such frequency-independent inverter in reality. By replacing J_1 and J_2 with the capacitive or inductive inverters from Fig. 5.7, four different combinations can be obtained as listed in Table 5.1, where the values of C_1, C_2, L_1 and L_2 are listed in Table 5.2.

Combination	J_1	J_2
1	$J_1 = \omega C_1$	$J_2 = \omega C_2$
2	$J_1 = \frac{-1}{\omega L_1}$	$J_2 = \frac{-1}{\omega L_2}$
3	$J_1 = \omega C_1$	$J_2 = \frac{-1}{\omega L_2}$
4	$J_1 = \frac{-1}{\omega L_1}$	$J_2 = \omega C_2$

Table 5.1 Different combinations of inverters

C_1	C_2	L_1	L_2
$\frac{B_1}{\omega_0}$	$\frac{B_2}{\omega_0}$	$\frac{-1}{\omega_0 B_1}$	$\frac{-1}{\omega_0 B_2}$

Table 5.2 The values of coupling elements

Since 3 and 4 in Table 5.1 actually give the same kind of frequency dependency, only combinations 1, 2 and 3 are substituted into (5.7), and then (5.10), (5.11) and (5.12) are obtained respectively.

$$|S_{21}(\omega)| = \left|\frac{-2}{\frac{C_2}{C_1} + \frac{Y_R(\omega)}{Z_0} \cdot \frac{1}{\omega^2 C_1 C_2} + \frac{C_1}{C_2}}\right| = \left|\frac{-2}{\frac{B_2}{B_1} + \frac{Y_R(\omega)}{Z_0} \cdot \frac{{\omega_0}^2}{\omega^2} \cdot \frac{1}{B_1 B_2} + \frac{B_1}{B_2}}\right| \tag{5.10}$$

$$|S_{21}(\omega)| = \left|\frac{-2}{\frac{L_1}{L_2} + \frac{Y_R(\omega)}{Z_0} \cdot \omega^2 L_1 L_2 + \frac{L_2}{L_1}}\right| = \left|\frac{-2}{\frac{B_2}{B_1} + \frac{Y_R(\omega)}{Z_0} \cdot \frac{\omega^2}{{\omega_0}^2} \cdot \frac{1}{B_1 B_2} + \frac{B_1}{B_2}}\right| \tag{5.11}$$

$$\begin{aligned} |S_{21}(\omega)| &= \left|\frac{-2}{\frac{-1}{\omega^2 C_1 L_2} + \frac{Y_R(\omega)}{Z_0} \cdot \frac{-L_2}{C_1} + (-\omega^2 C_1 L_2)}\right| \\ &= \left|\frac{-2}{\frac{B_2}{B_1} \cdot \frac{{\omega_0}^2}{\omega^2} + \frac{Y_R(\omega)}{Z_0} \cdot \frac{1}{B_1 B_2} + \frac{B_1}{B_2} \cdot \frac{\omega^2}{{\omega_0}^2}}\right| \end{aligned} \tag{5.12}$$

It can be seen that $Y_R(\omega_0)$ is zero at the resonant frequency ω_0. Thus (5.10)-(5.12) are all identical to (5.9) no matter what values B_1 and B_2 are. For an input and output matched case, B_1 is equal to B_2, and then $|S_{21}|$ is 1 at the resonant frequency ω_0. So for a narrow band analysis, all of the above cases give similar frequency response.

However, if a wideband analysis is carried out, the result is very different. As frequency moves away from ω_0, it can be seen that the middle term of the denominator of (5.9), $\frac{Y_R(\omega)}{Z_0} \cdot \frac{1}{B_1 B_2}$, gets bigger and bigger, while $\frac{B_2}{B_1}$ and $\frac{B_1}{B_2}$ have values between 0.5 and 2. Thus for this wideband analysis, (5.9) – (5.12) can be simplified to (5. 13) – (5.16), respectively. So far only two constants $\frac{B_2}{B_1}$ and $\frac{B_1}{B_2}$ have been ignored, and they are much smaller than $\frac{Y_R(\omega)}{Z_0} \cdot \frac{1}{B_1 B_2}$. This means the error caused by the above simplification is negligible. Furthermore, the above simplification does not change the frequency dependency of (5.9) – (5.12) and this will ensure that (5.13) – (5.16) can be confidently used for the wideband analysis. It can be seen that (5.16) has the best match with (5.9), and its frequency response only depends on $Y_R(\omega)$, while (5.14) and (5.15) have extra dependencies and exhibit highpass and lowpass properties, respectively. Fig. 5.8 plots the $|S21|$ of (5.9)-(5.12) against normalized frequencies.

$$|S_{21}(\omega)| \approx \left| \frac{-2}{\frac{Y_R(\omega)}{Z_0} \cdot \frac{1}{B_1 B_2}} \right| \tag{5.13}$$

$$|S_{21}(\omega)| \approx \left| \frac{-2}{\frac{Y_R(\omega)}{Z_0} \cdot \frac{1}{\omega^2 C_1 C_2}} \right| \tag{5.14}$$

$$|S_{21}(\omega)| \approx \left| \frac{-2}{\frac{Y_R(\omega)}{Z_0} \cdot \omega^2 L_1 L_2} \right| \tag{5.15}$$

$$|S_{21}(\omega)| \approx \left| \frac{-2}{\frac{Y_R(\omega)}{Z_0} \cdot \frac{-L_2}{C_1}} \right| = \left| \frac{-2}{\frac{Y_R(\omega)}{Z_0} \cdot \frac{1}{B_1 B_2}} \right| \tag{5.16}$$

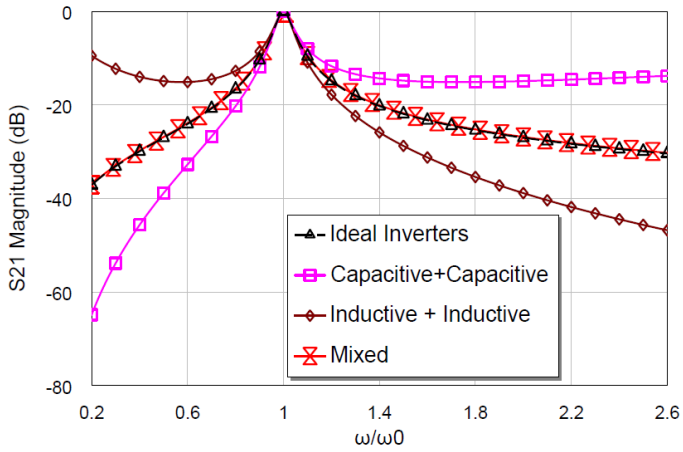

Fig. 5.8 |S21| of different combinations of inverters

It can be seen from Fig. 5.8 that by combining an inductive coupling with a capacitive coupling, the frequency response is almost identical to the combinations of two ideal frequency-independent inverters over a wide bandwidths. This then forms the basis of using mixed frequency-dependent couplings to design filters with a wideband match with coupling matrix prototypes. It also implies that when a direct-coupled-resonator filter is designed, if purely inductive/capacitive couplings are used, the implemented filter will then have a very different wideband response from the coupling matrix prototype using ideal inverters. This is illustrated in the next section.

5.4. Direct Coupled Resonator Filters with Wideband Response Matching with Coupling Matrix Prototype

Fig. 5.9 (a) shows a normalized N × N coupling matrix for a 5-pole direct-coupled resonator filter with a centre frequency of 0.25 GHz, fractional bandwidth (FBW) of 20%, and passband ripple of 0.043 dB. Then by applying the de-normalization in (5.17) [5.12], the coupling matrix for a *FBW* of 20% is obtained in Fig. 5.9 (b). All of the 4 couplings between any two adjacent resonators are positive and implemented as capacitive couplings. By using the similarity transformation in Section 5.2, this coupling matrix can be reconfigured to have zero to four negative couplings. For instance, by using a transformation matrix $\mathbf{T_2}$, couplings M_{12} and M_{23} can be changed to negative. Then by using another matrix $\mathbf{T_1}$, M_{12} is changed back to positive, leaving only M_{23} negative.

$$M_{j,j+1} = m_{j,j+1} \cdot FBW \tag{5.17}$$

	1	2	3	4	5
1	0	m_{12}=0.8655	0	0	0
2	.	0	m_{23}=0.6355	0	0
3	.	.	0	m_{34}=0.6355	0
4	.	.	.	0	m_{45}=0.8655
5	.	.	.	.	0

(a)

	1	2	3	4	5
1	0	M_{12}=0.1731	0	0	0
2	.	0	M_{23}=0.1271	0	0
3	.	.	0	M_{34}=0.1271	0
4	.	.	.	0	M_{45}=0.1731
5	.	.	.	.	0

(b)

Fig. 5.9 A coupling matrix for a fifth order direct-coupled-resonator filter (a) normalized (b) de-normalized

So depending on the number of negative couplings, five different coupling combinations can be obtained. Although with ideal inverters, all of these reconfigured coupling matrix prototypes produce the same response. However, after replacing the ideal inverters with lumped-element capacitive/inductive inverters from Fig. 5.6, these filters produce very different wideband response, as shown in Fig. 5.10 (a) and (b). Some of them have better selectivity at the lower passband edges, while others at the higher edges. As indicated in Section 5.3, it can be expected that if two of the coupling are implemented as inductive inverters while the other two capacitive, the |S21| of the filter may have almost identical response with the filter using ideal inverters. This is verified in Fig. 5.10 (a), as the response of the filter with two capacitive couplings overlaps the ideal coupling matrix prototype. From another point of view, by using different couplings, the reflection zeros are produced at different frequencies, as shown in Fig. 5.10 (b). These different distributions of reflection zeros lead to different selectivity at passband edges.

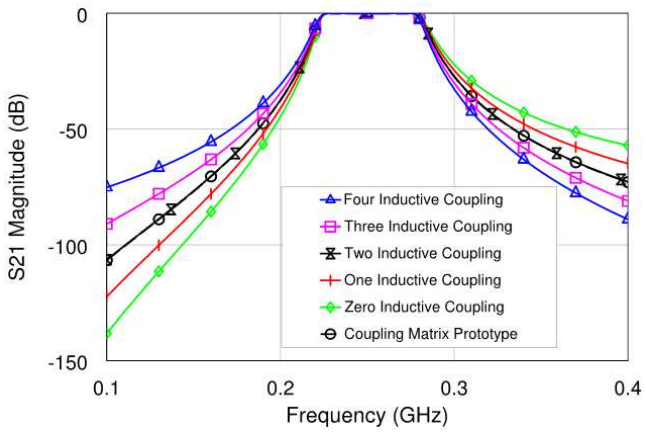

(a)

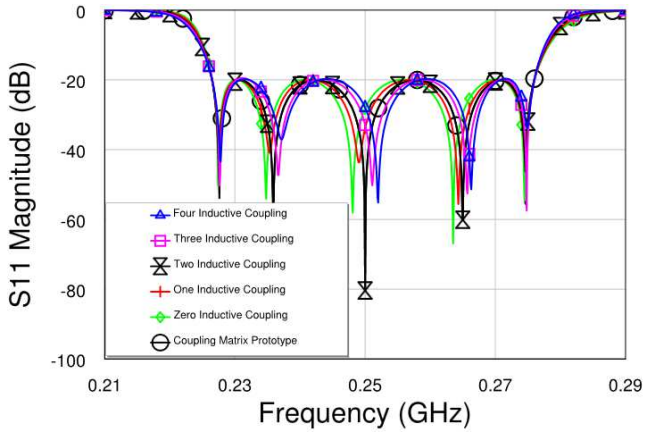

(b)

Fig. 5.10 (a) S21 and (b) S11 for different coupling configurations

It can also be seen that if all the couplings are implemented as capacitive inverters, these capacitive inverters together with the shunt resonators give the filter a very strong highpass nature, similar to (5.14), thus a high selectivity can be obtained at the lower passband edge. If all the inverters are inductive, then the filter has a very strong lowpass nature, similar to (5.15), which gives the filter a very good selectivity on the upper passband edge. It should be mentioned that if the resonators are implemented in a series way, then capacitive impedance inverters will give the filter a lowpass nature while inductive gives highpass, as have been discussed in Chapter 4.

5.5. A Five-pole Coupled Resonator Filter with Two Finite Frequency Transmission zeroes.

In this section, theories presented in Section 5.2 and 5.3 will be used to design a fifth order coupled-resonator filter with two finite frequency transmission zeroes. This is demonstrated with an N × N coupling matrix. The filter has a centre frequency of f_0 = 250 MHz and FBW = 20%. The passband ripple is 0.043 dB and two transmission zeroes are located at 215 MHz and 290 MHz, which correspond to -1.5 and 1.5, respectively, in the lowpass domain according to the bandpass to lowpass transformation [5.13]. Fig.5.11 (a) shows the normalized coupling matrix obtained by using the synthesis and matrix reduction method in [5.10]. Some online tools, such as in [5.14] could also be used for producing such a coupling matrix. Then by applying the de-normalization (5.17), the coupling matrix for a *FBW* of 20% is obtained in Fig. 5.11 (b). The external coupling coefficient $Q_{e01} = Q_{e56} = 4.971$.

	1	2	3	4	5
1	0	-0.8445	0	0	0
2	.	0	-0.5825	0	0.2136
3	.	.	0	0.7544	0
4	.	.	.	0	0.8170
5	.	.	.	.	0

(a)

	1	2	3	4	5
1	0	-0.1689	0	0	0
2	.	0	-0.1165	0	0.04272
3	.	.	0	0.1509	0
4	.	.	.	0	0.1634
5	.	.	.	.	0

(b)

Fig. 5.11 The original N×N coupling matrix (a) normalized (b) de-normalized

5.5.1. Synthesis

It can be seen that the matrix in Fig. 5.11 (b) already has an equal number of inductive and capacitive couplings. However, to further demonstrate the theory from Section 5.2 and 5.3,

and illustrate the differences of *S21* among different configurations, this matrix can be transformed to have purely capacitive main couplings and one inductive cross coupling by applying a transformation matrix $\mathbf{T_2}$, or purely inductive main couplings and one capacitive cross coupling by applying $\mathbf{T_4}$. When frequency-independent inverters are used, all of these three configurations give the same frequency response. By replacing these ideal inverters with practical inverters from Fig. 5.6 and perform some schematic optimizations [5.20] to obtain the required passband ripple, the *S21* and *S11* of these different configurations are plotted in Fig. 5.12 (a) and (b), respectively. It can be seen that the circuit model with equal number of inductive and capacitive main couplings has the best frequency response match with the coupling matrix prototype (they are overlapping each other in Fig. 5.12 (a) and (b)). It should be mentioned that, although the two configurations with purely capacitive or inductive couplings could be optimised to move the transmission zeroes to the correct positions, it then wouldn't be able to give the same passband ripple or bandwidth. The overall shape of the S21 wouldn't be the same as the coupling matrix prototype, either. This is basically because the positions of the passband poles determine the shape of the S21. It also shows that although there is an extra cross coupling for the matrix in Fig. 5.11, it does not have obvious effect on the shape of S21. This is because the positions of the passband poles, in Fig. 5.12 (a) are more determined by resonators and main couplings, while the cross coupling has more effect on the locations of transmission zeroes.

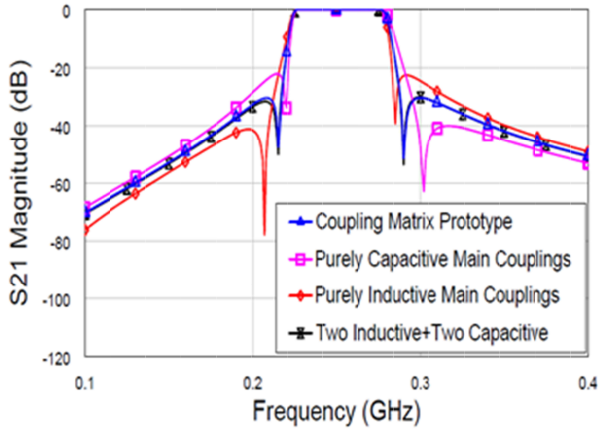

(a)

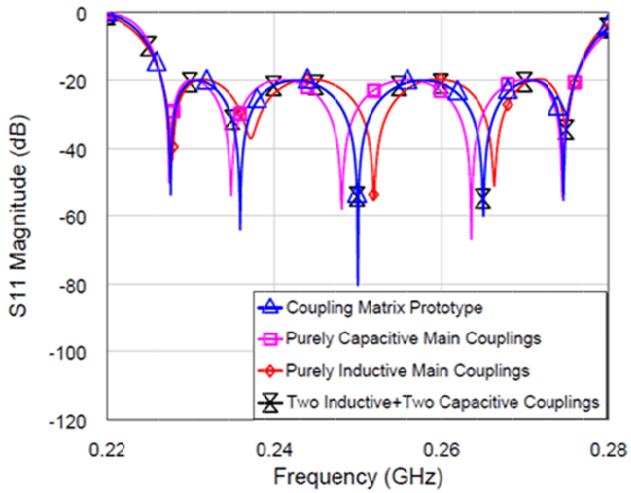

(b)

Fig. 5.12 (a) S21 and (b) S11 of different configurations

Up to this point, although it has been found that mixed couplings should be used to obtain a good agreement between practical LC circuit models and coupling matrix prototype, it is still difficult to implement the LC circuit on commercially available substrates due to the inductive couplings. The value of coupling inductors can be calculated using (5.18), where b_j and b_{j+1} are slope parameters [5.12]. Considering the de-normalization (5.17), for a small *FBW*, the value of $M_{j,j+1}$ is small and thus coupling inductors are of large values according to (5.18). For the matrix in Fig. 5.11 (b) and centre frequency of 250MHz, the $L_{j,j+1}$ is between 88nH and 129nH. To implement such large values, two methods could be used. One is reducing the width of the metal track and this would reduce the Q of the inductor.

Another way is to increase the length of the track with the cost of decreasing the self-resonant frequency (SRF). None of the above two methods is desired.

$$\frac{-1}{\omega L_{j,j+1}} = J_{j,j+1} = M_{j,j+1} \cdot \sqrt{b_j \cdot b_{j+1}} \tag{5.18}$$

To solve this problem, the negative inductance $-L_{j,j+1}$ from the inductive inverter is firstly combined with adjacent resonator inductors, then a Π to T transformation is applied to the circuit. All of the resultant series inductors L_{si}, $L_{s(i+1)}$ and shunt inductor $L_{p(i,\ i+1)}$ have realisable values. This Π to T transformation is valid for the whole frequency range and does not change the response of the circuit model. This process is shown in Fig. 5.13 (a) and (b).

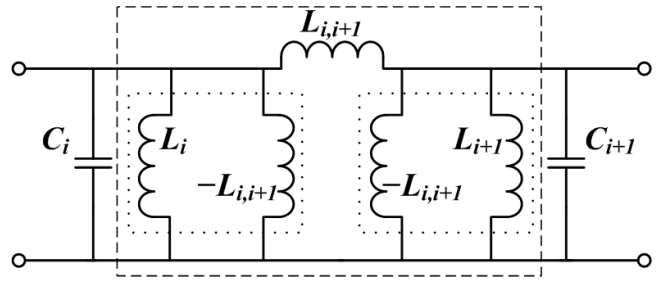

(a)

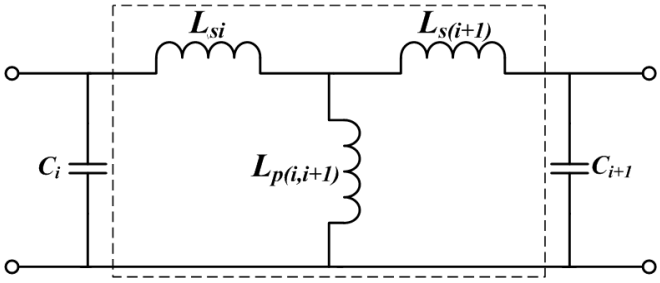

(b)

Fig. 5.13 (a) Before and (b) after Π to T transformation

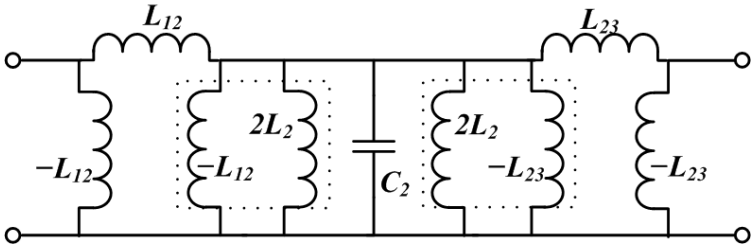

Fig. 5.14 Circuit with two inductive couplings adjacent to each other

In Fig. 5.11 (b), since two inductive couplings M_{12} and M_{23} are adjacent to each other, to absorb the negative inductances from inverters J_{12} and J_{23}, the resonator inductor L_2 has to be split to two inductors and then Π to T transformations can be applied at both sides, as illustrated in Fig. 5.14. Then this would introduce an extra element in the circuit, which is not desired from the miniaturisation perspective. To produce an optimal circuit model with the least number of elements for a miniature implementation, some further similarity transformations, as explained in Section 5.2, should be done to separate the two inductive couplings. The matrix in Fig. 5.15 can be obtained and chosen for the final implementation.

	1	2	3	4	5
1	0	-0.1689	0	0	0
2	.	0	0.1165	0	0.04272
3	.	.	0	0.1509	0
4	.	.	.	0	-0.1634
5	.	.	.	.	0

Fig. 5.15 The final coupling matrix after separating two adjacent inductive couplings

The corresponding final circuit model is shown in Fig. 5.16 after absorbing all the negative elements and applying Π to T transformations to inductive couplings. The input/output matching is done by using an L-shape matching section [5.12], other than a Π section to reduce the number of elements. It should be noticed that after the absorbing process, C_n is no longer the original resonator capacitor as they absorbed adjacent negative capacitance from the inverters or L-matching sections. An optimization of values of the circuit is then carried out to ultimately match the response of the coupling matrix. The values of circuit elements before and after optimisation are listed in Table 5.3. It should be clarified that by using such a mixed coupling approach, it does not mean that no optimisation is needed at the circuit model level. For other coupling configurations, an ultimate match could not be possible even with optimisations as already shown in Fig. 5.12 (a) and (b). So this mixed-coupling approach differs from others by the fact that it provides the possibility to almost fully match the response set by the coupling matrix. Fig. 5.17 shows the simulated responses of the circuit model in Fig. 5.16 and the ideal coupling matrix prototype. It could be seen that the circuit model in Fig. 5.16 which is generated from a coupling matrix using mixed couplings, has almost the same response as the ideal coupling matrix prototype. The locations of reflection and transmission zeroes are almost the same. Considering the

bandwidth of 75 MHz between the two transmission zeroes, the circuit model in Fig. 5.17 actually matches an ideal coupling matrix prototype over a *FBW* of 30%. Up to this point, a good agreement between "Circuit 1" and "Circuit 2" from Fig. 5.1 has been obtained.

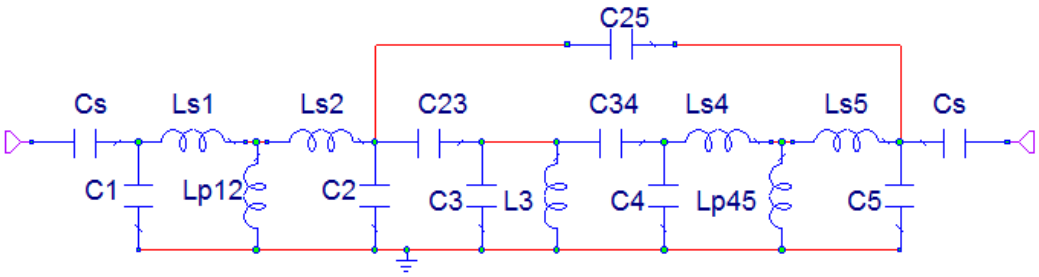

Fig. 5.16 The circuit model for physical implementation

	C1	C2	C3	C4	C5	C23	C34	Cs
Calculated	20.721pF	22.717pF	19.795pF	22.942pF	19.567pF	3.148pF	4.077pF	10.989pF
After optimization	19.61pF	22.29pF	20.96pF	22.30pF	18.67pF	3.104pF	4.016pF	9.937pF
	Ls1	Ls2	L3	Ls4	Ls5	Lp12	Lp45	C25
Calculated	12.833nH	12.833nH	15nH	12.893nH	12.893nH	2.608nH	2.518nH	1.154pF
After optimization	13.061nH	13.061nH	15nH	13.09nH	13.09nH	2.494nH	2.42nH	1.076pF

Table 5.3 Element values before and after optimization for the circuit in Fig. 5.17

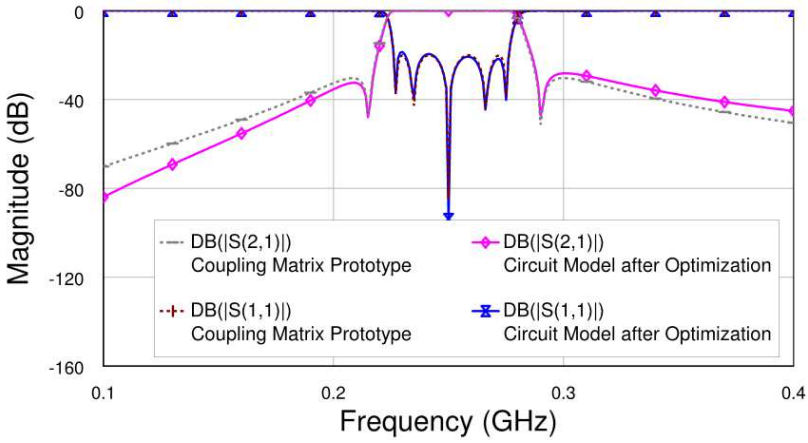

Fig. 5.17 Circuit simulation response versus coupling matrix prototype response

5.5.2. Implementation and Fabrication

The circuit in Fig. 5.16 is then implemented as a compact LCP module consisting of three circuit and one ground layers as shown in Fig. 5.18. The dielectric constant of LCP is 3.0 and loss tangent 0.0025. The thickness of the whole module is 0.4mm while separations between every two adjacent circuit layers are 50 µm.

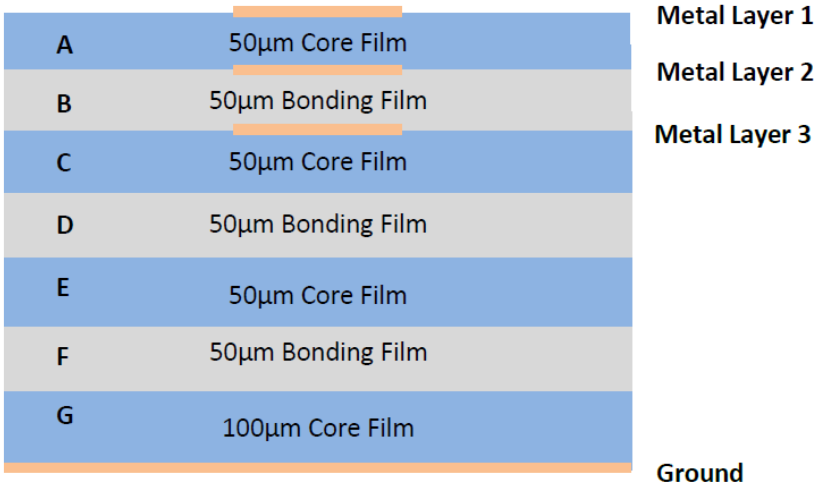

Fig. 5.18 Multilayer LCP structure for the implementation

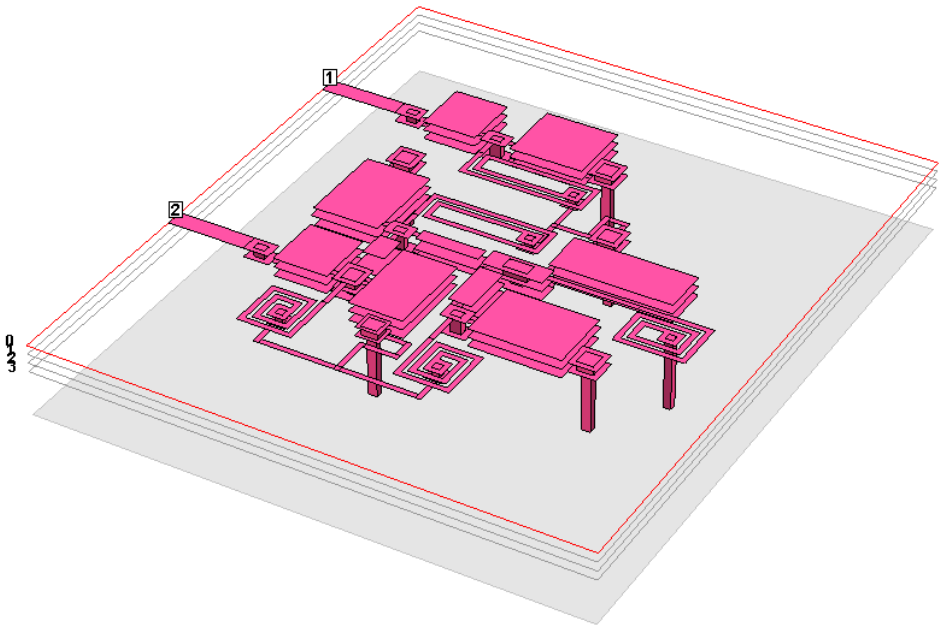

Fig. 5.19 3-D structure of the proposed filter

Then all of the capacitors and inductors are implemented on this multilayer structure and the filter is shown in Fig. 5.19. The initial physical dimensions of each inductor and

capacitor are obtained by using the element value extraction process from Chapter 2, then a tuning/optimisation process can be carried out to obtain a good match with the circuit model. The dimensions of the filter are $0.0294\lambda_g \times 0.0303\lambda_g \times 0.00052\lambda_g$ (22.6 mm × 23.25 mm × 0.4 mm), where λ_g is the guided wavelength at the centre frequency of 250 MHz. In terms of guided wavelengths, this is relatively small compared with other published multilayer filters [5.15]-[5.18]. Its final full wave simulation result [5.19] is compared with the circuit model simulation result [5.20] and is shown in Fig. 5.20 (a). It can be seen that the circuit model in Fig. 5.16 and the multilayer LCP module in Fig. 5.19 produce almost identical response from 0.1GHz to 0.4GHz. This then produces a match between the "Circuit 2" and "Circuit 3" of the design flow in Fig. 5.1. Considering the result in Fig. 5.17, it could be seen that "Circuit 1", "Circuit 2" and "Circuit 3" now all have similar response over a relatively wide bandwidth.

The above filter example is fabricated using the multilayer LCP fabrication process from Chapter 2. From Table 5.3, it can be seen that the differences between the values before and after optimisation are very small. This also suggests that the fabrication errors should be well controlled to ensure the fabricated samples have the designed performances. For this reason, all the multilayer capacitors appeared in this design are implemented with three metal layers as in Fig. 5.21 (a) and the middle layer patch is designed to be slightly larger than the first and third layers in Fig. 5.21 (b). In case of some registration errors/shifts among these layers, the structure in Fig. 5.21 (a) and (b) can be less sensitive to such errors and maintain the designed capacitance value.

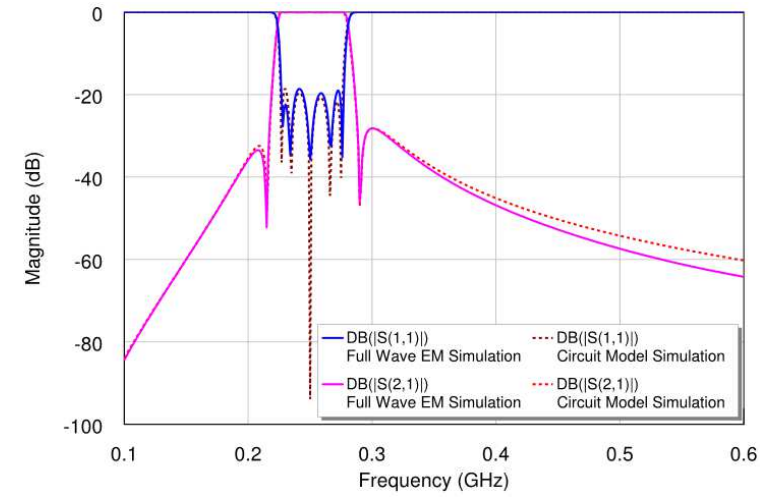

(a)

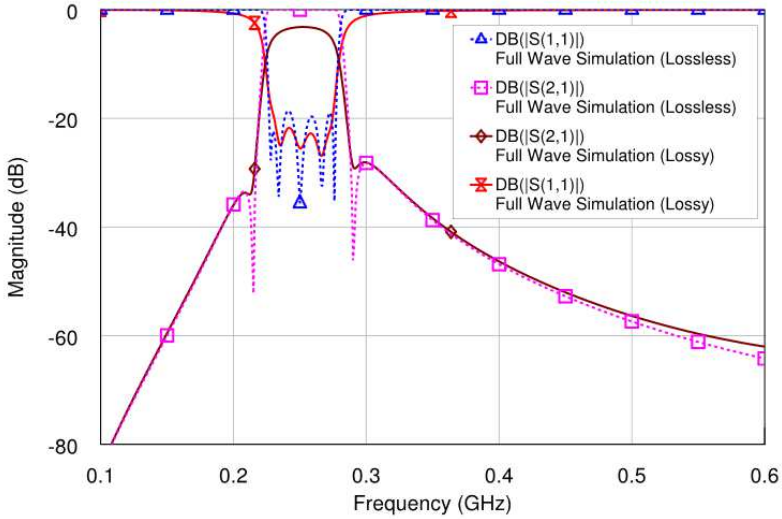

(b)

Fig. 5.20 (a) EM simulation results compared with circuit model results (b) EM Simulation results including conductive and dielectric loss.

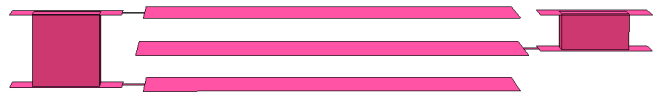

(a)

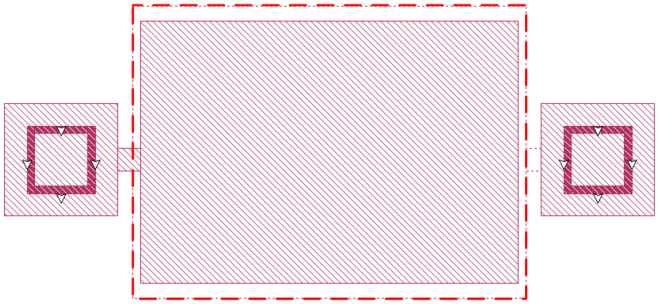

(b)

Fig. 5.21 (a) A modified 3-layer capacitor and (b) its planar structure (dashed-lines are for the middle layer)

Fig. 5.22 (a) shows a fabricated sample for the filter with two transmission zeroes and its measured response in Fig. 5.22 (b) is obtained on an Agilent N5224A VNA. The centre frequency, bandwidth and locations of transmission zeroes of the fabricated sample are almost identical to the simulation result. However, higher insertion loss is observed. According to the simulation, the midband insertion loss is -3.2 dB, while the fabricated sample shows -5.1 dB. This is mainly due to the mismatch in the passband, the extra loss from the via paste and the lower Q of inductors from fabrication. This somehow indicates a trade-off with such a design. Since there are so many elements involved, thus fabrication tolerance should be tightly controlled during the fabrication process, otherwise all the little differences in elements values can largely degrade the passband performance. Considering it's a design for narrow band applications, resistive loss from the vias and tracks should be minimized to reduce the insertion loss.

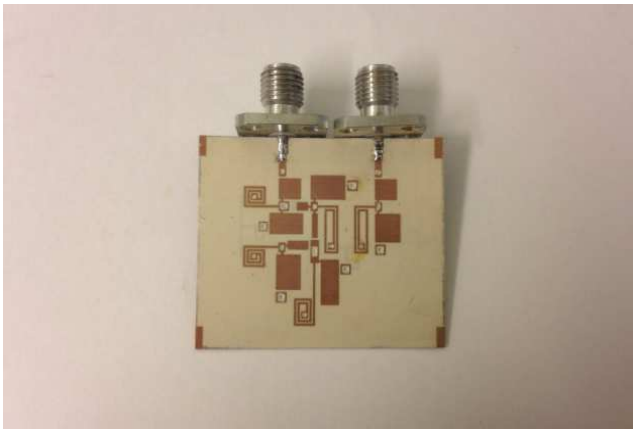

(a)

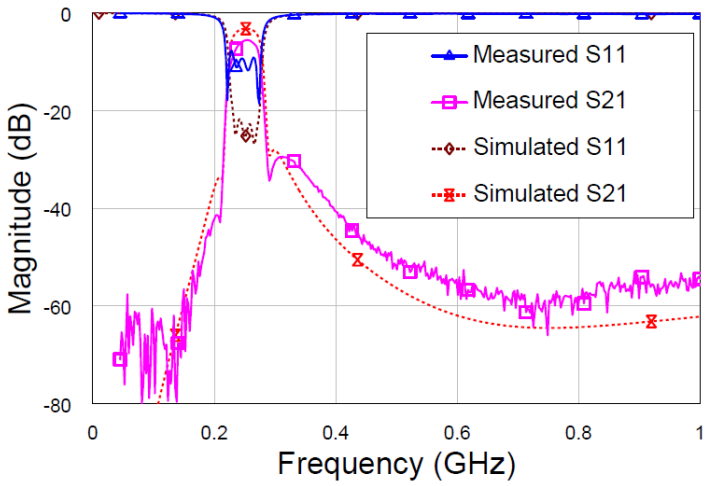

(b)

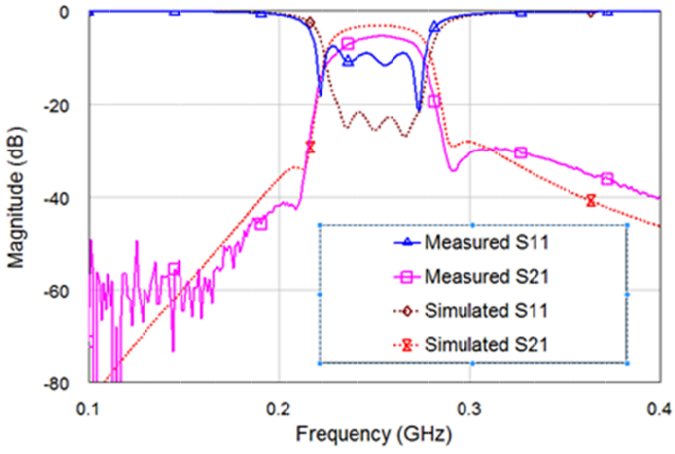

(c)

Fig. 5.22 (a) A photo of the fabricated filter with two transmission zeros, (b) its measured wideband response and (c) narrowband response.

5.6. A Five-pole Coupled Resonator Filter with Five Finite Frequency Transmission zeroes

For an N × N coupling matrix, the maximum number of finite frequency transmission zeroes that can be generated for an N-pole bandpass filter is (N-2) [5.5, 5.6]. Then in order to produce the more finite frequency transmission zeroes, (N+2) × (N+2) coupling matrix was introduced in [5.7], where source and load are included in the coupling matrix. This makes it possible to generate N finite frequency transmission zeroes for an N-pole bandpass filter. A coupling diagram for a fifth order bandpass filter using (N+2) × (N+2) coupling matrix is shown in Fig. 5.23 (a).

When such a (N+2) × (N+2) coupling matrix is involved, theories from Section 5.2 and 5.3 are still applicable. To demonstrate this, a fifth order bandpass filter with five finite frequency transmission zeroes is presented here. The filter has the same centre frequency, *FBW* and passband ripple as the one in Section 5.5. Its transmission zeroes are located asymmetrically outside the passband. Their locations are 201 MHz, 213 MHz, 285 MHz, 314 MHz and 350 MHz, which corresponds to -2.2, -1.6, 1.3, 2.3 and 3.43 in the lowpass domain. By using the synthesis method from [5.7], the normalized (N+2) × (N+2) coupling matrix is obtained and shown in Fig. 5.23 (b).

To get an equal number of capacitive and inductive main couplings, two transformations are applied to the original coupling matrix by using transformation matrix $\mathbf{T_2}$ and $\mathbf{T_3}$. Then the coupling matrix in Fig. 5.23 (c) is obtained. It should emphasize that in the case of (N+2) × (N+2) coupling matrix, the signs of the input and output couplings should be taken into account. This is why the input coupling m_{S1} and output coupling m_{5L} are left to have different signs in Fig. 5.23 (c) in order to have an overall equal number of capacitive and inductive main couplings. By using the same design process as for the filter in Section 5.5, this coupling matrix is implemented as the circuit model in Fig. 5.24 and the elements values for the circuit model, before and after optimisation, are listed in Table 5.4. The circuit model after optimisation has almost identical frequency response as the coupling matrix prototype as shown in Fig. 5.25. The 3-D structure of physical implementation is shown in Fig.5.26 (a), with the full wave EM simulation results [5.19] in Fig. 5.26 (b) and (c). In summary both of the circuit model and the 3-D implementation match well with the

coupling matrix prototype from 0.15 GHz to 0.4 GHz, which corresponds to a FBW of 100%. The dimensions of the filter are $0.0282\lambda_g \times 0.0327\lambda_g \times 0.00052\lambda_g$ (21.7 mm × 25.1 mm × 0.4 mm), where λ_g is the guided wavelength at the centre frequency of 250MHz.

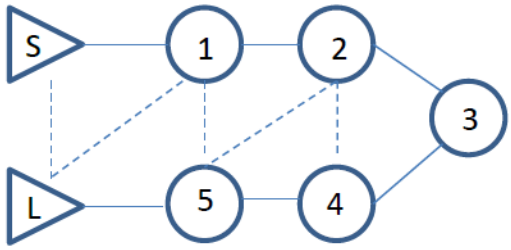

(a)

	S	1	2	3	4	5	L
S		-0.9992	0	0	0	0	0.0134
1	-0.9992	-0.0085	0.8336	0	0	0.0849	0.0400
2	0	0.8336	0.0084	0.5344	-0.2697	-0.2599	0
3	0	0	0.5344	0.4160	0.7060	0	0
4	0	0	-0.2697	0.7060	-0.1438	0.8029	0
5	0	0.0849	-0.2599	0	0.8029	-0.0153	0.9988
L	0.0134	0.0400	0	0	0	0.9988	

(b)

	S	1	2	3	4	5	L
S		-0.9992	0	0	0	0	0.0134
1	-0.9992	-0.0085	-0.8336	0	0	0.0849	0.0400
2	0	-0.8336	0.0084	0.5344	0.2697	0.2599	0
3	0	0	0.5344	0.4160	-0.7060	0	0
4	0	0	0.2697	-0.7060	-0.1438	0.8029	0
5	0	0.0849	0.2599	0	0.8029	-0.0153	0.9988
L	0.0134	0.0400	0	0	0	0.9988	0

(c)

Fig. 5.23 (a) Coupling Diagram for a (N+2)×(N+2) coupling matrix (b) Original Coupling Matrix and (c) transformed matrix for implementation

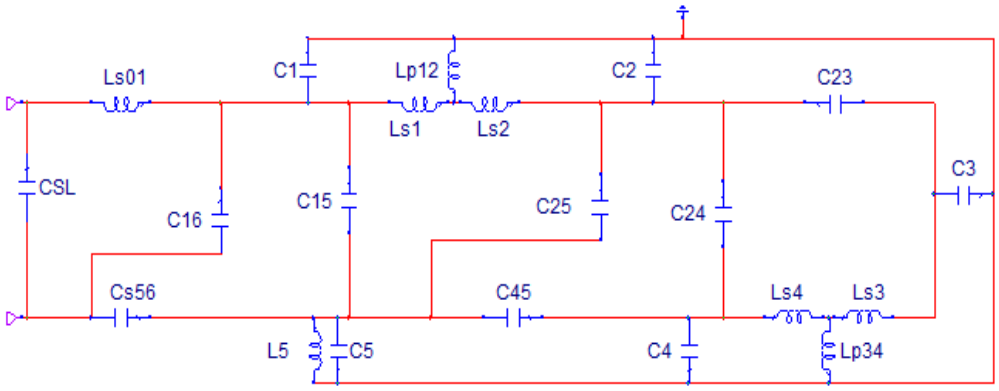

Fig. 5.24 The final circuit model for the (N+2)×(N+2) coupling matrix

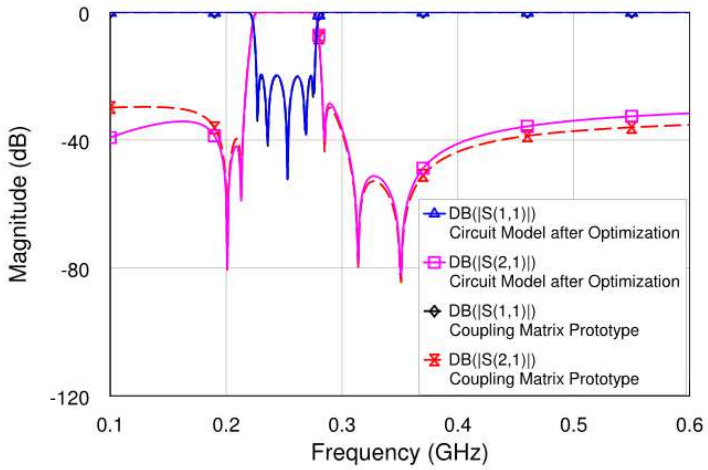

Fig. 5.25 Circuit simulation response versus coupling matrix prototype response

	C1	C2	C3	C4	C5	C23	C45	Cs56
Calculated	26.274pF	21.274pF	22.035pF	21.967pF	14.572pF	2.827pF	4.373pF	10.925pF
After optimization	25.607pF	21.481pF	22.533pF	22.16pF	15.718pF	2.793pF	4.118pF	10.384pF
	Ls1	Ls2	Ls3	Ls4	L5	Lp12	Lp34	Ls01
Calculated	16.906nH	12.181nH	13.166nH	13.166nH	15nH	3.3826nH	2.1307nH	37.09nH
After optimization	17.264nH	12.439nH	12.905nH	12.905nH	15nH	3.2329nH	2.2614nH	41.23nH
	CSL	C16	C15	C25	C24			
Calculated	0.1706pF	0.332pF	0.4593pF	1.405pF	1.467pF			
After optimization	0.1535pF	0.374pF	0.1837pF	1.3466pF	1.282pF			

Table 5.4 Element values for the circuit model in Fig. 5.25.

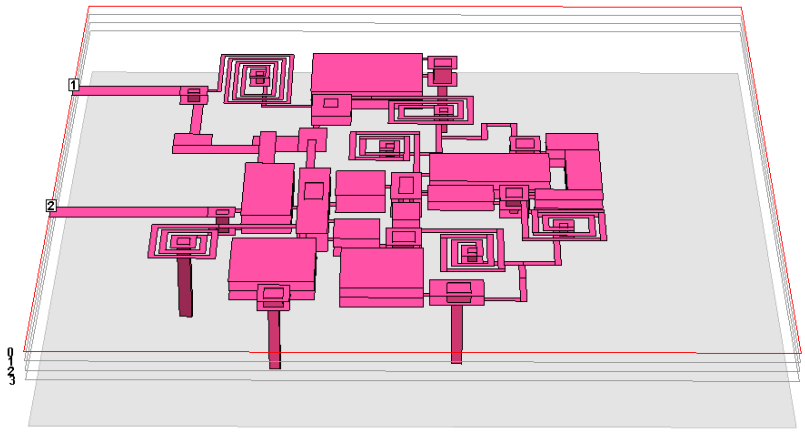

(a)

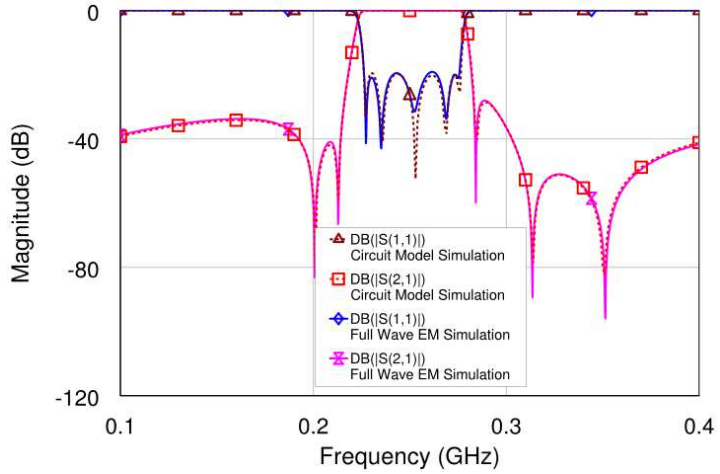

(b)

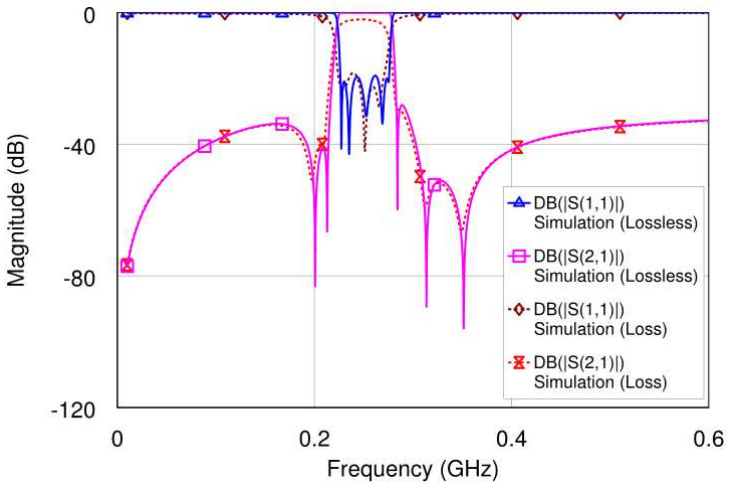

(c)

Fig. 5.26 (a) 3-D structure of the proposed filter (b) Full wave EM simulation versus circuit model simulation (c) Simulation including loss

5.7. General Design Procedure

In Section 5.5 and 5.6, two examples have been presented to demonstrate the application of theories from Section 5.2 and 5.3. From these two examples, a general design procedure for such type of lumped element coupled-resonator filter can be summarised as below:

1) Obtain the coupling matrix and reduce it to a folded form or other simplified forms.

2) Transform the reduced matrix into a form which has equal number of capacitive and inductive main couplings if the order of the filter is odd; if the order is even, the designer can transform the matrix to have one extra capacitive or inductive main coupling, depending on which one gives a "better" response according to the specification.

3) For filters with narrow or moderate bandwidths, any two inductive main couplings should be separated by a capacitive coupling. For wideband bandwidths, this is not necessary.

4) Replace all the ideal inverters in the coupling matrix prototype with lumped element capacitive/inductive inverters; for the input/output coupling, an L-shape matching section can be used.

5) Simplify the circuit model by absorbing all the negative elements into adjacent resonators and then apply π to T transformation if necessary to obtain realizable values for the inductive coupling.

6) Perform an optimisation process to obtain the required performances [5.20].

7) Transform the circuit model into a desired multilayer physical implementation.

5.8. Conclusion

In this chapter, a novel systematic approach for the design of miniature coupled-resonator bandpass filter has been introduced. The approach is based on a new type of matrix similarity transformation to give equal number of capacitive and inductive main couplings to the filter. Then it is proved in the chapter that with equal number of capacitive and inductive main couplings, the filter can have almost identical frequency response with the ideal coupling matrix prototype using frequency-independent inverters.

With these theories presented, a bridge is built between ideal frequency-independent inverters and practical frequency-dependent lumped element inverters. Thus it is possible, for the first time, to design coupled-resonator filters with wideband response match with coupling matrix prototypes using frequency-dependent lumped element inverters. More importantly, theories presented in this chapter can be used to design filters with any order and transmission zeroes can be pre-defined at arbitrary locations.

To demonstrate how these theories can be applied to the design of miniature filters, two bandpass filters are designed to cover both N × N and (N+2) × (N+2) matrices. A detailed design procedure is summarised in the chapter and circuit transformations have been introduced to make sure that synthesized filter have realisable values for all the elements. It is also the first time that, such filters with narrow/moderate bandwidths and finite frequency transmission zeroes are designed and fabricated using multilayer LCP technology. Thus this chapter together with Chapter 4 complete the development of multilayer LCP filters for narrow/moderate bandwidth applications.

For higher frequency applications, the proposed design approach may also be useful. However, fabrication and loss might be the two main challenges, as the spiral lines for inductors have to be much thinner to provide a high self-resonant frequency. This would decrease the Q and increase the insertion loss. Potentially, the idea presented in this paper is also applicable to coupled-distributed-resonator filter design and this should be investigated in future and might be a solution for high frequency applications.

References

[5.1] R. Hershtig, R. Levy, and K. Zaki, “Synthesis and Design of Cascaded Trisection (CT) Dielectric Resonator Filters”, in *Proc. Eur. Microw. Conf.*, Sept. 1997, pp. 784–791.

[5.2] J.-S. Hong and M. J. Lancaster, “Microstrip Cross-Coupled Trisection Bandpass Filters with Asymmetric Frequency Characteristics,” *IET Microw. Antenna Propagat.*, vol. 146, no. 1, pp. 84-90, Feb. 1999.

[5.3] R. J. Cameron, and J. D. Rhodes, “Asymmetric Realization for Dual-Mode Bandpass Filters,” *IEEE Tran. Microw. Theory Tech.*, vol. 29, no. 1, pp. 51-58, Jan. 1981.

[5.4] R. Levy, “Direct Synthesis of Cascaded Quadruplet (CQ) Filters,” *IEEE Trans. Microw. Theory Tech.*, vol. 43, no. 12, pp. 2940-2945, Dec. 1995.

[5.5] A. E. Atia, A. E. Williams, and R. W. Newcomb, “Narrow-band multiple-coupled cavity synthesis,” *IEEE Trans. Circuits Syst.*, vol. 21, no. 5, pp. 649–655, Sept. 1974.

[5.6] R. J. Cameron, “General Coupling Matrix Synthesis Methods for Chebyshev Filtering Functions,” *IEEE Trans. Microw. Theory Tech.* ., vol. 47, no. 4, pp. 433-442, Apr. 1999.

[5.7] R. J. Cameron, “Advanced Coupling Matrix Synthesis Techniques for Microwave Filters,” *IEEE Trans. Microw. Theory Tech.*, vol. 51, no. 1, pp. 1-10, Jan. 2003.

[5.8] S. Amari, F. Seyfert, and M. Bekheit, “Theory of Coupled Resonator Microwave Bandpass Filters of Arbitrary Bandwidth,” *IEEE Trans. Microw. Theory Tech*., vol. 58, no. 8, pp. 2188-2203, Aug. 2010.

[5.9] W. Meng, H.-M. Lee, K. A. Zaki and A. E. Atia, “Synthesis of Wideband Multicoupled Resonator Filters,” *IEEE Trans. Microw. Theory Tech.*, vol. 59, no. 3, pp. 593-603, Mar. 2011.

[5.10] R. J. Cameron, C. M. Kudsia, and R. R. Mansour, *Microwave Filters for Communication Systems: Fundamentals, Design, and Applications*. New York, Wiley, 2007.

[5.11] F. R. Gantmacher, *The Theory of Matrices*, vol. 1, Chelsea Publishing, New York, 1959.

[5.12] G. Matthaei, L. Young and E. M. T. Jones, *Microwave Filters, Impedance-Matching Networks, and Coupling Structures*, Artech House, Norwood, MA, 1980.

[5.13] J.-S. Hong, *Microstrip Filters for RF/Microwave Applications*, 2nd Edition. New Jersey: Wiley, 2011.

[5.14] Guidedwavetech.com, (2014). Coupling Matrix Filter Tool. [online] Available at: http://www.guidedwavetech.com/coup/poles1.htm [Accessed 10 Jan. 2014].

[5.15] S. Qian, and J.-S. Hong, “A compact multilayer liquid crystal polymer VHF bandpass filter,” *43rd Eur. Microw. Conf*. 2013, pp.1207-1210, Oct. 2013, Nuremberg.

[5.16] Z.-C. Hao and J.-S. Hong, “Ultra-Wideband Bandpass Filter Using Multilayer Liquid-Crystal-Polymer Technology,” *IEEE Trans. Microw. Theory Tech.*, vol. 56, no. 9, pp. 2095-2100, Sept. 2008.

[5.17] Z.-C. Hao and J.-S. Hong, “UWB Bandpass Filter Using Cascaded Miniature High-Pass and Low-Pass Filters With Multilayer Liquid Crystal Polymer Technology,” *IEEE Trans. Microw. Theory Tech.*, vol. 58, no. 4, pp. 941-948, Apr. 2010.

[5.18] S. Qian and J.-S. Hong, “Miniature Quasi-Lumped Element Wideband Bandpass Filter at 0.5-2 GHz Band Using Multilayer Liquid Crystal Polymer Technology,” *IEEE Trans. Microw. Theory Tech.*, vol.60, no. 9, pp.2799-2807, Sept. 2012.

[5.19] Sonnet *em*, EM User’s Manual, Version 12, NY 2009.

[5.20] AWR Microwave Office, Appl. Wave Res. Inc., Version 2009, El Segundo, CA, 2007.

Chapter 6

A Low Loss Implementation of a Channel-Reconfigurable Filter in a Multilayer LCP Package

6.1. Introduction

In previous chapters, the design and fabrication of bandpass filters using multilayer LCP technology have been discussed. Both wideband and narrow band filters have been presented, which proves that multilayer LCP technology is a promising solution for the design of miniature bandpass filters. However, there is an increasing demand for compact reconfigurable filters, so it would be interesting to implement reconfigurable filters on multilayer LCP substrates.

During the past a few years, various types of electronically reconfigurable filters have been developed for novel software-defined and cognitive radio systems. In terms of reconfigurable components, varactors [6.1]-[6.3], PIN diodes [6.4]-[6.6] and microelectromechanical systems (MEMS) switches [6.7]-[6.9], are usually used. In [1] thin-film barium–strontium–titanate (BST) varactors are integrated into a traditional planar combline filter and a tuning range of 16% is achieved. For improved selectivity and high attenuation in the stopband, a tunable combline filter with source-load coupling is reported in [6.2]. Apart from combline filter, tunable filters based on novel compact dual-mode resonators are investigated in [6.3] and 41% of tuning range is reported. For PIN diodes, they can be used to implement a filter with reconfigurable bandwidths as in [6.4], both reconfigurable bandwidths and central frequencies in [6.5] and switchable notch band in an ultra-wideband (UWB) bandpass filter as in [6.6].

However, for some cognitive radio and radar applications, where a large number of states/channels are needed, the above work has some limitations. Varactors can be used to perform continuous tuning to obtain lots of channels, but they have low linearity and high loss. PIN diodes have very fast switching speed and high linearity but to achieve lots of states, a large number of PIN diodes are usually needed, which increases the cost and loss. To solve this, the work in [6.7]-[6.10] is aimed at realising large number of channels using different approaches. [6.7]-[6.9] adopt MEMS switched capacitor banks and large numbers

of channels are achieved, such as a 4-bit, 16-channel filter reported in [6.9]. These channels are adjacent to each other and thus the filter works in a similar fashion to a continuously tuned filter. Recently, a novel approach of channel-reconfigurable filter was reported in [6.10] using more widely used PIN diodes, instead of MEMS switches, for high linearity, fast and more reliable switching. The filter is based on cascaded bi-modal optimum stub filters [6.11, 6.12], and by using 4 stages and switching each stage between lowpass mode and highpass mode as shown in Fig. 6.1, the microstrip filter can realise 16 narrow channels to cover the frequency range from DC to 2.5 GHz. In total, 22 diodes are used to connect/disconnect the stubs with ground.

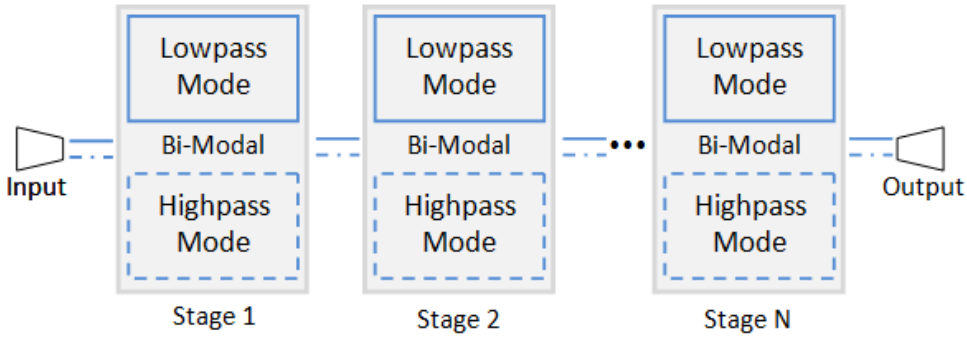

Fig. 6.1 Reconfigurable filter by using cascaded bi-modal optimum stub filters [10].

Although the idea proposed in [6.10] is promising for channel-reconfigurable filters, it is worth further development to improve the performance and solve existing problems. First of all, to implement a bi-modal stage which can behave as either an open-stub/lowpass, or short-stub/highpass filter, PIN diodes in [6.10] are all placed at the end of stubs to connect/disconnect them with grounding vias. The more stubs, the more PIN diodes. In this case, the cost and loss of the filter will be increased when more stubs and greater selectivity are needed. In particular, all of the pin diodes are placed at the end of each stub, which is the point with high RF current density when the PIN diode is switched on. This generates high insertion loss for the filter especially when all the PIN diodes are switched on. In addition, since the loss from PIN diodes are usually proportional to the frequency, it is highly desirable that fewer PIN diodes should be used for a higher frequency application.

In addition to the above high loss and high cost problems, there is also an issue to correctly design such a filter in [6.10]. With such a large amount of PIN diodes, it is challenging and time consuming to compensate for their non-ideal effects, so that those bi-modal optimum

stub filters can have a periodic response over a wide band. The dispersion from microstrip transmission lines makes this a more serious matter at higher frequency.

To address these concerns, this work is carried out to develop a low cost and low loss implementation, which can tackle the problems above and improve performance of the filter. In section 6.2, the reconfiguration approach and design of bi-modal stages are discussed. The fabrication and measured results including *S* and nonlinearity parameters of the filter as a multilayer LCP package is presented in Section 6.3. This is followed by a summary and suggestion of future work in Section 6.4.

6.2. A Channel-Reconfigurable Filter

6.2.1. Open and Short Stub Filters

In [6.11] and [6.12], a type of filter as shown in Fig. 6.2 (a) and (b) has been reported. This type of filter consists of a cascade of open or short stubs of electrical length θ_0 at the cutoff frequency f_c, separated by connection lines of electrical length $2\theta_0$. Usually, for a distributed filter with 3 stubs, it only generates a third order filter response. However, for the type in Fig. 6.2 (a) and (b), it can actually generate a fifth order frequency response, as the connection lines are not redundant and contribute to the order of the filter [6.12]. This gives the filter a fast rate of cutoff. In this sense, it is called an optimum filter.

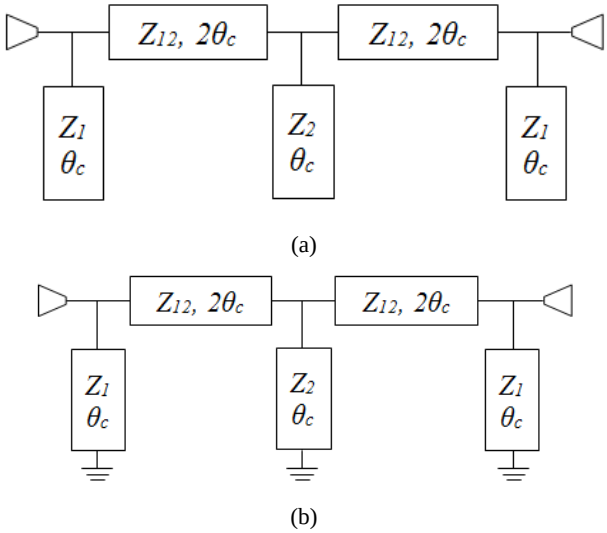

Fig. 6.2 (a) Optimum open stub filter with a highpass/bandpass response (b) Optimum short stub filter with a lowpass/bandstop response.

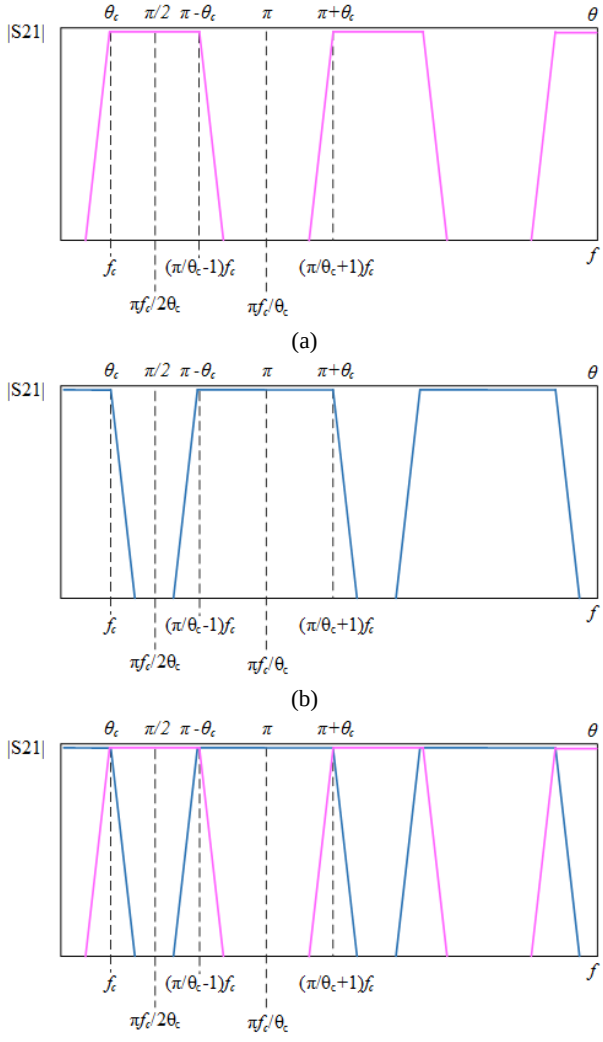

Fig. 6.3 (a) Optimum open stub filter (b) Optimum short stub filter (c) bi-modal operation

Another important characteristic for the optimum stub filter is its capability of producing a periodic response. For the open-stub filter, at low frequencies, it can be regarded as a highpass filter. As the frequency increases, it starts generating its harmonic passbands, as shown in Fig. 6.3(a). If all of the open stubs in Fig. 6.2(a) are changed to short stubs as shown in Fig. 6.2(b), all of the passbands in Fig. 6.3(a) become stopbands and *vice versa*, as shown in Fig. 6.3(b). This "inversion" is summarised in Fig. 6.3 (c), where red lines and blue lines denote open and short stubs respectively. It should be mentioned that although optimum open and short stub filter produces periodic bandpass response, in this chapter they are still referred as lowpass and highpass filters, which is based on their low frequency responses.

6.2.2. A Cascade of Bi-Modal Optimum Stub Filters

Considering a 3-stage cascaded filter example in Fig. 6.4, each stage can work as either an open stub or short stub filter. Theoretically, 8 different frequency responses can be obtained. If it is required that each frequency response only contains one passband with the same absolute bandwidth B_0, then two conditions must be satisfied. Firstly, the N-th stage should be designed to have a bandwidth $2^{(N-1)}$ times as wide as the first stage. Secondly, for each stage the bandwidth of the passband (excluding the highpass or lowpass passband) should be equal to the stopband. If these two conditions are met, as shown in Fig. 6.5 (a), (b) and (c), then 8 channels with an equal bandwidth can be obtained. This is highlighted as in Fig. 6.5 (d). It should be mentioned that to eliminate all the harmonic passbands outside the operating frequency range, a lowpass filter ought to be added for practical applications. Since this work is to demonstrating the idea only, this is not considered here.

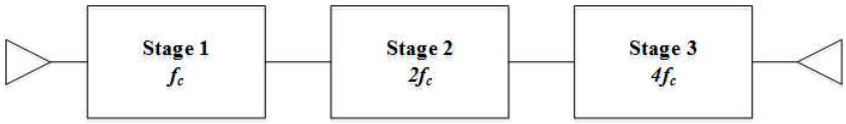

Fig. 6.4 A Cascade of two bi-modal stages (f_c is lowpass cutoff frequency when stage 1 is in open stub mode)

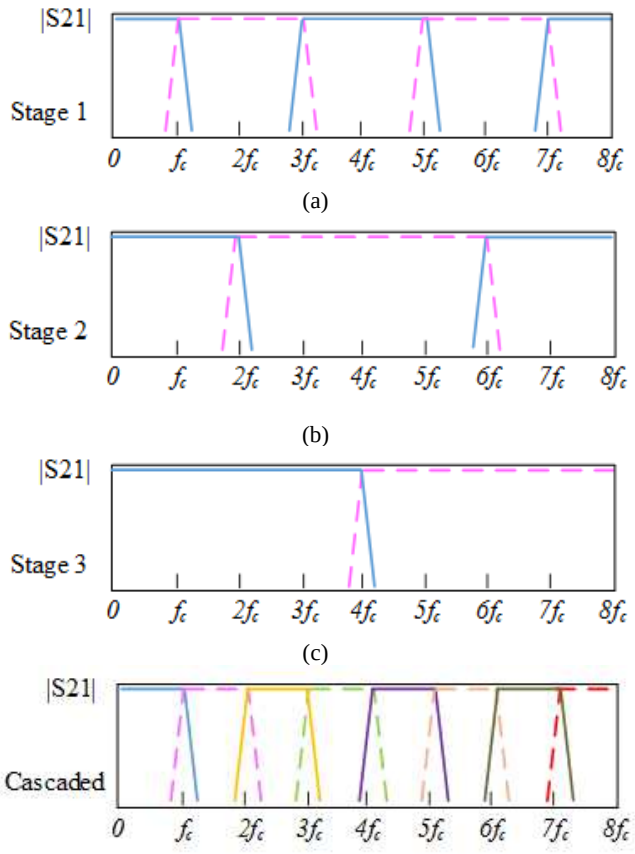

Fig. 6.5 Frequency responses of (a) the first stage, (b) second stage and (c) third stage; (d) 8 channels by cascading

6.2.3. Reconfiguration Approach

In this chapter, a cascade of bi-modal stages in Fig. 6.6 is used to implement the channel-reconfigurable filter. Compared with the work in [6.10], there are several improvements.

Firstly, instead of switching a stub filter between open and short stub mode using PIN diodes, this work uses two filters in one bi-modal stage as shown in Fig. 6.6 to remove PIN diodes from the filter. This does not only reduce the insertion loss, but also make it possible to design the two filters separately without the need of compensating for the non-ideal effect from PIN diodes. In such a way, both filters can be optimised to give the required response and form a desired bi-modal stage.

Secondly, double pole double throw switches (DPDT) are inserted between any two adjacent stages in order to choose the required filter from each stage. In such a way, an N-stage filter can produce 2^N different responses. Since these DPDT switches are usually made of PIN diodes internally, to quantify the number the PIN diodes that are actually used in this implementation, every DPDT switch can be replaced by 4 PIN diodes. In this case, 16 diodes are needed for a 4-stage filter; while in [6.10] 22 diodes are used for a 4-stage design. More importantly, with the implementation discussed here, the total number of PIN diodes needed is not related to the number of stubs. This makes it possible to use high order filters in each stage without using more diodes. Furthermore, using the approach in Fig. 6.6, there will be 8 diodes switched on for every configuration. However, in [6.10], it is a value between 0 and 22, which means there will be one configuration suffering from all the loss from PIN diodes. As a summary, Table 6.1 and 6.2 listed the number of PIN diodes needed for the implementation in this work, and the number of PIN diodes that needs to be switched on, respectively, in comparison with the implementation in [6.10].

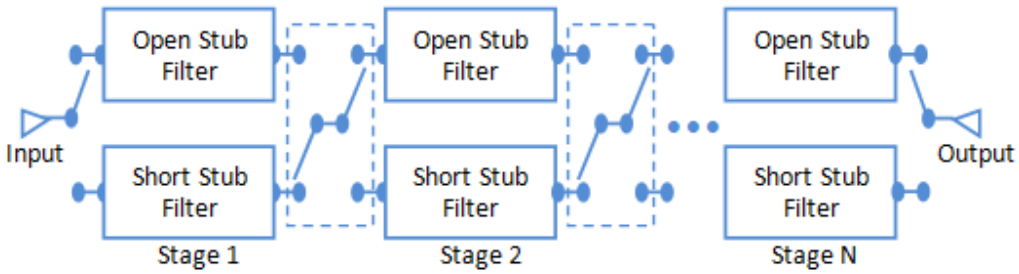

Fig. 6.6 A Cascade of Bi-modal Stages using DPDT switches

Number of PIN Diodes	2-bit	3-bit	4-bit	5-bit
Proposed Design	8	12	16	20
Design in [6.10]	9	15	22	30

Table 6.1 The number of PIN diodes needed

Number of PIN Diodes	2-bit	3-bit	4-bit	5-bit
Proposed Design	4	6	8	10
Design in [6.10]	9	15	22	30

Table 6.2 The maximum number of PIN diodes switched on

Although the implementation in Fig. 6.6 has many advantages in comparison with [6.10], its main drawback is that it requires (2 × N) filters for an N-stage design. This will increase the overall size of the reconfigurable filter.

6.2.4. Stripline Implementaion of a 2-Stage Channel-Reconfigurable Filter using Multilayer LCP technology

To demonstrate the reconfiguration approach, a 2-stage channel-reconfigurable filter is designed to cover the frequency range from DC to 4 GHz. The lowpass cutoff frequencies for the 2 stages are set to 1 GHz and 2 GHz, respectively, as shown in Fig. 6.7 (a) and (b). To maintain similar selectivity for each channel, the number of stubs is increased by one if the passband bandwidth is doubled, as suggested in [6.10]. To demonstrate this in a straightforward manner, the two stages in this work are chosen to be 2-stub and 3-stub respectively, which is for the consideration of both acceptable selectivity and small filter size.

The synthesis of optimum stub filter was detailed in [6.11] and [6.12] but are briefly discussed here for quick reference. Considering the periodic response in Fig. 6.3 (a) of optimum stub filter, Formula (6.1) is obtained by making the passband and stopband having the same bandwidth. It can then be found that θ_c, which is the electrical length of the stubs in Fig. 6.2, should be 45 degrees at the lowpass cutoff frequency. Then the characteristic impedance of the n-th stub Z_n can be obtained using (6.2), which is from Richard transformation [6.13], and C_n is the required shunt capacitance in the equivalent Chebyshev π-network lowpass circuit. By using *ABCD* parameter matching, formula (6.3) can be used to calculate the characteristic impedance of the connection line $Z_{n,n+1}$ between stub n and n+1, and $L_{n,n+1}$ is the required series inductance in the equivalent Chebyshev π-network

lowpass circuit. In this work, the 2-stub filter design uses a third-order 0.1 dB ripple Chebyshev lowpass prototype with element values of $g_1 = g_3 = 1.0316$, $g_2 = 1.1474$, and $g_0 = g_4 = 1.0$; while the 3-stub filter design deploys a fifth-order 0.1 dB ripple Chebyshev lowpass prototype whose element values are $g_1 = g_5 = 1.1468$, $g_2 = g_4 = 1.3712$, $g_3 = 1.9750$, and $g_0 = g_6 = 1.0$.

Although (6.1)-(6.3) give a close approximation for the optimum stub filter design, the original parameters obtained by using these formulae need to be slightly tuned to meet the 3 dB bandwidth specifications. The original and final design parameters are listed in Table 6.3. Fig. 6.7 shows frequency responses of filter models obtained using the original and tuned design parameters.

$$\pi - 2\theta_c = 2\theta_c \tag{6.1}$$

$$-j(\omega_0 \cdot C_n)^{-1} = -\mathrm{j} \cdot \mathrm{Z_n} \cdot \cot\theta_0 \tag{6.2}$$

$$j \cdot \omega_0 \cdot L_{n(n+1)} = j \cdot Z_{n(n+1)} \cdot \sin(2\theta_0) \tag{6.3}$$

		Z_1	Z_{12}	Z_2
2-Stub	Original	48.5	57.4	
	Optimised	46.0	62.0	
3-Stub	Original	43.6	65.6	25.3
	Optimised	48.4	58.0	32.2

Table 6.3 Original and optimized design parameters.

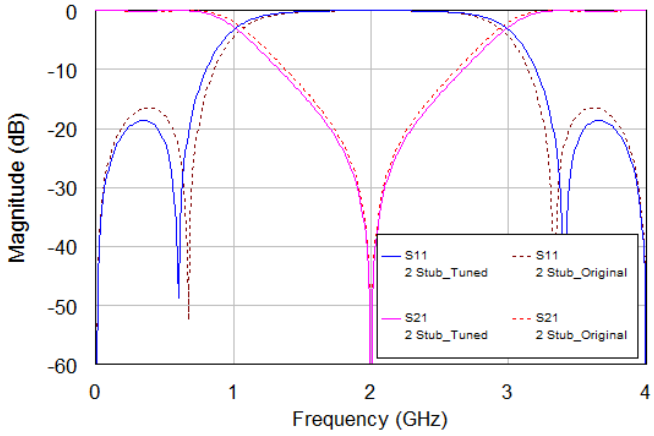

(a)

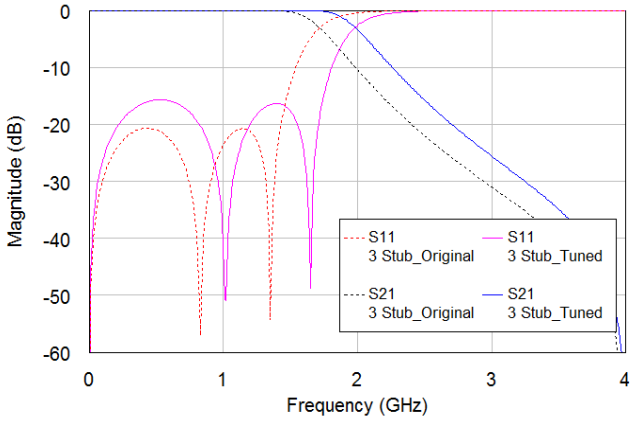

(b)

Fig. 6.7 Frequency responses of circuit models using the original and tuned design parameters. (a) 2-stub filter. (b) 3-stub filter.

Since it is very important to maintain the periodicity of the frequency responses as shown in Fig. 6.5, stripline is chosen to implement these optimum stub filters instead of microstrip, which was used in [6.10]. This can eliminate the dispersion issue with microstrip, thus making it possible to obtain high order harmonics at desires frequencies.

Due to the distributed line elements, the whole filter will have a large footprint if no miniaturization is used. To minimise the footprint, all the stubs and connection lines are implemented as meander lines. All these meander lines are simulated separately until they demonstrate the required electrical length and frequency response. They are then formed together in a special topology to minimise unwanted cross coupling among closely located transmission-line elements. Fig. 6.8(a) shows the 3D view for the miniature 2-open-stub

stripline filter, as an example. It has planar dimensions of 13.6 mm × 14.3 mm as shown in Fig. 6.8 (b) and its full wave simulation result [6.14] is shown in Fig. 6.8 (c), from which it can be seen that very good periodicity has been achieved, especially in comparison to a microstrip implementation. The frequency response of the stripline configuration shows good periodicity up to 12 GHz, whereas the microstrip one even cannot produce a good response after the first harmonic due to dispersion.

The other filters in this design can be implemented in a similar way, and then the whole reconfigurable filter has a form as shown in Fig. 6.9 (a).

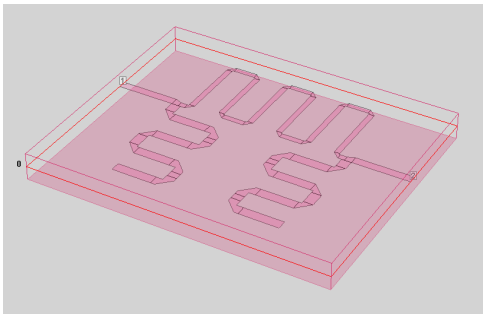

(a)

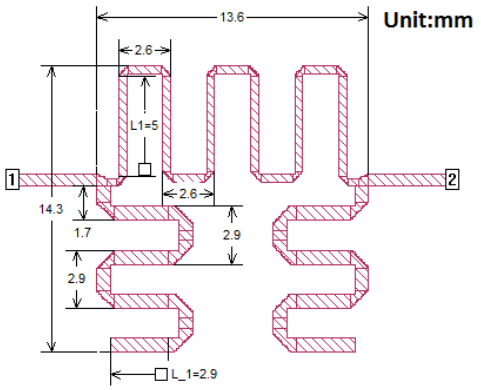

(b)

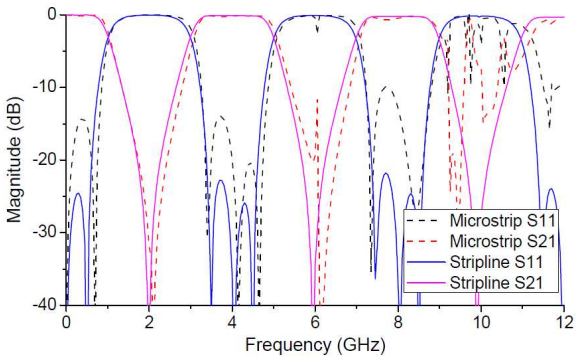

(c)

Fig. 6.8 stripline 2-open-stub filter (a) 3D view of the stripline filter (b) Dimensions of the filter (b) Full-wave Simulation result of the stripline filter compared with dispersive microstrip filter.

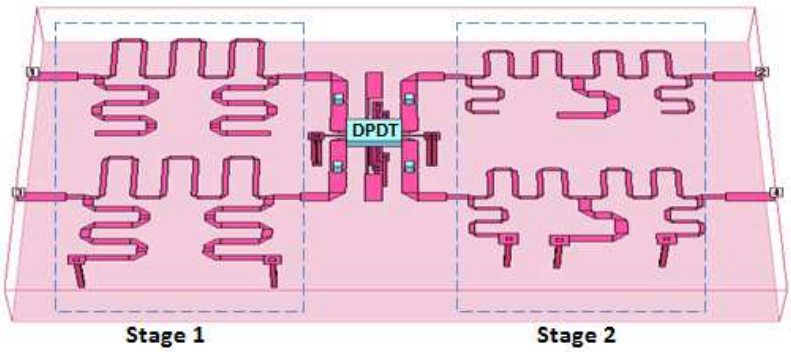

(a)

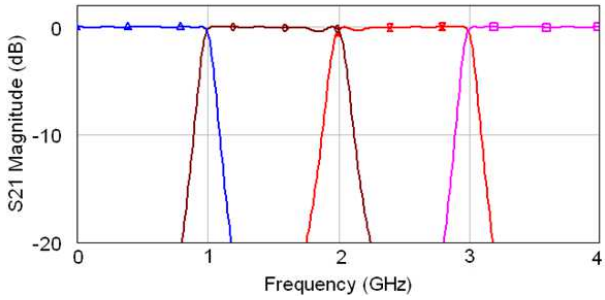

(b)

Fig. 6.9 (a) The whole reconfigurable filter with 2 bi-modal stages and DPDT switches (b) S21 of the 4 channels from full wave EM simulation

6.3. Fabrication and Measurement

With multilayer LCP technology, stripline structures can be easily fabricated by the method shown in Fig. 6.10. Compared to traditional thick substrate based stripline structures, LCP technology gives more flexibility in terms of substrate thickness. To connect the top and bottom ground layers together, connection vias are drilled by CO_2 laser and then plated by high conductivity paste using through-hole plating technique for LCP [6.15].

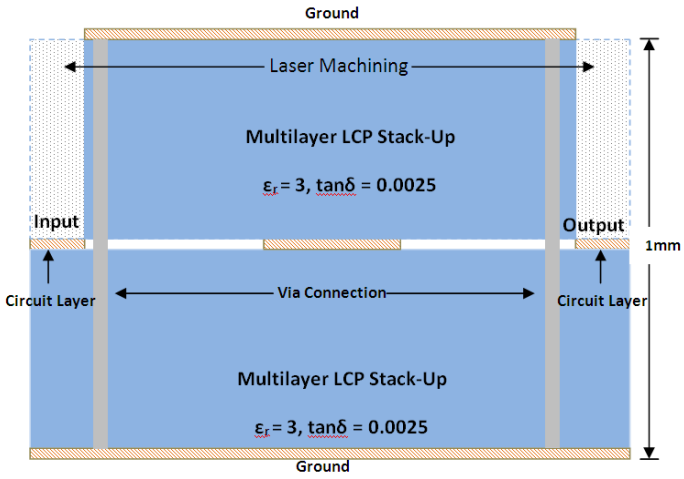

(a)

Fig. 6.10 Stripline circuit using multilayer LCP technology

As an example, Fig. 6.11 (a) is a photograph of a stripline 2-open-stub filter fabricated using multilayer LCP technology. The copper tracks for the filter, as referring to Fig. 6.10, are on the middle layer. Within the multilayer lamination process, a stack-up of 1 mm thickness is made to implement the stripline structure as shown in Fig. 6.10, resulting in a compact and light-weight filter. Fig. 6.11 (b) shows the measured response of the fabricated 2-open-stub filter, compared with simulated response. It can be seen that, apart from some mismatch problems, which are due to fabrication tolerance, the periodic response of the stripline filter has been well maintained up to 10 GHz.

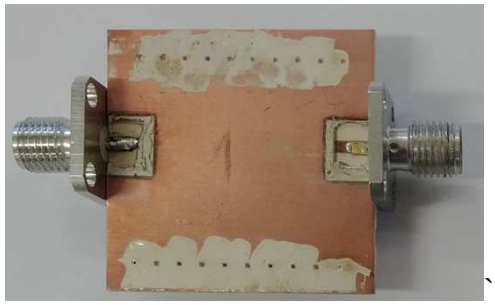

(a)

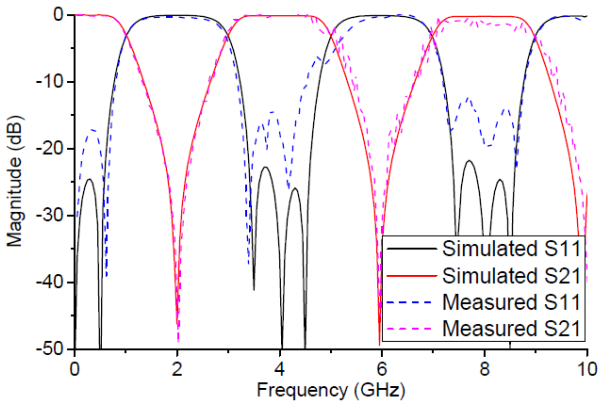

(b)

Fig. 6.11 A fabricated sample of the 2-open-stub filter

The fabricated reconfigurable filter is shown in Fig. 6.12 (a) and it has a planar size of 4.3 cm × 3.6 cm. The embedded filter layout is similar to Fig. 6.9 (a). Then, by using high precision CO_2 laser, a window can be opened and thus the DPDT switch can be easily integrated into the LCP package, as shown in Fig. 6.12 (b). Measured S21 is shown in Fig. 6.12 (c). Table 6.4 lists the 3 dB cutoff frequencies and mid passband insertion loss of each channel. It can be seen that due to non-dispersive stripline configuration, all of the 4 channels have roughly the same absolute bandwidth. Since the absolute bandwidth is constant, the fractional bandwidth is then reduced while the insertion loss increased from the state 1 to state 4. Nevertheless, the loss of filter is reasonably small. The DPDT switch being used in this work is the MA-Com MASWSS0129 broadband DPDT GaAs MMIC switch.

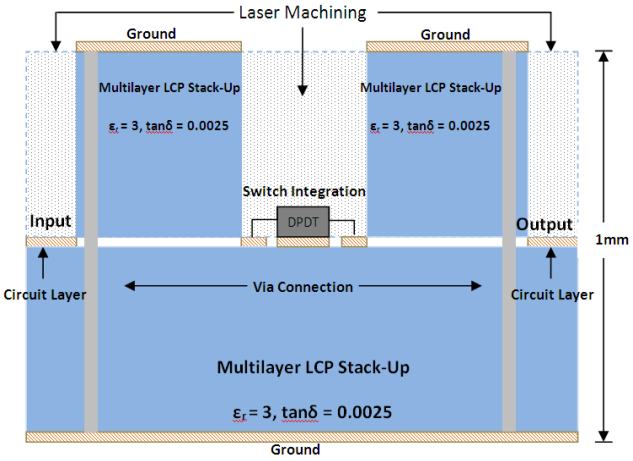

(a)

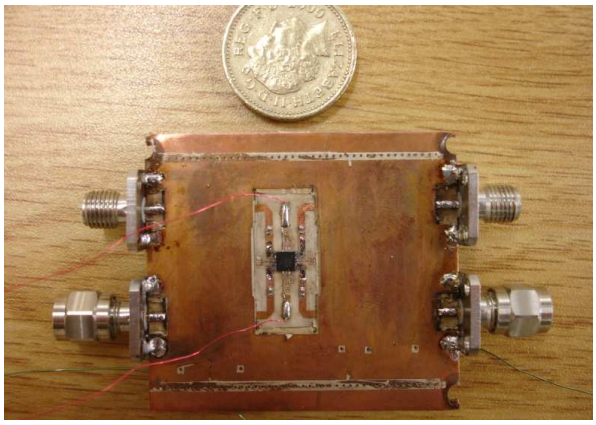

(b)

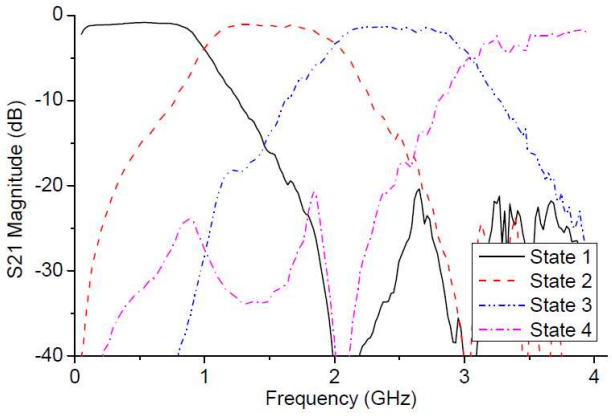

(c)

Fig. 6.12 (a) Multilayer LCP stripline circuit with integrated MMIC switch (b) Fabricated reconfigurable filter (c) Measured S21 of the 4 channels.

	State 1	State 2	State 3	State 4
Mid-band Passband Insertion Loss (dB)	0.8	1.0	1.4	1.7
3-dB bandwidth (GHZ)	0 - 1.02	0.98-2.01	2.00-3.05	3.02-4

Table 6.4 Measured insertion loss and 3dB bandwidth of different channels

Third-order intercept point (IP3) testing of the whole filter has also been carried out in this work. The setup of this test is shown in Fig. 6.13, where in order to obtain a 0 dBm power level, two broadband amplifiers were used. The tones generated from signal sources have a frequency difference of $\Delta f = f_2 - f_1$. Fig. 6.14 (a) shows the measured result of the IP3 at the centre frequency of each channel. For the 1-dB compression point test, the filter can handle an input power of at least 25 dBm, which is sufficient for most applications, without any power compression. Fig. 10(b) shows the measured output power when the input power is increased from -10 dBm to 25 dBm for the State 2, as an example.

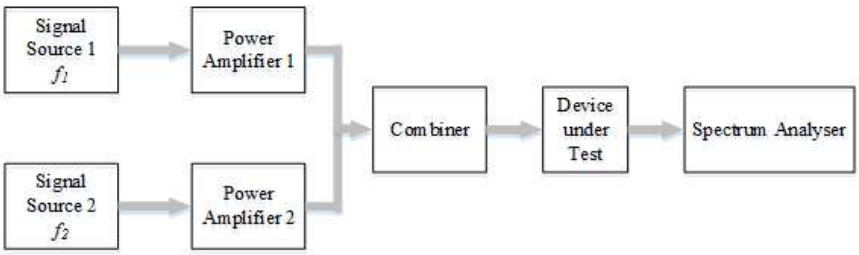

Fig. 6.13 Setup for IP3 measurement

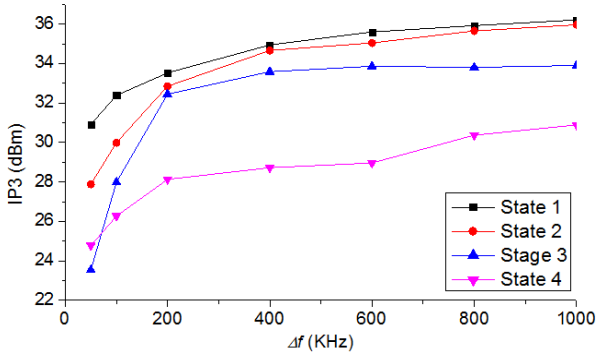

(a)

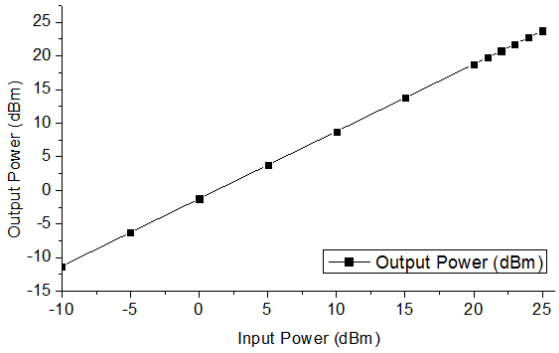

(b)

Fig. 6.14 (a) IP3 measurement for 4 channels with bandwidths shown in Table 6.4 (b) compression point measurement for State 2.

6.4. Conclusion

In this chapter, an improved implementation of channel-switchable reconfigurable filter consisting of bi-modal filtering stages has been proposed. Compared with previous implementations, this work significantly reduces the number of PIN diodes needed, which reduces both the cost and loss of the reconfigurable filter. Furthermore, with a new reconfiguration scheme, every bi-modal stage consists of a highpass filter and a lowpass filter. These two filters can be designed and optimized separately to obtain the required periodic response. To eliminate the dispersion and obtain periodic responses, all these filters are implemented with stripline technology. Low-cost and light-weight multilayer LCP circuit technology and advanced CO_2 laser machining are used for the fabrication and the whole filter is implemented as a compact LCP package. As a preliminary investigation, this work has shown that the proposed design for realising electronically reconfigurable channel filters is attractive for further developments.

References

[6.1] J. Nath, D. Ghosh, J.-P. Maria, A. I. Kingon, W. Fathelbab, P. D. Franzon, and M. B. Steer, "An electronically tunable microstrip bandpass filter using thin-film barium-strontium-titanate (BST) varactors," *IEEE Trans. Microw. Theory Tech.*, vol. 53, no. 9, pp. 2707-2712, Sept. 2005.

[6.2] M. Sanchez-Renedo, "High-Selectivity Tunable Planar Combline Filter With Source/Load-Multiresonator Coupling", *IEEE Microw. Wireless Compon. Lett.*, vol. 17, no. 7, pp. 513-515, July 2007.

[6.3] W. Tang and J.-S. Hong, "Varactor-Tuned Dual-Mode Bandpass Filters", *IEEE Trans. Microw. Theory Tech.*, vol. 58, no. 8, pp. 2213-2219, Aug. 2010.

[6.4] A. Miller and J.-S. Hong, "Wideband Bandpass Filter with Reconfigurable Bandwidth," *IEEE Microw. Wireless Compon. Lett.*, vol. 20, no. 1, pp. 28-30, Jan. 2010.

[6.5] M. A. Sanchez-Soriano and J.-S. Hong, "Reconfigurable Lowpass Filter Based on Signal Interference Techniques", in *Proc. 2011 IEEE MTT-S Int. Microwave Symp.*, June 2011, pp. 1–4.

[6.6] Z.-C. Hao and J.-S. Hong, "UWB Bandpass Filter with Switchable Notching Band using Multilayer LCP Technology", *in Proc. 2010 European Microwave Conf.*, Sept. 2010, pp. 17-20.

[6.7] C. Palego et al., "A Two-Pole Lumped-Element Programmable Filter With MEMS Pseudodigital Capacitor Banks," *IEEE Trans. Microw. Theory Tech.*, vol. 56, no. 3, pp. 729-735, Mar. 2008.

[6.8] S.-J. Park, M. A. El-Tanani, I. Reines and G. M. Rebeiz, "Low-Loss 4–6-GHz Tunable FilterWith 3-Bit High-Q Orthogonal Bias RF-MEMS Capacitance Network", *IEEE Trans. Microw. Theory Tech.*, vol. 56, no. 10, Oct. 2008, pp. 2348-2355.

[6.9] K. Entesari and G. M. Rebeiz, "A differential 4-bit 6.5-10GHz RF MEMS tunable filter," *IEEE Trans. Microw. Theory Tech.*, vol. 53, no.3, pp. 1103-1110, Mar. 2005.

[6.10] M. Koochakzadeh and A. Abbaspour-Tamijani, “Multiresolution Channel-Select Filter with Ultrawide Frequency Coverage,” *IEEE Trans. Microw. Theory Tech.*, vol. 58, no. 5, pp. 1205-1212, May 2010.

[6.11] R. Levy, “A new class of distributed prototype filters with applications to mixed lumped/distributed component design,” *IEEE Trans.*, *MTT-18*, Dec. 1970, 1064-1071.

[6.12] J.-S. Hong, *Microstrip Filters for RF/Microwave Applications*, 2nd Edition. New Jersey: Wiley, 2011.

[6.13] P. I. Richards, “Resistor-transmission-line circuits,” *Proc. IRE. Trans. Microw. Theory Tech.*, 36, 217–220, Feb. 1948.

[6.14] Sonnet *em*, EM User’s Manual, Version 12, NY 2009.

[6.15] S. Qian and J.-S. Hong, “Miniature Quasi-Lumped Element Wideband Bandpass Filter at 0.5-2 GHz Band Using Multilayer Liquid Crystal Polymer Technology,” *IEEE Trans. Microw. Theory Tech.*, vol.60, no. 9, pp.2799-2807, Sept. 2012.

Chapter 7
Conclusions and Future Work

7.1. Conclusions

This thesis presented some recent developments on the design and fabrication of miniature bandpass filters for low frequency applications using multilayer LCP technology. These developments aimed to tackle two problems which had existed prior to the work in this thesis.

The first one has been related to fabrication of multilayer LCP devices. Prior to the work presented in Chapter 2, multilayer LCP filters in open literature only deploy two circuit layers and one ground. No via connections had been found to provide inter-connections between different circuit layers. Secondly, LCP filters had only been designed at frequencies above 3 GHz and there had been a need to explore the potential of LCP substrates for low frequency applications.

In total, 5 technical chapters, Chapter 2 to Chapter 6, have been included in this thesis to solve the above two problems. Since the fabrication of multilayer LCP devices has been continuously improved at different stages of the work carried out in this thesis, various fabrication techniques have been discussed in Chapter 2, 5 and 6, to address the first problem above. For the second problem, Chapter 2 and 3 are devoted to present novel ultra-wideband miniature filters operating at low frequencies, while Chapter 4 and 5 have discussed approaches for the design of bandpass filter with narrow/moderate bandwidths. Then Chapter 6 presented a packaged reconfigurable filter, which demonstrates another potential application of multilayer LCP technology. Fig. 7.1 illustrates the relations among these 5 chapters. The technical contributions from each chapter are summarised in the following paragraphs.

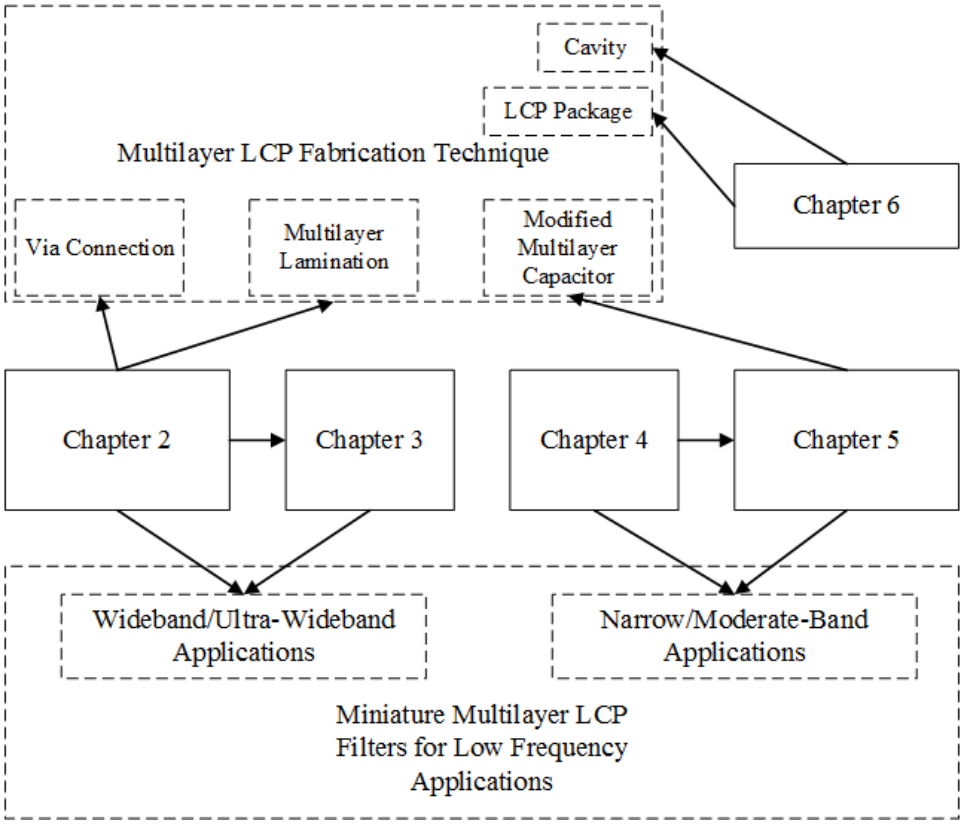

Fig. 7.1 Relations among the 5 technical chapters

In Chapter 2, two miniature ultra-wideband bandpass filters for the 0.5-2 GHz band were presented. Both filters were designed by cascading lumped-element highpass and lowpass filters. A value extraction process was introduced in this chapter to accurately control the capacitance/inductance of multilayer lumped-elements. This value extraction process significantly accelerates the design flow. Most importantly, in this chapter, 5 metal layers were used for the implementation of filters, which had not been done prior to this work. With such a 5-metal-layer structure, the sizes of these two filters are 80% smaller than previous work in open literature [7.1]. Reliable fabrication techniques for both lamination and via connection were also developed and the measured results of fabricated samples validate the fabrication techniques as well as the design approaches. This work simply shows that multilayer LCP filters can be much smaller than existing LCP filters in the open literature and for the first time as small as LTCC filters in terms of guided wavelength by using more layers in the design. The newly developed via fabrication techniques for LCP have shown that LCP designs with 5-metal-layers can be accurately fabricated, which will

ensure a promising future for the design and fabrication of multilayer LCP devices. Some of the work in this chapter leads to the publication of [7.2] and [7.3].

Chapter 3 continued the investigation of the design of ultra-wideband bandpass filters. Due to the collaboration with the Department of Microelectronics & Radio Engineering, Saint Petersburg ElectroTechnical University, the filter presented in this Chapter was designed for the 3.1-10.6 GHz UWB band. A novel and efficient circuit model was developed in this chapter. This model had fewer elements compared with conventional filter prototypes and leaded to a very compact and simple multilayer LCP implementation. Measured results showed very high yield of the fabrication of this filter. Thus the filter presented in this chapter can be regarded as a promising candidate for practical application. Although the mature LTCC technology can have similar yield, LTCC devices are usually not as low weight and the technology itself is not as low cost considering the fabrication facility needed for the lamination and co-firing (at 800 °C). Furthermore, compared with the work in [7.4], this design has similar performance, while the size is 30% smaller. This work was summarized and published in [7.5].

With the work in Chapter 2 and 3, two sets of design approaches have been developed for the design of miniature wideband multilayer LCP filters. The cascaded filter topology in Chapter 2 is very flexible and can be easily modified to meet other specifications, such as the number of poles and operating frequencies. The circuit model in Chapter 3 is more efficient and easier to implement. It will suit applications, where high yield is required.

Chapter 4 then starts the development of design methodologies for miniature bandpass filters with narrow/moderate bandwidths. Consisting of series LC resonators and capacitive inverters, a 4-pole direct-coupled bandpass filter is designed and shows a superior selectivity at the upper passband edge. To produce realizable element values, T to Π transformations were introduced to the design. Compared with conventional designs, this 4-pole filter has found to have a similar selectivity to a 5-pole Chebyshev design. In addition, due to the use of lumped-element and multilayer LCP fabrication, the second harmonic was pushed away from the passband. This gave the filter a spurious-free stopband with a bandwidth up to 9 times of the centre frequency. Furthermore, this design approach can be used for filters with any number of poles and the filter topology will always be symmetric unlike conventional Chebyshev filters, which have asymmetric topology when the number

of poles is odd. In short, this design approach is extremely useful for applications where the upper passband edge selectivity is critical. The wide stopband also reduces the cost of the whole system as a lowpass mask filter might not be needed. Some of the work in this chapter was published in [7.6].

With the capability of producing finite frequency transmission zeroes, the work in Chapter 5 can be regarded as a more advanced design approach for miniature bandpass filters with narrow/moderate bandwidths. By using a new type of matrix similarity transformation, a bridge was built between ideal frequency-independent inverters and practical frequency-dependent lumped element inverters. This eventually made it possible to design coupled-resonator filters with wideband response match with coupling matrix prototypes using frequency-dependent lumped element inverters. More importantly, theories presented in this chapter can be used to design filters with any order and transmission zeroes can be pre-defined at arbitrary locations. To minimise the fabrication tolerance, modified multilayer capacitors was also presented in this chapter. In general, the work in this chapter is a very important development for the theory of coupling matrix. It builds a bridge between ideal coupling matrix models and physical filter implementations. The multilayer lumped element LCP implementation presented in this chapter is also very special considering its circuit transformation process and can also be adopted by other technologies such as CMOS and LTCC. Some of the work in this chapter leaded to the publication [7.7].

As it can be seen here, Chapter 4 and 5 also provides two different solutions for the design of miniature bandpass filters with narrow/moderate bandwidths. The design approach in Chapter 4 is simple and straight forward, and is very suitable for applications where good selectivity and wide stopband is needed. If it is required to provide high attenuation at specific frequencies in the stopband, then the approach in Chapter 5 can be used to generate finite frequency transmission zeroes.

Chapter 6 presented a reconfigurable filter which was implemented as a multilayer LCP package. By using double pole double throw switches, non-dispersive stripline structures and periodic frequency responses from optimum stub filters, this reconfigurable filter was of low insertion loss and easy to design. In addition, cavity structures were fabricated on LCP, which completes the development of fabrication techniques for multilayer LCP devices. This shows that various multilayer structures which exists on LTCC can now be

implemented on LCP as well and it demonstrates the potential of LCP as the next generation multilayer solution for low cost and compact microwave devices. The work in this chapter was published in [7.8].

Table 7.1 lists the sizes and design specifications of some of the miniature filters presented in this thesis.

Design		Size ($\lambda_g \times \lambda_g \times \lambda_g$)	Passband FBW	Stopband FBW	Other Properties
Chapter 2	Fig. 2.15	0.058 × 0.026 × 0.004 5 Metal Layers	120%	360%	Cascaded Design and Flexible Approach
	Fig. 2.19(a)	0.065 × 0.026 × 0.004 5 Metal Layers	120%	400%	
Chapter 3	Fig. 3.4(a)	0.2 × 0.2 × 0.014 3 Metal Layers	110%	>200%	Efficient Circuit Model, Easy Implementation, and High Yield
Chapter 4	Fig. 4.10(a)	0.074 × 0.018 × 0.0005 5 Metal Layers	20%	>1000%	Good Selectivity and Wide Stopband
Chapter 5	Fig.5.19	0.0294 × 0.0303 × 0.00052 4 Metal Layers	20%	>300%	Arbitrarily Defined Transmission Zeroes
	Fig. 5.26(a)	0.0282 × 0.0327 × 0.00052 4 Metal Layers	20%	>200%	

Table 7.1 Sizes and design specifications of some filters presented in this thesis.

In general, with the aim of investigate the design and fabrication techniques for multilayer microwave LCP filters, this thesis has shown that with newly developed fabrication techniques, multilayer LCP filters can be as compact as its competitor LTCC filters. Considering its low fabrication cost and low manufacture temperature, it is more compatible with existing low cost PCB technology than LTCC. This gives LCP a bright future in applications such as consumer communication systems, where cost is one of the key specifications. Furthermore, LCP has the advantage of low weight and has a certain degree of flexibility, which will attract applications such as satellite system, where weight and space is critical. The design approaches presented in this thesis also have many advantages over existing approaches. The design in Chapter 2 is very flexible while the one in Chapter 3 is highly efficient. Designs in Chapter 4 and 5 are very interesting developments of conventional coupled resonator filters and shows how ideal circuit models can be transformed to suit different design requirements.

7.2. Future Work

Based on the work presented in this thesis, some future work could be done.

- Most filters presented in this thesis use compact multilayer capacitors. However, due to the low relative dielectric constant of LCP, the capacitance density is still not high enough. To reduce the size of these capacitors, materials with high relative dielectric constant could be embedded into multilayer LCP devices to implement large capacitance. This might require some development of the fabrication technique for LCP at the same time.

- The filter in Chapter 3 is particularly interesting due to its capability of producing 4 reflection and 2 transmission zeroes with 9 components. However, it would be useful if a systematic approach could be developed to generate efficient circuit models with frequency response of higher order.

- Chapter 4 presented a filter with a superior stopband performance. To produce a more compact implement, the filter, which actually has a symmetric form, could be designed in a folded way. This would also make it easier to add cross couplings.

- The theory in Chapter 5 is extremely useful and differs from other approach by being able to generate a lumped-element model to match the response of a coupling matrix prototype in a relatively wide bandwidth. However, the filter examples only demonstrated this for a FBW of 20%. Thus future work could be done to investigate whether the theory could be applied to designs with FBW of 40% or even higher.

- The packaged reconfigurable filter in Chapter 6 has relatively large size in comparison with other filters presented in this thesis. To reduce the size, one feasible way would be introducing double-stripline structure into the design. This means that two stripline structures can be arranged in a vertical way to share one common ground. Then it would be able to design filters on top of each other with a ground in between for shielding purpose. This potentially could lead to 50% of size reduction in future.

References

[7.1] Z.-C. Hao and J.-S. Hong, "UWB Bandpass Filter Using Cascaded Miniature High-Pass and Low-Pass Filters With Multilayer Liquid Crystal Polymer Technology," *IEEE Trans. Microw. Theory Tech.*, vol. 58, no. 4, pp. 941-948, Apr. 2010.

[7.2] S. Qian, Z.-C. Hao, J.-S. Hong, J. P. Parry and D. P. Hand, "Design and Fabrication of a Miniature Highpass Filter Using Multilayer LCP Technology," *in Proc. 41th European Microw. Conf.*, Oct. 2011, pp. 187-190. Manchester, UK.

[7.3] S. Qian and J.-S. Hong, "Miniature Quasi-Lumped Element Wideband Bandpass Filter at 0.5-2 GHz Band Using Multilayer Liquid Crystal Polymer Technology," *IEEE Trans. Microw. Theory Tech.*, vol.60, no. 9, pp.2799-2807, Sept. 2012.

[7.4] Z.-C. Hao and J.-S. Hong, "Ultra-Wideband Bandpass Filter Using Multilayer Liquid-Crystal-Polymer Technology," *IEEE Trans. Microw. Theory Tech.*, vol. 56, no. 9, pp. 2095-2100, Sept. 2008.

[7.5] S. Qian, J.-S. Hong, A. Rusakov and I. B. Vendik, "A Novel Compact Ultra-Wideband Bandpass Filter," *in Proc. 43rd European Microw. Conf.*, Oct. 2013, pp. 896-899. Nuremberg, Germany.

[7.6] S. Qian and J.-S. Hong, "A compact multilayer liquid crystal polymer VHF bandpass filter," *in Proc. 43rd European Microw. Conf.*, Oct. 2013, pp. 1207-1210. Nuremberg, Germany.

[7.7] S. Qian, G. Brand, J.-S. Hong and P. Meyer, "The Design of Miniature Multilayer Bandpass Filters With Mixed Couplings," *IEEE Trans. Microw. Theory Tech.*, vol.61, no. 12, pp.4072-4078, Dec. 2013.

[7.8] S. Qian and J.-S. Hong, "Channel-reconfigurable filter with integrated switch in multilayer LCP package," *42nd European Microw. Conf.*, Oct. 2012, pp. 265-268. Amsterdam, Netherland.